


VNIVERSITAT  VALÈNCIA

Facultat de Física

Departament de Física de la Terra i

Termodinàmica



*A model to estimate daily albedo from
remote sensing data.*

*Accuracy assessment of MODIS MCD43
product*

**Tesi presentada per:
BELÉN FRANCH GRAS**

Portada: Imatge de fons corresponent al producte de reflectivitat superficial de MODIS CMG adquirit per Aqua (MYD09CMG) un dia d'Abril de 2005.

Contraportada: Delta del riu Lena a l'est de Sibèria. Imatge adquirida per Landsat 7 en juliol de l'any 2000 proporcionada per NASA en fals color.

José A. Sobrino Rodríguez, Catedràtic de Física de la Terra de la Universitat de València i director de la Unidad de Cambio Global,

CERTIFICA:

Que la present Memòria “**A model to estimate daily albedo from remote sensing data. Accuracy assessment of MODIS MCD43 product**”, ha estat realitzada baix la meua direcció al *Departament de Física de la Terra i Termodinàmica* de la Facultat de Física per **Belén Franch Gras**, i que constitueix la seua Tesi Doctoral per a optar al grau de Doctora en Física.

I per a que així conste, en compliment de la legislació vigent, signe aquest certificat en Burjassot, a 15 de Gener de 2013.

Fm.: J. A. Sobrino Rodríguez

AGRAÏMENTS

En aquestes línies vull expressar el meu agraïment a les persones i institucions que han contribuït a la realització d'aquest treball:

Al meu tutor i director de la Unitat de Canvi Global Dr. José Antonio Sobrino Rodríguez, per haver-me guiat i orientat des de els meus primers passos en Teledetecció. Gràcies per haver comptat amb mi per a formar part d'aquest grup.

A la Dra. Soledad Gandía, degana de la facultat de Física i anterior directora del *Departament de Física de la Terra i Termodinàmica* i al Dr. Jose Antonio Martinez Lozano, actual director del *Departament de Física de la Terra i Termodinàmica* per la seua amable acollida al departament.

Al Dr. Victor Reglero director del *Laboratori de Processat d'Imatges*, per el seu suport a la meua activitat investigadora, facilitant-me la utilització de les excel·lents instal·lacions del centre que dirigeix.

To Eric Vermote for welcoming me to his nice group and for teaching me most of the knowledge which has been indispensable to write this work. Thanks for giving me the opportunity of being a member of your group. To Emilie, Meredith, Martin, Andrea and Luiggi for your warmly welcome and for helping me while I was in the UMD.

Als meus companys de la Unitat de Canvi Global:

A Rosa per ser la meua companya de tobogan anímic que suposa escriure una tesi. No m'imagino com haguera sigut passar per aquesta època sense haver-ho compartit juntes. Espere que no perdes mai eixa alegria que saps transmetre a la gent del teu voltant. A Juan Carlos per prestar-me part del seu escàs temps per a resoldre'm dubtes. A Guillem per tots els consells que ens has donat al llarg dels anys. A Yves, per acceptar ser el president del tribunal i prestar la seua dedicació a corregir aquest treball. A Dražen, per mostrar-nos sempre la part positiva de la vida. Ànims en l'època que comences. A Cristian, membre honorífic del grup, per haver treballat conjuntament la part d'evapotranspiració que presente a la tesi i haver-se esforçat en acabar-ho a marxes forçades. A antics membres del grup com

Victoria, Mireia, Mariam i Ana perquè tots, d'alguna manera, han contribuït a aquest treball.

A la meua família pel seu suport incondicional que fins i tot ha travessat més d'una frontera. Gràcies per donar-me tant bons consells i ensenyar-me des de menuda a valorar els estudis. No se que faré sense vosaltres. Vos trobaré molt a faltar!

A Fernando per estar sempre al meu costat tant en els bons com en els mals moments (que no han sigut pocs). Gràcies per deixar-ho tot per a començar una nova vida junts tant lluny de la nostra terra. Gràcies per transmetre'm eixa fortalesa que tant admire de tu.

Als meus amics amb els que he compartit les hores de descans de la universitat.

La realització d'aquesta tesi ha sigut possible gràcies als següents projectes d'investigació:

“Metodologías avanzadas en observación de la Tierra: calibración de datos ópticos y extracción de la información, *EODIX*” (projecte AYA2008-0595-C04-01)

“Calibración de satélites de observación de la tierra en España, CEOS-Spain, (projecte AYA2011-29334-C02-01)

“*WATER and global Change (WATCH)*.” Unió Europea (projecte 036946)

“*Coordinated Asia-European long-term Observations system of Qinghai – Tibet. Plateau hydro-meteorological processes (CEOP-AEGIS)*.” Unió Europea (projecte FP7-ENV-2007-1 proposal No. 212921)

INDEX

INTRODUCCIÓ	1
INTRODUCTION	11
Chapter 1: Theoretical background	21
1.1. Radiation interaction with atmospheric components.....	21
1.1.1. Water vapor.....	23
1.1.2. Aerosols.....	24
1.2. Atmospheric correction.....	26
1.3. BRDF coupling correction.....	29
1.4. BRDF parametric models.....	32
1.5. BRDF inversion models.....	38
1.5.1. MODIS BRDF/Albedo product inversion.....	39
1.5.2. VJB method.....	40
1.6. Albedo estimation.....	42
Chapter 2: Methodology	45
2.1. Anisotropy influence study.....	45
2.2. Test of the MCD43 surface albedo estimation.....	47
2.3. Evaluation of BRDF inversion methods.....	49
2.3.1. 4parameter method.....	49
2.3.2. 5parameter Rsqr method.....	51
2.3.3. 5parameter Vsqr method.....	53
Chapter 3: Material	55
3.1. EODIX database.....	55
3.1.1. Study area and field campaign.....	55
3.1.2. In situ data.....	56

3.1.3. Airborne data.....	58
3.1.4. Satellite data.....	60
3.2. MODIS CMG database.....	61
Chapter 4: Results.....	67
4.1. Anisotropy influence study.....	67
4.2. Test of the MCD43 surface albedo estimation.....	83
4.2.1. Atmospheric correction.....	83
4.2.2. Airborne albedo estimation.....	85
4.2.3. Aggregation.....	87
4.3. Evaluation of BRDF inversion methods.....	89
Chapter 5: Application: Albedo accuracy impact on evapotranspiration precision.....	103
5.1. Introduction.....	104
5.2. Data acquisition.....	106
5.2.1. In situ data.....	106
5.2.2. Airborne data.....	107
5.3. Methods.....	108
5.3.1. Atmospheric correction.....	108
5.3.2. Albedo estimation.....	109
5.3.3. Land surface temperature and emissivity.....	109
5.3.4. Net radiation estimation.....	110
5.3.5. Daily evapotranspiration.....	110
5.4. Results.....	113
5.4.1. Albedo comparison.....	113
5.4.2. Net radiation.....	119

5.4.3. Ground heat flux.....	120
5.4.4. S-Sebi diagram and evaporative fraction (EF).....	122
5.4.5. H, LE and daily evapotranspiration.....	125
5.4.6. Comparison with in situ data.....	131
Chapter 6: Application: Albedo evolution and impact on land surface temperature.....	137
6.1. Methods.....	138
6.2. Results.....	139
6.2.1. Forest fires.....	141
6.2.2. Wind storms.....	144
6.2.3. Floods and land slides.....	146
6.2.4. Droughts.....	148
6.2.5. Decrease of albedo.....	149
CONCLUSIONS.....	151
REFERENCES.....	159

LIST OF FIGURES

Figura I.1. Comparació de la distribució de radiació en un bosc respecte a una pastura (Adaptada de Jackson et al. (2008)).

Figura I.2. Diagrama conceptual del impacte de l'augment d'albedo en la superfície. La línia de punts representa un feedback positiu i la línia de ratlles un feedback negatiu (Pitman, 2003)

Figure II.1. Comparison of the radiation distribution in a cropland or grassland (A) versus a forest (B) (Adapted from Jackson et al. (2008)).

Figure II.2. Conceptual diagram of the impact an increase in albedo has on the land surface and some elements of the boundary-layer climate. The dotted line represents a positive feedback and the dashed lines represent a negative feedback (Adapted from Pitman (2003)).

Figure 1.1. Influence of the atmospheric gasses on the radiation.

Figure 1.2. Scattering diagram of the radiation when it interacts with a particle in the particular cases of isotropic, and Mie scattering. The isotropic scattering is multiplied by 10. (Adapted from Slater, 1980)

Figure 1.3. Different contributions of the atmosphere and the surface to the top of the atmosphere signal

Figure 2.1. Description of the methodology used in this work.

Figure 3.1. In situ albedo measurements from a) a goniometer in a corn field, b) an albedometer located in a meteo station in a barley field and c) an albedometer located also in a meteo station but in a wheat field. D) AHS RGB image and position of the validation points (triangles)

Figure 3.2. AHS sensor. Scan-head and operator console and INTA C-212-200 EC-DUQ airplane.

Figure 3.3. Flight lines over the test area the 12th of June 2011.

Figure 3.4. Terra (left) and Aqua (right) platforms.

Figure 3.4. Study sites: a) KONZA EDC, b) Walker Branch, c) Howland and d) GSFC.

Figure 4.1. Plots of the V and R parameters in band 2 versus the NDVI classes considered in each area in order to apply the VJB methodology.

Figure 4.2. Temporal evolution of R and V in band 1 (a and b), band 2 (c and d) and band 4 (e and f) of MODIS.

Figure 4.3. Pixel-by-pixel comparison of BRDF corrected reflectance obtained from BRDF1 (first iteration, black) and from BRDF2 (second iteration, red) versus the lambertian reflectance for GSFC site in band 1 (a,b,c), band 2 (d,e,f) and band 4 (g,h,i).

Figure 4.4. Pixel-by-pixel comparison of BRDF corrected NDVI obtained from BRDF1 (first iteration, black) and from BRDF2 (second iteration, red) versus the lambertian NDVI for GSFC site.

Figure 4.5. Relative RMS between ρ_3 (considering it as the nearest to the true value) and (a) the top of atmosphere (TOA) reflectance, (b) ρ_1 and (c) ρ_2 versus the view zenith angle and for each zone.

Figure 4.6. Bias obtained considering the average of ρ_3 minus a) Top of Atmosphere reflectances, b) ρ_1 and c) ρ_2 versus the view zenith angle and for each zone.

Figure 4.7. White sky broad band albedo relative RMS (a) and bias (b) obtained comparing the albedo₂ to albedo₁ for each site

Figure 4.8. Airborne surface reflectance test over in situ measurements for each band.

Figure 4.9. Albedo test in the corn (circles), wheat (squares) and barley (triangles) fields.

Figure 4.10. Broadband blue sky albedo airborne image using a) the RTLSR model and b) the RTLSR-HS model

Figure 4.11. (a) Blue-sky broadband albedo airborne image from the RTLSR model. Squares: equivalence between MODIS pixels (b) and AHS area averaged (a).

Figure 4.12. MODIS and AHS albedo comparison of the nearest pixel to the corn (circles), wheat (squares) and barley (triangles) fields.

Figure 4.13. Temporal evolution of the broadband white sky albedo derived with the different methodologies at the Ispra site.

Figure 4.14. R and V parameters (band 2) versus the five NDVI classes of the Ispra pixel considered in the VJB method in the particular case of 2007.

Figure 4.15. Average year RMSE at the Ispra site between the proposed methods and the VJB method regarding the MCD43 product.

Figure 4.16. Percentage of the difference of the broadband white sky albedo of a Europe scene corresponding to the period from the 28th of July until the 13th of August of 2003 derived from a) the VJB method versus the MCD43 product and b) the method presented in this thesis versus the MCD43 product.

Figure 4.17. Broadband white sky albedo images of the Europe scene corresponding to the period from the 28th of July until the 13th of August of 2003 derived from the VJB, 4param, 5paramRsqr and 5param Vsqr methods versus the MCD43 product.

Figure 4.18. Percentage RMSE of a) the VJB method, b) the 4param method, c) the 5param Rsqr method and d) the 5param Vsqr method against the MCD43 product.

Figure 4.19. Histogram of Figure 4.18 images.

Figure 4.20. Land Cover Type Yearly Climate Modeling Grid (MCD12C1 MODIS product) and the classes considered in this study.

Figure 4.21. Average year RMSE for each class of the Europe scene between the proposed methods and the VJB method regarding the MCD43 product.

Figure 5.1. α_{REF} (left column) and α_{BRDF} (right column) along the main area during each flight overpass versus the view zenith angle.

Figure 5.2. α_{REF} (left) and α_{BRDF} (center) AHS images of the main area and α_{REF} vs. α_{BRDF} scatterplot (right) for 9:39 and 10:01 images.

Figure 5.3. Net radiation images ($\text{W}\cdot\text{m}^{-2}$) at 9:39 (-40° VZA) and at 10:01 (0° VZA) from α_{REF} (left) and from α_{BRDF} (right).

Figure 5.4. G using the albedo estimated from the reflectance (left) and the BRDF (right) 9:39 and 10:01 images (hot-spot (-40°) and Nadir VZA angles).

Figure 5.5. Albedo vs. Surface Temperature plots following the S-SEBI model for 9:39 and 10:01 UTC images. The linear fits indicate the upper and lower boundaries according to wet and dry surface assumptions respectively.

Figure 5.6. EF from α_{REF} (left) and from α_{BRDF} (right) at near to nadir VZA and VZA = -40°

Figure 5.7. H (W/m^2) from α_{REF} (left) and from α_{BRDF} (right) at near to nadir VZA and VZA = -40°

Figure 5.8. LE (W/m^2) from α_{REF} (left) and from α_{BRDF} (right) at near to nadir VZA and VZA = -40°

Figure 5.9. Daily ET (mm) images from α_{REF} (left) and α_{BRDF} (right) at Nadir (VZA= 0°) and VZA = -40° .

Figure 5.10. Wheat field surface broad band albedo, net radiation (W m^{-2}) and soil heat flux (W m^{-2}) time series comparison for each VZA differing between solar and orthogonal planes.

Figure 5.11. Barley field surface broad band albedo and net radiation (W m^{-2}) time series comparison for each VZA differing between solar and orthogonal planes.

Figure 5.12. Barley field sensible heat flux (W m^{-2}) and latent heat flux (W m^{-2}) time series comparison for each VZA differing between solar and orthogonal planes.

Figure 6.1. Slope in percentage of the albedo evolution from 2002 to 2011 over Europe and Northern Africa.

Figure 6.2. Albedo, LST and air temperature evolution in areas where forest fires caused a change in albedo.

Figure 6.3. Seasonal amplitude of the LST and the air temperature.

Figure 6.4. Albedo, LST and air temperature evolution in Bordeaux and south of Sweden.

Figure 6.5. Yearly average of LST and air temperature in Bordeaux and Sweden pixels.

Figure 6.6. Albedo, LST and air temperature evolution in the west of Germany and south of Poland.

Figure 6.7. Yearly average of LST and air temperature in west of Germany and south of Poland pixels.

Figure 6.8. Albedo, LST and air temperature evolution in Syria pixel.

Figure 6.9. Seasonal amplitude (left) and yearly average (right) of LST and air temperature in Syria pixel.

Figure 6.10. Albedo, LST and air temperature evolution in Portugal and Algeria pixels.

LIST OF TABLES

Table 1.1. Coefficients for the Black sky albedo and White sky albedo polynomials.

Table 3.1. Equivalence between AHS and MODIS bands.

Table 3.2. MODIS spectral bands.

Table 4.1. Relative RMS when estimating the surface reflectance from a Lambertian assumption versus considering BRDF₁ (ρ_2) or BRDF₂ (ρ_3).

Table 4.2. Relative RMS when estimating the NDVI from a Lambertian assumption versus considering BRDF₁ (NDVI₂) or BRDF₂ (NDVI₃).

Table 4.3. Relative RMS when estimating the white sky albedo from BRDF₂ (albedo₂) versus considering BRDF₁ (albedo₁).

Table 4.4. RMS and bias of the white sky broad band albedo when comparing albedo₁ to albedo₂

Table 4.5. Test of surface reflectance airborne images.

Table 4.6. Land cover classification types considered in this study.

Table 5.1. Data set used in this work retrieved during the EODIX field campaign

Table 5.2. Rni and Cdi values obtained from the meteorological station in the wheat field.

Table 5.3. Statistics for α_{BRDF} and α_{REF} for each AHS image.

Table 5.4. Statistics of Rn for each AHS image.

Table 5.5. Linear fit parameters of every LST-albedo diagram, mean and standard deviation.

Table 5.6. Statistics of H for each AHS image following VZA and overpass time.

Table 5.7. Statistics of LE for each AHS image following VZA and overpass time.

Table 5.8. Statistics of daily ET for each AHS image following VZA and overpass time.

Table 6.1. Estimation of surface emissivity.

Table 6.2. Slope in percentage of the LST and air temperature evolution from 2002 to 2011 in burnt areas pixels.

ACRONYMS

4parameter	proposed method that considers V and R lineality with the NDVI
5parameter Rsqr	proposed method that considers V lineality and R quadratic dependency with the NDVI
5parameter Vsqr	proposed method that considers V quadratic and R lineality dependency with the NDVI
6S	Second Simulation of a Satellite Signal in the Solar Spectrum
AERONET	Aerosol Robotic NETWORK
AHS	Airborne Hyperspectral Scanner
albedo₁	albedo derived from ρ_1
albedo₂	albedo derived from ρ_2
ASTER	Advanced Spaceborne Thermal Emission and Reflection Radiometer
BRDF	Bi-directional Reflectance Distribution Function
BRDF₁	BRDF derived from ρ_1
BRDF₂	BRDF derived from ρ_2
BSA	Black-sky albedo
CMG	Climate Modeling Grid
EF	Evaporative fraction
EODIX	Earth Observation: optical Data calibration and Information eXtraction
ET	Evapotranspiration
FOV	Field Of View
G	Ground heat flux
H	Sensible heat flux

LE	Latent heat flux
LST	Land Surface Temperature
MCD12C1	MODIS Land Cover Type Yearly product
MCD43	MODIS BRDF/albedo product
MOD04	MODIS aerosol product
MOD07	MODIS Atmospheric profiles product
MOD09	MODIS surface reflectance product
MODIS	MODerate resolution Imaging Spectroradiometer
NDVI	Normalized Difference Vegetation Index
NIR	Near InfraRed
R parameter	Roughness BRDF parameter (k_2/k_0)
RMS	Root Mean Square error
Rn	Net radiation
RTLRS	Ross Thick Li Sparse Reciprocal
RTLRS -HS	Ross Thick Li Sparse Reciprocal that includes the hot spot correction proposed by Maignan et al. (2004)
S-SEBI	Simplified Surface Energy Balance Index
TES	Temperature Emissivity Separation
TOA	Top Of Atmosphere
V parameter	Volume BRDF parameter (k_1/k_0)
VJB	Vetmote et al. (2009) method
VNIR	Visible and Near InfraRed
VZA	View Zenith Angle
WSA	White-sky albedo
α_{BRDF}	albedo derived from the BRDF integration

α_{REF}	albedo derived from the surface reflectance weighted average
ρ_1	surface reflectance derived from the Lambertian assumption
ρ_2	surface reflectance considering the BRDF coupling correction from BRDF ₁
ρ_3	surface reflectance considering the BRDF coupling correction from BRDF ₂

RESUM

L'albedo superficial és un paràmetre físic que afecta al clima de la Terra i, a més, suposa una de les majors incerteses radiatives en l'actual modelització climàtica. Aquest paràmetre és molt variable tant a nivell espacial com temporal (Wang and Davidson, 2007) degut als canvis en les propietats de les superfícies i als canvis en les condicions d'il·luminació. En conseqüència, es requereix una resolució temporal diària de l'albedo per a realitzar estudis climàtics. L'augment de la resolució espacial dels models climàtics fa necessari l'estudi de les seues característiques espacials a nivell global. La teledetecció proporciona l'única opció pràctica de proporcionar dades d'albedo a nivell global amb alta qualitat i alta resolució tant espacial com temporal. El sensor MODerate Resolution Imaging Spectroradiometer (MODIS) a bord dels satèl·lits Terra i Aqua presenta unes característiques adequades per a l'estimació d'aquest paràmetre. El producte oficial d'albedo (MCD43, Strahler et al., 1999) s'obté invertint el model de Bi-directional Reflectance Distribution Function (BRDF) a partir del producte oficial de reflectivitat superficial $M\{O,Y\}D09$ (Vermote and Vermeulen, 1999). Per a obtenir l'albedo es fan una sèrie d'assumpcions. En primer lloc, la reflectivitat superficial, la qual és la base per a obtenir l'albedo, s'estima considerant que la superfície es Lambertiana, es a dir, que reflexa la radiació per igual en totes les direccions. En canvi és ben sabut que les superfícies son anisòtropes, per tant, el primer objectiu de la tesi serà determinar com afecta l'assumpció Lambertiana en l'estimació de l'albedo. En segon lloc, el

model de BRDF que s'utilitza en la derivació de l'albedo no considera l'efecte *hot spot*, el qual consisteix en un màxim de reflectivitat quan l'angle d'observació i d'il·luminació coincideixen. Fent ús de la campanya de mesures EODIX en una àrea agrícola a Barrax (Albacete) en la que es realitzaren diversos vols amb sensors hiperespectrals, el següent objectiu de la tesi serà comparar amb dades in situ l'albedo estimat mitjançant el mateix model de BRDF que el producte oficial de MODIS amb el model que corregeix l'efecte *hot spot*. A més, avaluarem el producte d'albedo de MODIS amb imatges de satèl·lit amb l'albedo estimat pel sensor aerotransportat Airborne Hyperspectral Scanner (AHS) degradant-lo a la mateixa resolució espacial que MODIS. Finalment, buscant una millora de la resolució temporal de MODIS i basant-nos en la metodologia presentada per Vermote et al. (2009), la qual permet l'estimació de l'albedo de forma instantània, hem millorat aquest mètode fent-lo més robust. Per tant, l'últim objectiu serà comparar el producte oficial MODIS amb el mètode original de Vermote et al. (2009) i amb la millora proposada en aquesta tesi.

Per tal de dur a terme els objectius presentats, aquesta tesi es divideix en cinc capítols. A continuació resumim breument el contingut de cadascun d'ells.

CAPÍTOL 1

El primer capítol introdueix els fonaments físics en que ens basem per obtenir l'albedo a partir de dades mesurades mitjançant teledetecció.

Comença descrivint els components atmosfèrics que pertorben la senyal mesurada pels sensors en la regió espectral del visible i pròxim infraroig. A continuació, descrivim la correcció atmosfèrica de la senyal tant assumint que la superfície es Lambertiana com anisòtropa. S'inclou, també, un estudi bibliogràfic d'anteriors treballs que han abordat les implicacions de l'assumpció Lambertiana en la correcció atmosfèrica assenyalant la importància del nostre estudi en aquest marc.

El capítol continua desenvolupant els models paramètrics de BRDF que hem utilitzat en aquesta tesi, centrant l'atenció principalment en el model utilitzat en el producte MCD43 de MODIS resumint els principals resultats de l'avaluació d'aquest producte en anteriors publicacions.

Finalment, analitzem els diferents mètodes d'inversió de la BRDF remarcant principalment el mètode presentat per Vermote et al. (2009), al

que nomenem com mètode VJB, en el que ens basem per a desenvolupar un mètode millorat que proposem al Capítol 2. El mètode VJB assumeix que els paràmetres V i R que descriuen la BRDF son linealment proporcionals al Normalized Difference Vegetation Index (NDVI) al llarg d'un mateix any. Per a determinar el valor d'aquests paràmetres divideix un mateix any en cinc classes d'NDVI i per a cadascuna estima el valor de V i R . A continuació, ajusta linealment V i R en funció de l'NDVI de cada classe obtenint així una equació que es pot aplicar per a totes les imatges del mateix any considerat. En comparació amb el producte oficial MCD43 de MODIS en que la superfície s'assumeix estable durant un període de 16 dies (oferint imatges dels paràmetres de BRDF i d'albedo cada 8 dies) el mètode VJB permet una resolució temporal diària evitant, així l'assumpció d'estabilitat que pot donar uns resultats erronis en zones variables con és el cas de zones agrícoles.

CAPÍTOL 2

El segon capítol descriu la metodologia utilitzada per a complir els objectius d'aquest treball. El capítol es divideix en tres apartats. El primer apartat desenvolupa l'esquema que hem seguit per estudiar l'influència de l'assumpció Lambertiana en l'estimació de l'albedo superficial. El segon es centra en descriure els mètodes considerats en l'avaluació del producte MCD43 en el marc de treball de la campanya EODIX. Finalment, el tercer apartat descriu els mètodes d'inversió de la BRDF que hem desenvolupat a aquesta tesi. Aquests es basen en la mateixa assumpció que el mètode VJB de dependència de V i R amb l'NDVI. En canvi aquests mètodes presenten una millora respecte el mètode original que consisteix en evitar la classificació de la superfície al llarg d'un any en 5 classes d'NDVI invertint el model considerant totes les dades de l'any considerat. D'aquesta manera es aconsegueix un model més robust i suposa una reducció considerable del temps de processat. Per altra banda, es pretén millorar també l'assumpció original del mètode VJB de linealitat amb l'NDVI de V i R . Així, diferenciem tres mètodes proposats.

El model 4param que suposa la dependència lineal dels dos paràmetres amb l'NDVI de manera anàloga al VJB però seguint el mètode d'inversió proposat.

El model 5param Rsqr que suposa que V depèn linealment de l'NDVI en canvi R es pot descriure a partir d'una funció quadràtica respecte a l'NDVI.

El model 5param Vsqr que suposa que R depèn linealment de l'NDVI en canvi V es pot descriure a partir d'una funció quadràtica respecte a l'NDVI.

CAPÍTOL 3

El tercer capítol mostra les dades utilitzades en aquesta tesi doctoral tant a la campanya EODIX en que s'analitzen les dades adquirides mitjançant el sensor aerotransportat AHS i dades mesurades in situ, com les dades històriques adquirides pel sensor MODIS.

CAPITOL 4

El quart capítol presenta els resultats obtinguts. Aquest capítol, de forma anàloga al segon capítol, està dividit en tres apartats.

En primer lloc es mostren els resultats de l'estudi del impacte de l'assumpció Lambertiana en l'estimació de l'albedo. L'estudi es centra en quatre píxels localitzats al llarg d'Estats Units: KONZA EDC (39.10°N, 96.60°W) una regió de pastura on la principal cobertura es herba, Walker Branch (36.0°N, 84.30°W) un bosc de fulla perenne, Howland (45.20°N, 68.75°W) un bosc nòrdic i GSFC (39.00°N, 76.85°W) que consisteix en una mescla entre àrea amb vegetació i residencial. Els resultats sobre la reflectivitat superficial mostren que la regió espectral del visible (2-12%) és més sensible a l'anisotropia de la superfície que el pròxim infraroig (0.7-5%) presentant, a més, un major error la banda en el verd (3-12%) que en el roig (2-8%). En canvi els errors a penes afecten a l'estimació de l'NDVI amb errors menor a l'1%. Finalment, l'anàlisi sobre l'albedo superficial mostra errors menors a l'1% el que demostra que l'assumpció Lambertiana pot utilitzar-se en l'estimació d'aquest paràmetre.

En segon lloc s'analitzen els resultats de la campanya de mesures EODIX comparant els dos models de BRDF i s'avalua el producte oficial de MODIS amb dades in situ. En concret disposem de mesures in situ a un camp de blat, a un camp d'ordi i a un camp de dacsca. Comparant el mètode utilitzat per MODIS (RTLSR) i el proposat per Maignan et al. (2004) (RTLSR-HS) amb les dades in situ els dos proporcionen el mateix error igual a 0.018. En canvi, el mètode RTLSR subestima les mesures al camp d'ordi, qüestió que coincideix amb previs estudis on es senyala que aquest mètode presenta bons resultats al llarg de l'època de creixement dels cultius i subestima els altres períodes (Jin et al., 2003). La comparació amb les

dades de satèl·lit dona un error de 0.04 per als dos models. Aquest elevat error pot ser degut a treballar sobre una zona heterogènia on es molt difícil l'avaluació de qualsevol paràmetre. A més, la metodologia del producte MODIS es diferencia de la seguida a aquest treball en que considera un període de 16 dies en que la superfície es considera estable per a determinar la BRDF, el que pot suposar una font d'error en zones agrícoles on la vegetació pot canviar molt en poc de temps. Els resultats també mostren que tant el model RTLSR com el RTLSR-HS poden ser utilitzats indistintament fora de la zona del Hot Spot, on el segon presenta millors resultats.

Finalment, comparem diferents mètodes d'inversió de la BRDF. Els resultats mostren que tant el mètode VJB com els mètodes proposats proporcionen resultats equivalents al producte MCD43 de MODIS amb errors igual al 5.0% en el cas del mètode VJB i 6.1%, 5.1% i 5.3% per a 4param, 5param Rsqr i 5param Vsqr respectivament. Les majors incerteses es troben a les zones muntanyoses on la falta de dades al llarg de la major part de l'any suposa una gran dificultat per a estimar la BRDF no sols per als mètodes analitzats, sinó també per al MCD43 que utilitza un algorisme alternatiu en aquests píxels. Aquest estudi conclou que el tant mètode VJB com els mètodes proposats suposen una alternativa al producte oficial de BRDF i albedo de MODIS ja que milloren la resolució temporal d'aquests paràmetres amb uns mètodes simples. En aquesta tesi proposem el mètode 5param Rsqr com a millora del VJB ja que suposa un model més robust que evita la classificació en classes d'NDVI i, per tant, millora el seu temps d'execució.

CAPITOL 5

Molts estudis d'evapotranspiració utilitzen l'aproximació errònia de que l'albedo pot descriure's com la mitja ponderada de les diferents bandes de reflectivitat superficial (α_{REF}). En canvi, com hem vist al llarg d'aquesta tesi, l'albedo es calcula a partir de integració de la BRDF (α_{BRDF}). En aquest capítol presentem una aplicació que es basa en avaluar l'efecte que aquesta aproximació genera en la precisió de fluxos com son la radiació neta i l'evapotranspiració. Comparant α_{REF} i α_{BRDF} , el primer presenta una gran dependència angular mentre que α_{BRDF} reman estable al llarg de totes les observacions. La màxima diferència obtinguda correspon a la regió del Hot Spot on l'aproximació suposa un error de 0.11 (65%). En el cas de la radiació neta la diferència entre utilitzar α_{REF} i α_{BRDF} suposa errors de entre el 6 i el 17%. No s'observen grans diferències en el cas del flux de calor del sol i en la fracció evaporativa. En canvi, el calor sensible, el calor latent i

l'evapotranspiració diària suposa un error del 23-39%, 6-18% i 5-15% respectivament.

CAPITOL 6

El sisè capítol analitza una altra aplicació derivada de les dades temporals de MODIS CMG tractades i avaluades al capítol de resultats. En aquest cas ens centrem en estudiar l'evolució temporal de l'albedo al llarg de l'escena d'Europa considerada i veure la seua influència en la temperatura superficial i temperatura de l'aire. L'estudi es analitza per separat cadascun de les causes que originen un increment d'albedo en l'escena que inclou Europa i nord d'Àfrica entre 2002 i 2011. En primer lloc, els incendis forestals originats en diverses regions d'Espanya i Portugal implicaren un increment d'albedo de entre 0.02 i 0.05. Després d'aquests esdeveniments la temperatura superficial mostra un increment de les temperatures estacionals extremes proporcional a l'increment d'albedo. Aquest efecte dura entre tres i quatre anys, mentre la recuperació de l'albedo tarda més temps. La temperatura de l'aire a penes mostra variacions. La tempesta de vent ocasionada a Bordeus incrementà en 6K la temperatura superficial mitjana de l'any 2009 (quan va succeir) i 2K la temperatura de l'aire. En canvi, una altra tempesta de vent en Suècia així com les inundacions en l'oest d'Alemanya i al sud de Polònia i la sequera en Síria no mostren cap influència en les temperatures superficials i d'aire. Aquest estudi mostra, per tant que les zones ubicades al sud d'Europa mostren una major sensibilitat climàtica a l'increment d'albedo.

INTRODUCCIÓ

Els canvis de cobertura de la superfície induïts pels humans estan accelerant en el segle XXI a través d'impactes directes via reforestació, desforestació o intensificació de l'agricultura o d'impactes indirectes derivats de l'activitat humana. Aquests canvis estan afectant el clima a través de diferents mecanismes (Bounoua et al., 2002). En primer lloc, la combustió de carburant ha implicat l'augment de la concentració de gasos d'efecte hivernacle. En segon lloc, la modificació per part dels humans de la superfície ha ocasionat l'alliberament de carboni a causa de la desaparició y crema de vegetació així com l'absorció de carboni quan la vegetació creix o es plantada. En tercer lloc, la modificació antropogènica de la vegetació està afectant al clima a través de la mediació dels intercanvis d'energia, moment i aigua entre la biosfera i l'atmosfera.

INTRODUCCIÓ

L'impacte de la cobertura superficial en el clima pot ser dividit en dos grans categories: biogeoquímics i biogeofísics (Feddema et al., 2005). Els processos biogeoquímics afecten al clima alterant el ritme dels cicles biogeoquímics, canviant així la composició química de l'atmosfera. Els processos biogeofísics afecten directament als paràmetres físics que determinen l'absorció i disposició d'energia a nivell superficial. Dins d'aquesta categoria es troben les perturbacions radiatives degudes als canvis de cobertura superficial les quals son considerades com un dels mecanismes més influents en el canvi climàtic tant a escala global com regional (ex., Cess, 1978; Charney et al., 1977; Otterman, 1977). Les propietats reflectives de la superfície de la Terra alteren l'índex d'absorció de la radiació solar i, per tant, la disponibilitat d'energia en la superfície de la Terra. Petits canvis en l'albedo superficial (paràmetre que determina aquestes propietats reflectives i que descrivim en els següents paràgrafs) poden produir canvis en la temperatura global equivalents als atribuïbles a l'augment de gasos d'efecte hivernacle (Charlson et al., 2005). Per altra banda, la hidrologia superficial i les característiques de transpiració de la vegetació també es poden considerar dins la categoria de processos biogeofísics ja que afecten a com l'energia rebuda en la superfície es divideix en fluxos de calor latent i sensible. En el mateix cas es troba l'estructura de la vegetació ja que afecta a la rugositat de la superfície, alterant així al moment i el transport de calor.

La vegetació regula l'intercanvi d'energia entre la biosfera i l'atmosfera, determina els processos hídrics i, a través de la fotosíntesi, fixa el diòxid de carboni atmosfèric en la biomassa, per tant és una part fonamental dins de la biosfera. Les plantes contínuament ajusten la seua obertura estomàtica a les condicions atmosfèriques per tal de millorar l'absorció de carboni donada una determinada pèrdua d'aigua per evaporació (Cowan and Farquhar, 1977). Els canvis en la cobertura vegetal estan associats amb els canvis en la morfologia i fisiologia de les plantes, el que podria, en absència d'altres forces, alterar els fluxos superficials i consegüentment el clima, tant a escala regional com global.

INTRODUCCIÓ

Plantar boscos i evitar la desforestació pot ajudar a frenar l'augment de les concentracions de CO₂ i de les temperatures globals. Però, a més d'alterar el balanç de carboni i les emissions de gasos d'efecte hivernacle, els projectes forestals impliquen també un conjunt addicional de canvis biofísics (Jackson et al., 2008). Els boscos obscureixen la superfície en comparació a pastures, terres agrícoles o superfícies cobertes per neu com es pot observar a la Figura 1.1.

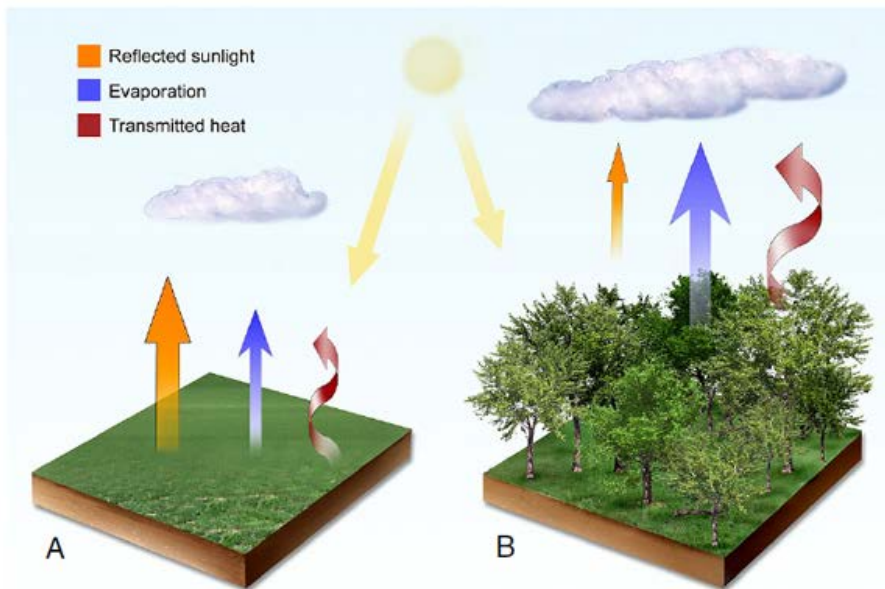


Figura 1.1. Comparació de la distribució de radiació en un bosc respecte a una pastura (Adaptada de Jackson et al. (2008)).

Aquest efecte implica una major absorció de la irradiància solar que pot calfar la superfície de forma regional. Altres canvis biofísics alteren la quantitat d'aigua que s'evapora de les plantes i de la superfície, la rugositat o la irregularitat de la vegetació, y la producció de núvols convectius i precipitacions. En general, tots aquests canvis poden afectar el clima tant a

INTRODUCCIÓ

nivell local com regional molt més que el segrest de carboni i, de vegades, de forma contradictòria.

La influència biofísica en la temperatura depèn d'on ocorren les activitats de segrest de carboni. En els tròpics, els boscos refreden regionalment al augmentar l'evapotranspiració de l'aigua des de la superfície a l'atmosfera. Aquest augment de vapor d'aigua pot ajudar a la formació de núvols que contribueixen addicionalment al refredament al reflectir la irradiància solar cap a l'espai. Feddema et al. (2005), Bonan (2008), i Pielke et al. (2002) trobaren que el canvi de cobertura en els boscos tropicals implica un increment de temperatura, ja que les pastures i els conreus tenen una menor transpiració i evaporació, el que resulta en la reducció del flux de calor latent i un augment de calor sensible en resposta al increment residual del balanç d'energia en la superfície.

Per altra part, els boscos boreals són un extrem diferent. Les taxes d'emmagatzematge de carboni són molt més lentes que en els tròpics a causa de les temperatures més fredes, menys llum solar i altres factors que limiten el creixement dels arbres. A més, les superfícies boreals estan cobertes de neu i gel durant llargs períodes de temps cada any. Per tant, el fet de modificar la neu per superfícies que absorbeixen més irradiància solar, com boscos d'avets o de pins, calfa l'àrea a escales espacials de centenars o inclús milers de kilòmetres. Com a resultat, plantar boscos en els països nòrdics pot ajudar a estabilitzar el CO₂ global però pot accelerar el calfament del clima a nivell regional, accelerant d'eixa manera la pèrdua de neu i cobertura de gel.

En canvi, les majors incerteses es troben en els boscos de latituds mitjanes (Field et al., 2007; Bala et al., 2007). Si be les seues taxes de segrest de carboni estan ben establertes, no es sap tant sobre cómo influeixen els canvis biofísics en el clima. Betts (2000) va simular els forçaments radiatius derivats de la modificació de la superfície al reforestar amb boscos en latituds mitjanes i zones boreals. Aquest estudi va concloure que el forçament positiu (augment de temperatura) induït per la disminució de la

INTRODUCCIÓ

reflexió de la superfície podria compensar el forçament negatiu esperat del segrest de carboni. Una sèrie d'estudis climàtics suggereixen que el fet de substituir els boscos per conreus o pastures refreden regionalment les temperatures en les latituds mitjanes (Bala et al., 2007; Diffenbaugh and Sloan, 2002; Oleson et al., 2004; Schaeffer et al., 2006). Així, Bounoua et al. (2002) van indicar que a les latituds mitjanes, on la modificació antropogènica del paisatge ha convertit grans extensions de boscos i pastures en terres de cultiu, l'augment de la reflexió de la superfície refreda la temperatura fins a 0.7°C a l'estiu i 1.1°C a l'hivern. En canvi, altres estudis mostren el contrari, que els boscos en latituds mitjanes refreden la temperatura en comparació amb pastures i conreus (De Fries et al., 2002; Jackson et al., 2005; Juang et al., 2007). En les zones més càlides dins d'aquesta regió, com el sud-est d'EEUU o nord d'Argentina, les temperatures superficials dels boscos son en general $1\text{-}5^{\circ}\text{C}$ més fredes que els cultius o les pastures més pròximes. Aquest refredament local es degut per una major evapotranspiració i un acoblament més eficient entre la superfície i l'atmosfera que s'atribueix a un augment de la rugositat. Paradoxalment, estos boscos també alliberen més calor a l'atmosfera perquè son més obscurs i absorbeixen més irradiància solar. La forma en que aquest calor es distribueix dins de l'atmosfera – tant en forma de temperatura d'aire com en forma de vapor d'aigua – no es comprèn bé. En algunes regions tropicals i de latituds mitjanes una quantitat addicional de vapor d'aigua pot formar núvols que contribueixen al refredament de la superfície i a l'augment de precipitacions en les zones pròximes. En altres regions on la disponibilitat de l'aigua es relativament escassa les plantacions de boscos poden calfar el clima regionalment a través de l'absorció de més radiació solar i l'augment substancial de l'evapotranspiració (Jackson et al., 2008). L'estudi, per tant, de la forma en que la superfície reflexa la irradiància solar que li arriba, així com la temperatura superficial de la mateixa, pot resultar de gran interès sobre tot en les latituds mitjanes.

L'albedo és la fracció de radiació solar que es reflectida per una superfície. En el sistema climàtic, l'albedo determina el balanç de radiació de la superfície i afecta a la temperatura de la superfície i a l'estructura de la

INTRODUCCIÓ

capa límit de l'atmosfera. En sistemes ecològics, l'albedo controla les condicions del microclima de les plantes i la seua absorció de radiació, el que afecta als processos físics, fisiològics i bioquímics com el balanç d'energia, l'evapotranspiració i la respiració. És ben sabut que la informació que proporciona l'albedo és important en la predicció de l'oratge, la projecció del clima i modelització de l'ecosistema (Wang and Davidson, 2007). Aquest paràmetre es considera també com un modulador important de les característiques climàtiques regionals com ara les sequeres naturals. Diversos estudis han demostrat que l'augment d'albedo de la superfície té un efecte negatiu en els fluxos d'humitat i les precipitacions, la desertificació i els resultats en general de les sequeres per una retroalimentació positiva entre la terra i l'atmosfera (Charney et al. 1977; Chervin, 1979; Sud and Fennessy, 1982; Sud and Molod, 1988; Xue and Shukla, 1993; Dirmeyer and Shukla, 1996; Knorr et al., 2001).

L'albedo és molt variable a nivell temporal (Wang and Davidson, 2007). Així, canvia naturalment amb l'angle solar d'il·luminació, a través de les estacions amb els canvis de vegetació i estocàsticament amb la pluja i la neu. També pot ser modificat directament, via l'activitat humana, o indirectament. La dinàmica de l'albedo està lligada a la dinàmica de l'ecosistema. Per tant, els impactes del canvi climàtic i la variació dels processos de l'ecosistema poden afectar a les característiques de l'albedo superficial. Ja que el sistema climàtic és molt sensible a l'albedo superficial, els ecosistemes poden retroalimentar significativament els escenaris del clima a través de canvis d'albedo. Així, des del punt de vista radiatiu, la desforestació canvia la radiació d'ona curta absorbida a nivell de superfície degut a l'increment de l'albedo superficial, mentre que els major impactes del calfament per efecte hivernacle són els canvis en la radiació d'ona llarga de l'atmosfera tant en direcció de la superfície com cap a l'espai (Zhang et al., 2001). A més, la desforestació altera la partició radiativa entre el calor latent i el calor sensible i, per tant, afecta a les propietats de la humitat i la temperatura del sol. L'eliminació de vegetació i l'exposició de sol nu disminueix l'emmagatzematge i la capacitat de l'aigua en la superfície, incrementant l'escorrentia i l'albedo (Charney, 1975; Mintz, 1984;

INTRODUCCIÓ

Cunnington and Rowntree, 1986). El descens de la humitat disponible per la superfície implica un descens del flux de calor latent que implica un augment de temperatura.

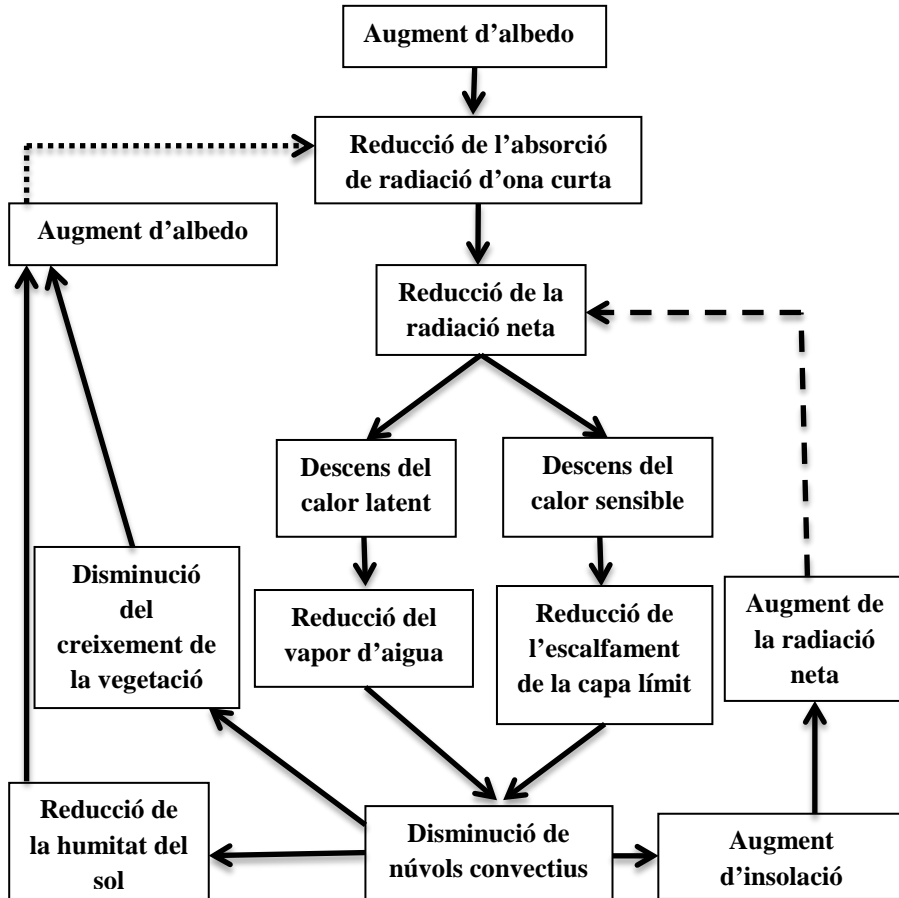


Figura I.2. Diagrama conceptual del impacte de l'augment d'albedo en la superfície. La línia de punts representa un feedback positiu i la línia de ratlles un feedback negatiu (Pitman, 2003)

INTRODUCCIÓ

Per altra part, l'augment d'albedo produeix una pèrdua de radiació neta. En els càlculs de models climàtics, aquest últim efecte sembla ser dominant en regions àrides i semi-àrides i l'efecte de dèficit de radiació origina una subsidència (moviment de l'aire en direcció descendent) a llarga escala. En aquest escenari d'aire descendent, la formació de núvols i precipitació seria molt difícil i l'aridesa tendria a augmentar. La reducció de núvols, en gran part a causa de la deforestació, no només debilita l'augment de l'albedo superficial al permetre que arribe més radiació solar a la superfície durant el dia, sinó que també modifica la radiació d'ona llarga entre la superfície i l'atmosfera permetent que més radiació d'ona llarga es perdi per la superfície calenta. Al mateix temps, la reducció del flux de calor latent pot compensar la pèrdua de radiació d'ona llarga per la reducció de la cobertura de núvols contribuint a mantindre l'increment de temperatura. Existeixen complexos processos de retroalimentació mitjançant els canvis en núvols i precipitació respecte a la pertorbació inicial de l'albedo (Figura 1.2).

Per tal de poder estudiar la variació de l'albedo no sols necessitem una adequada resolució temporal sinó que també la millor precisió possible, els quals són els principals objectius d'aquesta tesi. El sensor MODerate Resolution Imaging Spectroradiometer (MODIS) a bord dels satèl·lits Terra i Aqua permet, gracies a les seues freqüències de pas i geometria d'adquisició, estimar l'albedo superficial. El producte oficial d'albedo (MCD43, Strahler et al., 1999) s'obté invertint el model de Bi-directional Reflectance Distribution Function (BRDF) a partir del producte oficial de reflectivitat superficial M{O,Y}D09 (Vermote and Vermeulen, 1999). Per a obtindre l'albedo es fan una sèrie d'assumpcions. En primer lloc, la reflectivitat superficial, la qual és la base per a obtindre l'albedo, s'estima considerant que la superfície es Lambertiana, es a dir, que reflexa la radiació per igual en totes les direccions. En canvi és ben sabut que les superfícies són anisòtropes, per tant el **primer objectiu** de la tesi serà determinar com afecta l'assumpció Lambertiana en l'estimació de l'albedo. En segon lloc, el model de BRDF que s'utilitza en la derivació de l'albedo no considera l'efecte hot spot, el qual consisteix en un màxim de reflectivitat quan l'angle

INTRODUCCIÓ

d'observació i d'il·luminació coincideixen. Fent ús de la campanya de mesures Earth Observation: optical Data calibration and Information eXtraction (EODIX) en una àrea agrícola a Barrax (Albacete) en la que es realitzaren diversos vols amb sensors hiperespectrals, el **següent objectiu** de la tesi serà comparar amb dades in situ l'albedo estimat amb el mateix model de BRDF que el producte oficial de MODIS amb el model que corregeix l'efecte hot spot. A més, avaluarem el producte d'albedo de MODIS amb imatges de satèl·lit amb l'albedo estimat pel sensor aerotransportat degradant-lo a la mateixa resolució espacial que MODIS. Finalment, buscant una millora de la resolució temporal de MODIS i basant-nos en la metodologia presentada per Vermote et al. (2009), la qual permet l'estimació de l'albedo de forma instantània, havem millorat aquest mètode fent-lo més robust. Per tant, **l'últim objectiu** serà comparar el producte oficial MODIS amb el mètode original de Vermote et al. (2009) i amb la millora proposada en aquesta tesi.

Per tal de dur a terme els objectius presentats, aquesta tesi es divideix en cinc capítols:

El **primer capítol** presenta els fonaments físics en que ens basem per obtenir l'albedo a partir de dades mesurades mitjançant teledetecció. Començarem descrivint la correcció atmosfèrica de la senyal tant assumint que la superfície es Lambertiana com anisòtropa. A continuació, descriurem els models de BRDF paramètrics que hem utilitzat en el desenvolupament d'aquesta tesi. A més analitzarem els diferents mètodes d'inversió de la BRDF i finalitzarem detallant l'estimació de l'albedo.

El **segon capítol** descriu la metodologia utilitzada per acomplir els objectius nomenats. Aquest capítol el dividirem en tres apartats que es centraran en desenvolupar la metodologia seguida per tal d'acomplir cadascun dels objectius de la tesi per separat. Així mateix, descriurem els mètodes d'inversió de la BRDF que hem desenvolupat a aquesta tesi.

INTRODUCCIÓ

El **tercer capítol** mostra les dades utilitzades en aquesta tesi doctoral tant a la campanya EODIX en que s'analitzen les dades adquirides mitjançant el sensor aerotransportat AHS i dades mesurades in situ, com les dades històriques adquirides pel sensor MODIS.

El **quart capítol** presenta els resultats obtinguts. Aquest capítol, de forma anàloga al segon capítol, està dividit en tres apartats. En primer lloc es mostren els resultats de l'estudi del impacte de l'assumpció Lambertiana en l'estimació de l'albedo. En segon lloc analitzarem els resultats de la campanya de mesures EODIX comparant els dos models de BRDF i avaluant el producte oficial de MODIS amb dades in situ. Finalment, comparem diferents mètodes d'inversió de la BRDF.

El **cinquè capítol** desenvolupa una aplicació dels resultats obtinguts a la campanya EODIX. Així utilitzem l'albedo a nivell aeri a aquesta campanya per a analitzar l'influència de la seua precisió en l'obtenció de l'evapotranspiració, paràmetre que descriurem àmpliament a aquest capítol.

El **sisè capítol** analitza una altra aplicació derivada de les dades temporals de MODIS CMG tractades i avaluades al capítol de resultats. En aquest cas ens centrem en estudiar l'evolució temporal de l'albedo al llarg de l'escena d'Europa considerada i veure la seua influència en la temperatura superficial i temperatura de l'aire.

Finalment, el **capítol Conclusions** resumeix els principals resultats obtinguts en aquesta tesi doctoral.

INTRODUCTION

Human-induced land cover change is likely to accelerate in the 21st century as direct impacts via reforestation, deforestation or agricultural intensification become supplemented by indirect effects of human activity. These changes are affecting climate through several mechanisms (Bounoua et al., 2002). First, the combustion of fossil fuel has resulted in the increase in the atmospheric concentrations of greenhouse gases. Second, human modifications of the land surface cause release of carbon to the atmosphere from the decay and burning of vegetation and uptake carbon when vegetation regrows or is planted. Third, anthropogenic modifications of the earth's vegetation modify climate through mediation of the exchanges of energy, momentum, and water between the biosphere and atmosphere.

Land-cover impacts on global climate can be divided into two major categories: biogeochemical and biogeophysical (Feddema et al., 2005).

INTRODUCTION

Biogeochemical processes affect climate by altering the rate of biogeochemical cycles, thereby changing the chemical composition of the atmosphere. Biogeophysical processes directly affect the physical parameters that determine the absorption and disposition of energy at Earth's surface. Inside this category, the radiative perturbations due to land-cover changes are considered among the strongest climate forcing mechanisms at global and regional scales (ex., Cess, 1978; Charney et al., 1977; Otterman, 1977). The reflective properties of Earth's surface, alters the absorption rate of solar radiation and hence energy availability at Earth's surface. Small changes in surface albedo, even below detection limits of existing satellite-derived products, can lead to global temperature changes equivalent to that attributable to the anthropogenic increase of any enhanced greenhouse gas (Charlson et al., 2005). Beside, surface hydrology and vegetation transpiration characteristics can also be considered inside the biogeophysical processes category since they affect how energy received by the surface is partitioned into latent and sensible heat fluxes. Additionally, vegetation structure affects surface roughness, thereby altering momentum and heat transport.

Vegetation regulates energy exchange between the land biosphere and the atmosphere, determines the hydrological processes and, through photosynthesis, fixes atmospheric carbon dioxide in the biomass. Therefore, vegetation is a fundamental part of the biosphere. Plants continuously adjust their stomatal aperture to atmospheric conditions in order to enhance carbon uptake for a given evaporative loss of water (Cowan and Farquhar, 1977). Changes in vegetative cover are associated with changes in plants' morphology and physiology, which could, in the absence of other forcings, alter the surface fluxes and consequently the climate both at regional and global scales.

Planting forests and avoiding deforestation can help to slow increases in CO₂ concentrations and global temperatures. However, in addition to altering the carbon balance and emissions of other greenhouse gases, forest projects come with an additional suite of biophysical changes (Jackson et al., 2008). They often darken the land surface compared to

INTRODUCTION

pastures, agricultural lands, and snow-covered surfaces (Figure 1.1). This effect leads to higher sunlight absorption that can warm the land regionally. Other biophysical changes alter the amount of water that evaporates from plants and soil, the roughness or unevenness of the vegetation canopy, and the production of convective clouds and rainfall. Overall, such biophysical changes can affect local to regional climate much more than the accompanying carbon sequestration does and sometimes in a conflicting way.

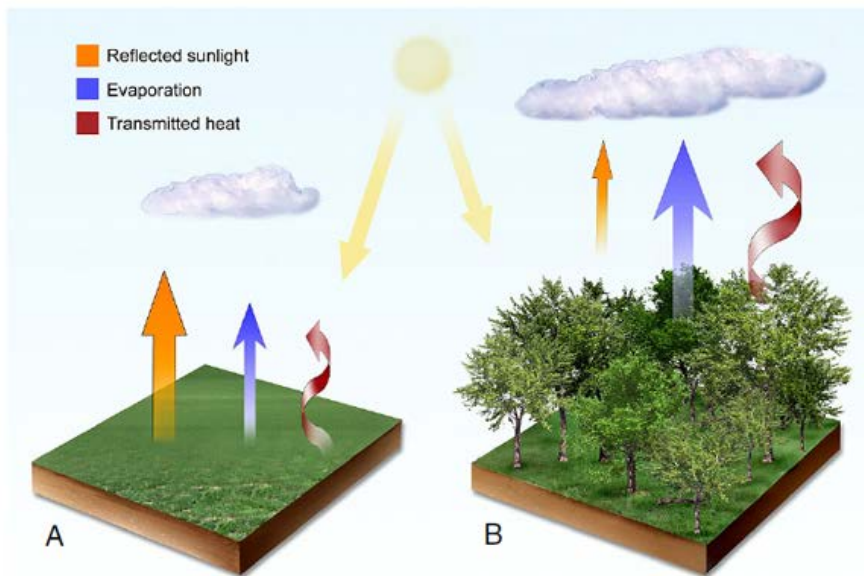


Figure II.1. Comparison of the radiation distribution in a cropland or grassland (A) versus a forest (B) (Adapted from Jackson et al. (2008)).

Biophysical influences on air temperature depend on where sequestration activities occur. In the tropics, forests cool regionally by increasing the evaporation of water from land to air. This added water vapor can help to form clouds that contribute to additional cooling by reflecting

INTRODUCTION

sunlight back to space. Feddema et al. (2005), Bonan (2008), and Pielke et al. (2002) found that in tropical forests land cover change results in warming, with the lower transpiration and canopy evaporation of grasslands and crops resulting in reduced latent heat flux and increased sensible heat flux in response to the increased residual surface energy budget.

Boreal forests provide a different extreme. Rates of carbon storage there are much slower than in the tropics because of colder temperatures, less sunlight, and other factors that limit tree growth. Boreal lands are also covered in snow and ice for extended periods each year. Replacing snow with a surface that absorbs more sunlight, such as an evergreen spruce or pine canopy, warms the area at spatial scales of hundreds or even thousands of kilometers. As a result, planting forests in northern countries will help to stabilize global atmospheric CO₂ but may accelerate climate warming regionally, further speeding the loss of snow and ice cover.

The greatest uncertainties lie in mid-latitude temperate forests (Bala et al., 2007; Field et al., 2007). While their rates of carbon sequestration are well established, much less is known about how accompanying biophysical changes influence climate. Betts (2000) simulated the radiative forcings associated with changes in surface albedo resulting from forestation in temperate and boreal forest areas. He found that the positive forcing induced by decreases in albedo could offset the negative forcing expected from carbon sequestration. A number of climate model studies suggest that replacing forests with agriculture or grasslands in temperate regions cools surface air temperatures (Bala et al., 2007; Diffenbaugh and Sloan, 2002; Oleson et al., 2004; Schaeffer et al., 2006). In this way, Bounoua et al. (2002) indicated that in temperate latitudes where anthropogenic modification of the landscape has converted large areas of forest and grassland to cropland, subsequent increases in albedo cool temperature by as much as 0.7 °C in summer and 1.1 °C in winter. Other studies show the opposite—that temperate forests cool the air compared with grasslands and croplands (De Fries et al., 2002; Jackson et al., 2005; Juang et al., 2007). In warm-temperate areas, such as the southeastern US or northern Argentina, surface temperatures of forests are often 1–5 °C cooler than adjacent

INTRODUCTION

grasslands or croplands. This local cooling is caused by more evapotranspiration and a more efficient coupling between the land and the atmosphere in forests attributable to increased roughness. Paradoxically, these forests also deliver more heat to the atmosphere because they are darker and absorb more sunlight. The fate of this added heat within the atmosphere (both in the form of air temperatures and water vapor) is poorly understood. In some temperate and tropical regions additional water vapor may form clouds that contribute to surface cooling and increased rainfall in nearby areas. In other regions where water availability is relatively scarce, such as the southwestern US, forest plantations may warm regional climate by absorbing more sunlight without substantially increasing evapotranspiration (Jackson et al., 2008). Therefore, the study of how the solar irradiance is reflected by the surface as well as its land surface temperature has a great interest in mid-latitudes.

Albedo is the fraction of incident solar radiation reflected by a surface. In the physical climate system, albedo determines the radiation balance of the surface and affects the surface temperature and boundary-layer structure of the atmosphere. In ecological systems, albedo controls the microclimate conditions of plant canopies and their radiation absorption, which, in turn, affects ecosystem physical, physiological, and biogeochemical processes such as energy balance, evapotranspiration, photosynthesis, and respiration. It has long been recognized that surface albedo information is important for weather forecasting, climate projection and ecosystem modeling (Wang and Davidson, 2007). This parameter was also found to be an important modulator for regional climate characteristics such as natural droughts. Several studies have shown that surface albedo has a negative effect on moisture flux convergences and rainfall, and desertification results generally in droughts by a positive feedback between land and atmosphere caused by high surface albedo (Charney et al. 1977; Chervin, 1979; Sud and Fennessy, 1982; Sud and Molod, 1988; Xue and Shukla, 1993; Dirmeyer and Shukla, 1996; Knorr et al., 2001).

INTRODUCTION

Land surface albedo is also highly variable temporally (Wang and Davidson, 2007). It changes naturally with solar insolation angle, seasonally with vegetation changes and stochastically with rain or snowfall. It can also be changed directly via human activity or indirectly. Surface albedo dynamics are closely related to ecosystem dynamics. Therefore, impacts of climate change and variations on ecosystem processes could possibly affect surface albedo characteristics. Since the physical climate system is very sensitive to surface albedo, ecosystems could significantly feedback to the projected climate scenarios through albedo changes. From the radiation point of view, deforestation causes change in absorbed shortwave radiation at the land-surface due to the imposed increase in surface albedo, while the major impacts of greenhouse warming are the changes of atmospheric longwave radiation both towards surface and out to space (Zhang et al., 2001). In addition, deforestation alters the surface radiative energy partition between H and λE and thus affects the surface moisture and thermal properties. Removal of vegetation and exposure of bare soil decreases soil water storage and capacity, increases runoff and the albedo (Charney, 1975; Mintz, 1984; Cunnington and Rowntree, 1986). Less moisture available at the surface means decreased latent heat flux leading to an increase in surface temperature. On the other hand, the increased albedo produces a net radiative loss. In climate model calculations, the latter effect appears to dominate in arid and semi-arid regions and the radiation deficit causes large scale subsidence. In this descending air, cloud and precipitation formation would be very difficult and aridity would tend to increase. Reduction of cloud cover, largely due to the effect of deforestation, not only weakens the effect of the increase in surface albedo by allowing more solar radiation to reach the land-surface during the day-time, but also modifies the longwave radiation between the land-surface and the atmosphere by allowing more outgoing longwave radiation to be lost by the warmed landsurface. At the same time, reduction of surface latent heat flux can offset the loss of outgoing longwave radiation by the reduction in cloud cover and makes a large contribution to maintaining the increased surface temperature. Complex feedbacks exist whereby changes in clouds or precipitation feedback to modify the initial perturbation to albedo (Figure 1.2).

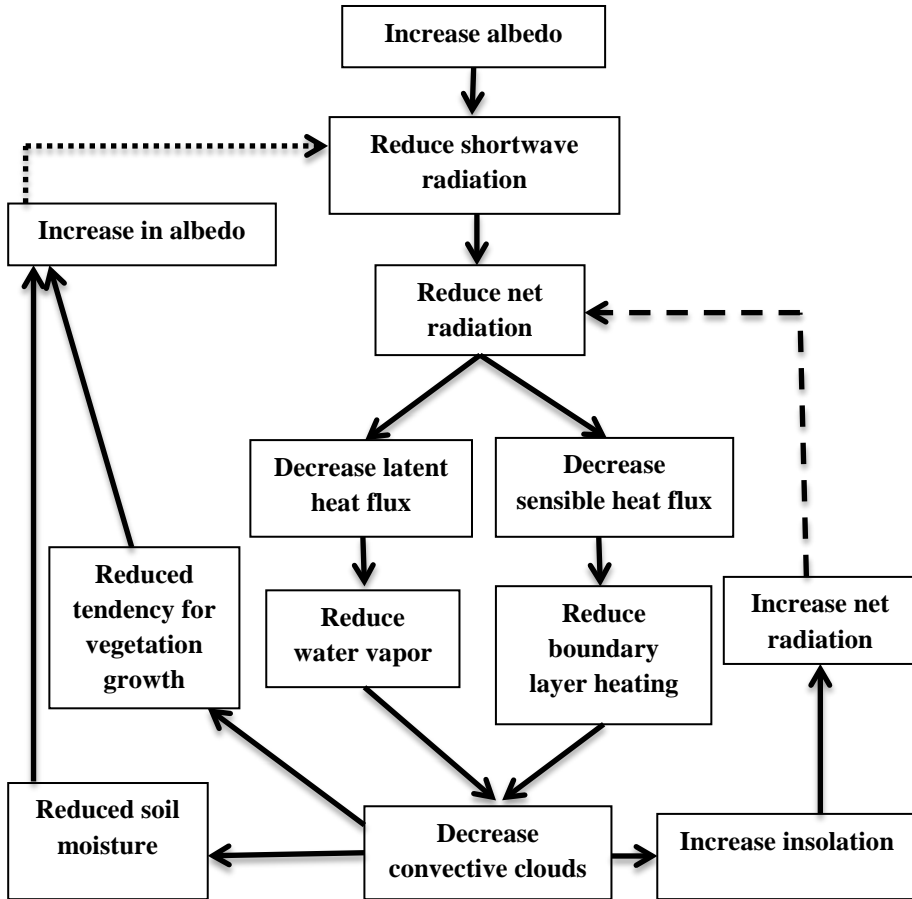


Figure II.2. Conceptual diagram of the impact an increase in albedo has on the land surface and some elements of the boundary-layer climate. The dotted line represents a positive feedback and the dashed lines represent a negative feedback (Adapted from Pitman (2003)).

In order to study the albedo evolution a good temporal resolution as well as the best accuracy is essential. Due to its acquisition geometry and frequency of satellite pass, the MODerate Resolution Imaging

INTRODUCTION

Spectroradiometer (MODIS) sensor onboard Terra and Aqua satellites allows the estimation of the surface albedo. The official albedo product (Strahler et al., 1999) is estimated through the Bi-directional Reflectance Distribution Function (BRDF) model inversion from surface reflectance images (Vermote and Vermeulen, 1999). In this way several assumptions are made in order to derive the surface albedo. First, the surface reflectance, which is the basis to obtain the albedo, is estimated considering that the surface is Lambertian, that is, it reflects radiance equally into all directions. However, it is well known that natural surfaces are anisotropic. Then, the first objective of the thesis will be the study of how the Lambertian assumption impacts on the albedo estimation. Secondly, the BRDF model considered in the albedo official product does not take into account the hot spot effect. This effect consists on a maximum of reflectance values when the view and illumination angles coincide. Taking advantage of the Earth Observation: optical Data calibration and Information eXtraction (EODIX) field campaign which was developed in an agricultural area in Barrax (Albacete) where several flights were achieved with airborne hyperspectral sensors, the next objective of this thesis is the comparison of in situ measurements with airborne albedo derived with the MODIS BRDF model and with the BRDF model that considers the Hot Spot effect correction. Additionally, we will evaluate the MODIS albedo product by comparing satellite albedo images to airborne albedo estimations. This study will be achieved through pixel aggregation in order to get to the same spatial resolution to the satellite images. Finally, looking for an improvement in the MODIS albedo temporal resolution and following Vermote et al. (2009) method which allows the instantaneous estimation of the albedo, we have improved this methodology presenting a more robust method. Therefore, the last objective of this thesis is the comparison of the MODIS official product with the results obtained with Vermote et al. (2009) method and with the improvement presented.

In order to achieve these objectives, the thesis is divided into five chapters:

INTRODUCTION

The **first chapter** presents the fundamental physics in which we base every study in order to obtain the albedo from remotely sensed data. We start describing the atmospheric correction of the signal assuming first the surface as Lambertian and next as anisotropic. Then, we describe the parametric BRDF models that we use in this thesis. Afterward, we analyze the different BRDF inversion methods. Finally, we show the equations used in the albedo estimation.

The **second chapter** describes the methodology followed to accomplish the objectives of this thesis. Therefore, this chapter is divided into three sections focusing on each one of the objectives presented above. Furthermore, we develop the proposed methods which we present in this thesis.

The **third chapter** on the one hand, describes the data that was acquired during the EODIX field campaign that consists on airborne images and in situ data and, on the other hand, details the historical MODIS CMG data used.

The **fourth chapter** presents the results obtained. This chapter, similarly to the second chapter, is divided into three sections. First, we show the results obtained in the study of the Lambertian assumption impact on the albedo estimation. Then, we analyze the results of the EODIX field campaign by comparing the two BRDF models and evaluating the MODIS official product with in situ data. Finally, we compare the BRDF inversion methods.

The **fifth chapter** develops an application from the EODIX field campaign results. Thus, we use the airborne albedo obtained in this campaign to analyze the influence of its accuracy on the evapotranspiration estimation, parameter that we describe in this chapter.

The **sixth chapter** analyzes other applications derived from MODIS CMG temporal data evaluated in the results chapter. In this case, we study

INTRODUCTION

the albedo temporal evolution over the European scene and we examine its influence on the land surface temperature and air temperature.

Finally, the **conclusions chapter** summarizes the main results obtained in this thesis.

CHAPTER 1

THEORETICAL BACKGROUND

This chapter provides a theoretical introduction to the concepts that will be needed in the following chapters starting from the atmospheric correction scheme, the BRDF estimation and finishing with the albedo derivation. Additionally, we will describe the state of the art of albedo monitoring from remotely sensed data.

1.1. RADIATION INTERACTION WITH ATMOSPHERIC COMPONENTS

When we use remote sensing data we must take into account the atmospheric perturbation since it is strong enough to modify the

CHAPTER 1

Theoretical Background

electromagnetic signal and, therefore, the information about the observed surface.

The electromagnetic radiation that passes through a material is attenuated by the absorption and scattering processes. In the particular case of the atmosphere, these processes are caused by its molecules and particles. The absorption is defined as the energetic transformation suffered by the radiation. As result there is a net alteration of the molecules' energetic levels, which is explained by the quantum theory. On the contrary, the scattering process determines the change of direction of part of the incident radiation. The classic electromagnetic theory explains this process that is spectrally continuous and does not lead to a net alteration of the energetic levels. Both processes lead to the extinction of radiation energy in the incident direction. Depending on the size of the molecules or particles that cause the scattering we can distinguish between two different scattering processes:

- *Rayleigh scattering* mainly consists of scattering from atmospheric gases. This occurs when the particles causing the scattering are smaller in size than the wavelengths of radiation in contact with them. This type of scattering is therefore wavelength dependent. As the wavelength decreases, the amount of scattering increases. Because of Rayleigh scattering, the sky appears blue. This is because blue light is scattered around four times as much as red light, and UV light is scattered about 16 times as much as red light.
- *Mie scattering* is caused by aerosols in the lower portion of the atmosphere. It occurs when the particles causing the scattering are larger than the wavelengths of radiation in contact with them. Mie scattering is responsible for the white appearance of the clouds.

In this thesis we focus on the solar spectrum region (400nm – 2500nm). In this spectral region the main atmospheric constituents responsible of the signal perturbation are the atmospheric gasses (such as the water vapor and ozone, Figure 1.1) and the aerosols.

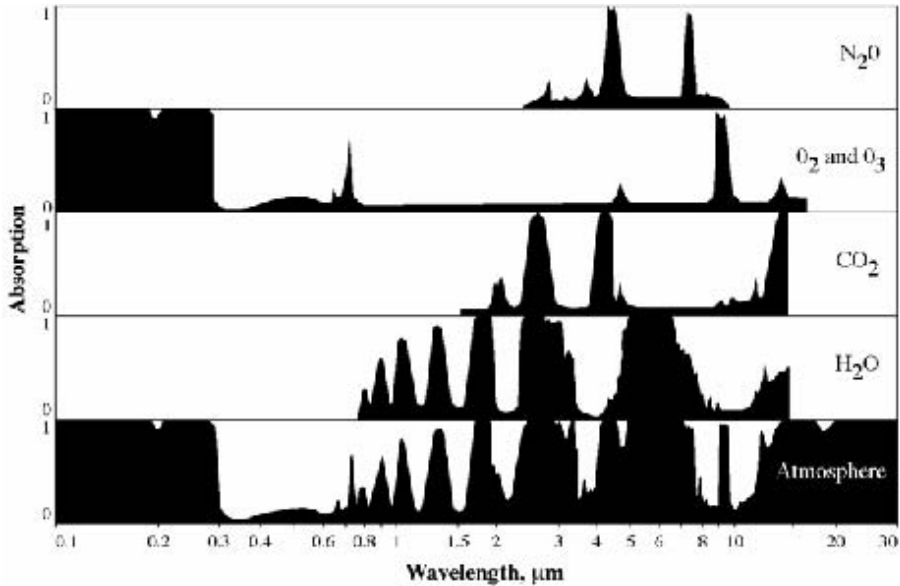


Figure 1.1. Influence of the atmospheric gasses on the radiation.

Regarding ozone, it presents a low temporal and spatial variability so a default value is usually considered. However, both aerosols and water vapor vary significantly at low temporal and spatial scales. Therefore, an accurate estimation of these atmospheric constituents is required. Next, we explain the main properties of the water vapor and aerosols.

1.1.1. Water vapor

The atmosphere contains variable amounts of water vapor resulting, mainly, from the evaporation of the seas and oceans. Most of it is located along the first five kilometers of air inside the troposphere. The water vapor content in a determined air volume varies with the temperature changes. The solar radiation interaction with water vapor molecules is controlled by the absorption mostly in the near infrared spectral region. The main absorption bands in this region are centered at 900, 940, 970, 1100, 1380 and 1870 nm. There are two other weaker absorption bands centered at 720 and 820 nm.

CHAPTER 1

Theoretical Background

The water vapor absorption bands in the visible spectral range are weaker therefore they can be ignored.

The water vapor can be monitored through in situ radiosondes which provide its vertical distribution along the atmospheric path. It can be also estimated from remote sensing techniques taking advantage of thermal bands which are more sensitive to its influence. As an example, the MODIS Atmospheric profiles product (MOD07, Seemann et al., 2006) provides daily atmospheric profiles at 5 km spatial resolution and at world-wide scale since year 2000. As far as we know, MOD07 is the existing atmospheric profiles product with the highest spatial resolution. Other sources of atmospheric profiles rely on the dataset provided by NCEP and the National Center of Atmospheric Research (NCAR) Reanalysis project (NCEP-1 here-in-after). NCEP-1 is a completely free available meteorological and climatological database often used for weather forecast and climate assessments. It covers a time period of about 60 years (from 1948 to nowadays), and it includes several meteorological variables at surface and 17 mandatory atmospheric levels, among others (Kistler et al., 2001).

1.1.2. Aerosols

An aerosol is a small, solid or liquid particle that is suspended in the air following its movement. Its characteristics depend on its origin; liquid particles are spherical while solid particles have different shapes and irregularities. Atmospheric aerosols can be originated naturally or anthropogenically. Some of these particles are emitted directly to the atmosphere (primary emissions) and others are emitted as gasses that form particles in the atmosphere when reacting (secondary emissions). Fundamentally, aerosols are concentrated in the lower layers of the atmosphere and their average life is of a few days. This is the reason for their high spatial and temporal variability. The chemistry composition of aerosols directly affects the way they interact with solar radiation. Figure 1.2 displays the scattering diagram of the radiation when it interacts with a particle. It shows that when the radiation incidences an aerosol, it is not scattered equally into every direction, but it is scattered preferably in the

radiation incidence direction so the radiation distribution pattern is highly asymmetric.

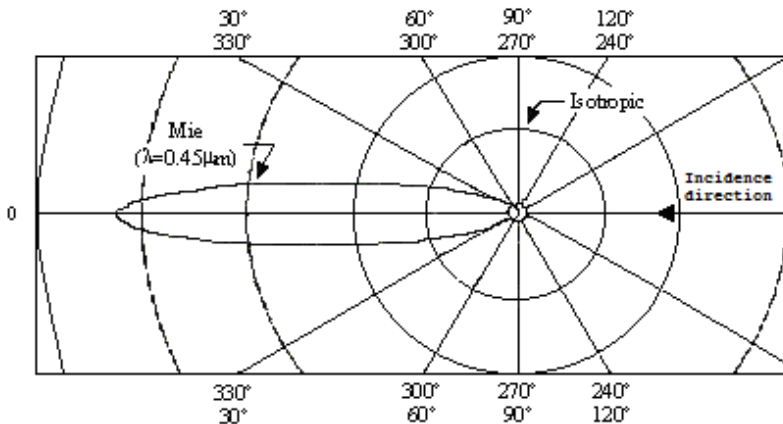


Figure 1.2. Scattering diagram of the radiation when it interacts with a particle in the particular cases of isotropic, and Mie scattering. The isotropic scattering is multiplied by 10. (Adapted from Slater, 1980)

The most used magnitudes to establish the amount of atmospheric aerosols are the Aerosol Optical Thickness (AOT) and the visibility. Aerosols can be measured in situ using sunphotometers. The Aerosol Robotic Network (AERONET, <http://croc.gsfc.nasa.gov/aeronet/index.html>) is an aerosol monitoring network from in situ measurements that serves as a database. The program provides a long-term, continuous and readily accessible public domain database of aerosol optical, microphysical and radiative properties for aerosol research and characterization, validation of satellite retrievals, and synergy with other databases. Additionally, aerosols can be estimated from remote sensing images. As an example, the MODIS aerosol product (MOD04) is actually composed of two entirely independent algorithms, one for deriving aerosols over land and the second for aerosols over ocean. Both algorithms were conceived and developed before the Terra launch and are described in depth in Kaufman et al. (1997) and Tanré et al. (1997). In addition, Levy et al. (2003) provide a more recent description of the over

CHAPTER 1

Theoretical Background

ocean retrieval algorithm. Both land and ocean aerosol algorithms rely on calibrated, geolocated reflectances provided by the MODIS Characterization Support Team (MCST), identified as products MOD02 and MOD03 for Terra MODIS products and MYD02 and MYD03 for the Aqua MODIS products.

1.2. ATMOSPHERIC CORRECTION

Atmospheric correction is the process by which the perturbation of remotely sensed signal due to atmospheric effects is removed. It is essential for the estimation of physical derived parameters or in order to analyze multitemporal data. Therefore, it is important to apply this process as accurately as possible. It is well known that the majority of land surfaces are anisotropic reflectors (Barnsley et al., 1997). This directional dependence of the land reflectance as a function of the sun–target–sensor geometry is described by the Bi-directional Reflectance Distribution Function (BRDF). However, atmospheric correction methods usually assume that the surface is uniform and Lambertian (Vermote and Kotchenova, 2008).

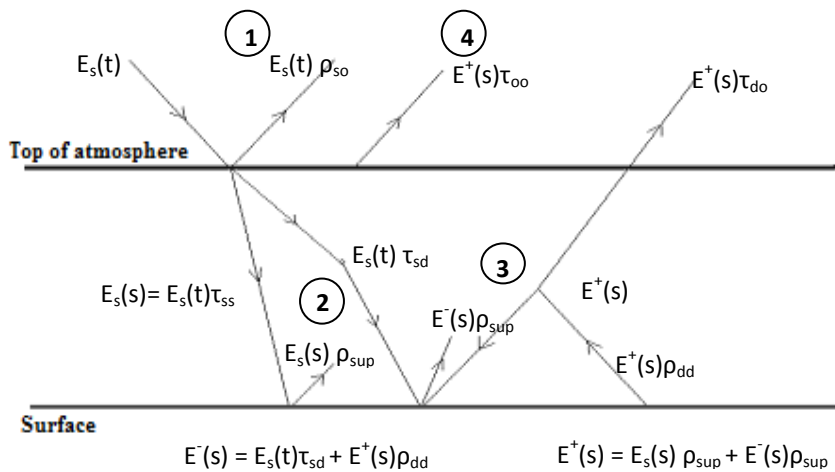


Figure 1.3. Different contributions of the atmosphere and the surface to the top of the atmosphere signal

Figure 1.3 shows the contributions to the top of the atmosphere signal in the visible and near infrared (VNIR) spectral range. Four terms are considered: (1) the photons reflected by the atmosphere before reaching the surface, (2) the photons transmitted directly to the target and directly reflected to the sensor, (3) the photons that are scattered by the atmosphere before reaching the target and directly reflected to the sensor and finally (4) the photons that have at least two interactions with the atmosphere and one with the target.

Taking these different contributions into account, if the surface is considered as uniform and Lambertian the radiative transfer equations for the atmosphere can be written as (Verhoef and Bach, 2003):

$$E_s(b) = \tau_{ss} E_s(t) \quad (1.1)$$

$$E^-(b) = \tau_{sd} E_s(t) + \rho_{dd} E^+(b) \quad (1.2)$$

$$E_o(t) = \rho_{so} E_s(t) + \tau_{do} E^+(b) + \tau_{oo} E_o(b) \quad (1.3)$$

$$E^+(b) = \rho_{surf} [E_s(b) + E^-(b)] \quad (1.4)$$

where (b) and (t) indicate the bottom and the top of the atmosphere irradiance € respectively. Eq. (1.1) describes the attenuation of direct sunlight by direct transmittance τ_{ss} through the whole atmospheric layer, Eq. (1.2) reflects the generation of diffuse downward flux (sky irradiance) by diffusely transmitted direct solar flux and upwelling diffuse flux from the surface that is reflected back by the atmosphere. Here, the term ρ_{dd} is the atmospheric spherical albedo. Eq. (1.3) describes how the top-of-atmosphere radiance is generated from atmospherically scattered direct sunlight via the term ρ_{so} (which can be considered a bi-directional reflectance of the atmospheric layer), diffuse upwelling flux that is scattered into the direction of view via the transmittance term τ_{do} , and directly transmitted radiance from the target via the direct transmittance τ_{oo} . Finally, Eq. (1.4) describes the reflection of radiance by a Lambertian surface.

Looking for the surface reflectance estimation, if it is considered a Lambertian surface so the approximation $E_o(b) = E^+(b)$ can be applied

CHAPTER 1

Theoretical Background

and using radiance units ($L_o(t) = E_o(t)/\pi$) the expression can be derived following

$$L_{sensor} = \left(\rho_{so} + \frac{(\tau_{ss} + \tau_{sd})\rho_{surf}\tau_{do}}{1 - \rho_{surf}\rho_{dd}} \right) \frac{E_s}{\pi} + \frac{(\tau_{ss} + \tau_{sd})}{1 - \rho_{surf}\rho_{dd}} \frac{E_s}{\pi} \rho_{surf}\tau_{oo} \quad (1.5)$$

where ρ_{so} is the bi-directional reflectance of the atmospheric layer, τ_{ss} is the downwelling direct transmittance, τ_{sd} is the diffuse transmittance in the solar direction, τ_{do} is the diffuse transmittance in the viewing direction, ρ_{dd} is the atmospheric spherical albedo, τ_{oo} is the upwelling direct transmittance and ρ_{surf} is the surface reflectance.

Using equation (1.5) but in reflectivity terms, ρ_{TOA} , and using the same notation as Vermote et al. (1997)

$$\rho_{sensor}(\mu_s, \mu_v, \phi) = \rho_0(\mu_s, \mu_v, \phi) + \frac{T(\mu_s)T(\mu_v)\rho_{surf}}{[1 - \rho_{surf}S]} \quad (1.6)$$

where $T(\mu_s) = \tau_{ss} + \tau_{sd}$ is the total transmittance from the top of the atmosphere to the ground along the path of the incoming solar beam, $T(\mu_v) = \tau_{oo} + \tau_{do}$ is the total transmittance from the ground to the top of the atmosphere in the view direction of the satellite, μ_s is the cosine of the solar zenith angle, μ_v is the cosine of the view angle, ϕ is the relative azimuth between the sun and the viewing directions, $\rho_0 = \rho_{so}$ and $S = \rho_{dd}$.

Finally, the surface reflectance is written in terms of atmospheric parameters and the image measured by the sensor (ρ_{sensor}):

$$\rho_{surf} = \frac{\rho_{sensor}(\mu_s, \mu_v, \phi) - \rho_o(\mu_s, \mu_v, \phi)}{T(\mu_s)T(\mu_v) + S(\rho_{sensor}(\mu_s, \mu_v, \phi) - \rho_o(\mu_s, \mu_v, \phi))} \quad (1.7)$$

1.3. BRDF COUPLING CORRECTION

If the surface is not Lambertian, the previous equation is inexact due to the coupling between the surface BRDF and the atmosphere BRDF (Lee and Kaufman, 1986) which equation (1.5) does not take into account. Therefore, in order to consider this effect and following Vermote et al. (1997) notation, the top of atmosphere reflectance is simulated as

$$\rho_{sensor}(\mu_s, \mu_v, \phi) = t_g(\mu_s, \mu_v) \left[\rho_o(\mu_s, \mu_v, \phi) + e^{-\tau_s} e^{-\tau_v} \rho_{surf}(\mu_s, \mu_v, \phi) + e^{-\tau_s} t_d(\mu_s) \bar{\rho} + e^{-\tau_v} t_d(\mu_v) \bar{\rho}' + t_d(\mu_s) t_d(\mu_v) \bar{\rho} + \frac{\left[e^{-\tau_s} + t_d(\mu_s) \right] \left[e^{-\tau_v} + t_d(\mu_v) \right] S(\bar{\rho})^2}{1 - S \bar{\rho}} \right] \quad (1.8)$$

where t_g is the transmittance due to gasses, $e^{-\tau/\mu_s}$ and $t_d(\mu_s)$ are the downward direct and diffuse transmittances of the atmosphere along the path of the incoming solar beam, $e^{-\tau/\mu_v}$ and $t_d(\mu_v)$ are the upward direct and diffuse transmittances of the atmosphere in the viewing direction, $\bar{\rho}$, $\bar{\rho}'$ and $\bar{\rho}$ are the surface hemispherical - directional, directional - hemispherical and hemispherical - hemispherical reflectances, respectively. These latter terms are also called coupling terms, as they are responsible for the coupling between atmospheric radiative transfer with the surface reflectance properties. They are written as

$$\bar{\rho} = \frac{\int_0^{2\pi} \int_0^1 \mu L_{R+A}^\downarrow(\tau_A, \tau_R, \mu_s, \mu_v, \phi') \rho_{surf}(\mu_s, \mu_v, \phi' - \phi) d\mu d\phi'}{\int_0^{2\pi} \int_0^1 \mu L_{R+A}^\downarrow(\tau_A, \tau_R, \mu_s, \mu_v, \phi') d\mu d\phi'} \quad (1.9)$$

$$\bar{\rho}'(\mu_s, \mu_v, \phi) = \bar{\rho}(\mu_v, \mu_s, \phi) \quad (1.10)$$

$$\bar{\rho} = \overline{\bar{\rho}'(\mu_s, \mu_v, \phi)} \quad (1.11)$$

CHAPTER 1

Theoretical Background

$$\frac{=}{\rho} \approx \frac{\int_0^1 \int_0^{2\pi} \int_0^1 \rho_{surf}(\mu, \mu', \phi) \mu \mu' d\mu' d\mu d\phi}{\int_0^1 \int_0^{2\pi} \int_0^1 \mu \mu' d\mu' d\mu d\phi} \quad (1.12)$$

where $L_{R+A}^\downarrow(\tau_A, \tau_R, \mu_s, \mu_v, \phi')$ is the downward diffuse irradiance with the Sun at μ_s and τ_R (resp. τ_A) are the Rayleigh (resp. aerosol) optical depth (Vermote et al., 1997). Equation (1.8) is not analytically invertible to retrieve the surface reflectance since ρ_{surf} is embedded in the integrals accounting for the coupling terms. However, this problem may be solved by an iterative process. This process consists of using a BRDF model to perform the integrals in the coupling terms. Once the coupling terms are known, a newer set of angular values is obtained. This is again used to update the coupling terms and the subsequent values. The procedure continues in this fashion until convergence in two consecutive iterations is found.

At this step we question the influence of considering the Lambertian assumption instead of considering the surface directional effects in the atmospheric correction scheme. Previous works, such as Lee and Kaufman (1986) studied the effects of the surface anisotropy on the derivation of surface reflectance, and on the vegetation index. Their results were based on three types of vegetation: savannah, pasture and coniferous forests from the Kriebel (1978) data set. They concluded that the Lambertian assumption can be used satisfactorily for a view zenith angle outside the backscattering region. Hu et al. (1999) analyzed also this issue but for MODIS simulated data. They considered four typical land cover types: a plowed field (barren), a field of hard wheat, a grass lawn and a hardwood forest. Their results showed errors of 3-7% in the red and 2-5% in the near-infrared spectral regions, with worst cases showing errors of up to 10-20%. They observed that the further away from isotropy the BRDF shape is, and the larger aerosol optical depth, the larger error becomes. Additionally, they obtained albedo errors between 1-2% in the red and near-infrared, with worst cases showing errors of up to 5%. These results were also validated by Lyapustin

(1999), who computed relative albedo errors between 1-2%, though in one case, it reached the 7%. All these works, though, used radiative transfer simulations over in situ measurements or simulated observation data, but none of them used remotely sensed data. However, Wang et al. (2010) worked with AERONET-based Surface Reflectance Validation Network (ASRVN) data, which is an automated data collection and processing system (Lyapustin et al., 2006; Wang et al., 2009) which receives 50×50 km² subsets of MODIS L1B data from MODIS adaptive processing system (MODAPS) and AERONET aerosol and water vapor information and performs atmospheric correction for about 100 AERONET sites based on accurate radiative transfer theory with complex quality control of the input data. They observed that uncompensated atmospheric scattering caused by the Lambertian model systematically biases the results underestimating the reflectance at high solar or view zenith angles and overestimating it at low zenith angles. Their results showed that the bias in the surface reflectance, in absolute magnitude, can be as high as 15% in the red band and 40% in the green band. These values, though, were higher than Hu et al. (1999) estimations. Regarding the albedo their average difference was about 0.008 in the green, 0.005 in the red and 0.004 in the near-infrared bands, concluding that the albedo product of MODIS presents a low but systematic negative bias due to the Lambertian assumption.

The first objective of this thesis is evaluating the influence of the Lambertian assumption when estimating both the surface reflectance and the surface albedo. Additionally, we will analyze the influence of the BRDF correction on the Normalized Difference Vegetation Index (NDVI; Tucker, 1979). If this index is not corrected atmospherically, its value will be degraded by reducing the contrast between the red and near infrared (NIR) reflected signals. The red signal normally increases as a result of scattered, upwelling path radiance contributions from the atmosphere, while the NIR signal tends to decrease as a result of atmospheric attenuation associated with scattering and water vapor absorption. The net result is a drop in the NDVI signal and an underestimation of the amount of vegetation at the surface (Huete et al., 1999). However, if the signal is corrected atmospherically with the Lambertian assumption, the degradation in the

CHAPTER 1

Theoretical Background

NDVI value will depend on how the surface anisotropy influences each spectral range.

This study was carried out using the radiative transfer code Second Simulation of a Satellite Signal in the Solar Spectrum (6S, Vermote et al., 2006). We focus our analysis on MODIS CMG Collection 6 data, which have improvements to the cloud mask and atmospheric profile algorithms regarding Collection 5 data. Therefore, although we also work with MODIS data, the database is not exactly the same as Wang et al. (2010) since they correct MODIS L1B data with their algorithm while we work directly with the MODIS official product. We will center the analysis on four different surfaces: a prairie region, a broadleaf forest, a boreal-northern hardwood transitional forest and a mixed pixel of vegetation and urban residential areas.

1.4. BRDF PARAMETRIC MODELS

The bidirectional reflectance distribution function (BRDF) describes the scattering of a parallel beam of incident light from one direction in the hemisphere into another direction in the hemisphere. The term BRDF was first used in the literature in the early 1960s (Nicodemus, 1965). The BRDF describes the intrinsic reflectance properties of a surface and thus facilitates the derivation of many other relevant quantities, e.g., conical and hemispherical quantities, by integration over corresponding finite solid angles. The BRDF can be expressed as

$$f_v(\theta_s, \phi_s; \theta_v, \phi_v) = \frac{dL_v(\theta_s, \phi_s; \theta_v, \phi_v)}{dE_s(\theta_s, \phi_s)} \quad (1.13)$$

where $\theta_s, \phi_s; \theta_v, \phi_v$ are the zenithal and azimuthal solar and view angles respectively; dE_s is the irradiance in the illumination direction ($dE_s(\theta_s, \phi_s) = \cos \theta_s \sin \theta_s L_s(\theta_s, \phi_s) d\theta_s d\phi_s$) and dL_v is the reflected radiance in the solid angle θ_v, ϕ_v (Nicodemus et al., 1977).

The BRDF quantifies the angular distribution of radiance reflected by an illuminated surface. A proper estimate of these functions is necessary for land surfaces studies (Maignan et al., 2004):

- to correct bidirectional effects in time series of vegetation indices and reflectances (Leroy and Roujean, 1994; Wu et al., 1995)
- to evaluate the coupling between surface reflectance and atmospheric scattering for proper atmospheric correction (Vermote et al., 1997) as we have seen in the previous section
- to classify land surface cover (Hyman and Barnsley, 1997; Zhang et al., 2002)
- to use the directional signature for the estimate of surface parameters such as leaf area index and other biophysical parameters (Knyazikhin et al., 1998; Bicheron and Leroy, 1999)
- to estimate the albedo from reflectance measurements (Wanner, 1997; Cabot and Dedieu, 1997) which is the main objective of this work.

Kernel-driven models for the BRDF of vegetated land surfaces attempt to describe the BRDF as a linear superposition of a set of kernels that describe basic BRDF shapes. Coefficients or weights are chosen to adapt the sum of the kernels to the given case (Wanner et al., 1995).

If the kernels are chosen to be a set of mathematical functions selected solely because their shape seems to be able to model BRDFs as they are actually observed, the model is purely empirical. There is no physical basis for such kernels beyond their description of BRDF-like shapes. One example for such a model is the modified Walthall model (Walthall et al., 1985; Nilson et al., 1989).

If the kernels chosen are derived from approximations of more-detailed physical models, where the approximations are made in order to deduce from the complex model a BRDF shape typical for that model, the model may be called semiempirical. Typically, semiempirical kernels are based either on one of several possible approximations to a radiative transfer scenario of light scattering in a horizontally homogeneous plant canopy or on one of several approximations feasible in a geometric-optical model of

CHAPTER 1

Theoretical Background

light scattering in forestlike canopies of distinct crown shapes. With a Lambertian term added, a kernel-driven semiempirical BRDF model thus consists typically of an isotropic term, a volume scattering term and a geometric scattering term (Roujean et al., 1992).

Among the BRDF models available, semiempirical models are regarded as some of the most versatile and the easiest to implement (Gao et al., 2001). They have the advantage of adjusting to many different kinds of land surface types and can be inverted analytically. These kinds of BRDF models have been widely used for data from the new generation remote sensors such as MODIS (Justice et al., 1998), Multiangle Imaging Spectroradiometer (MISR) (Diner et al., 1998) and Polarization and Directionality of the Earth's Radiation instrument (POLDER) (Leroy et al., 1997).

The kernel-driven models are three parameter semiempirical linear models. The theoretical basis of these models is that the land surface reflectance is modeled as a sum of three kernels representing basic scattering types: isotropic scattering, radiative transfer-type volumetric scattering as from horizontally homogeneous leaf canopies, and geometric-optical surface scattering as from scenes containing three-dimensional objects that cast shadows and are mutually obscured from view at off-nadir angles.

$$\rho(\theta_s, \theta_v, \phi) = k_0 + k_1 F_1(\theta_s, \theta_v, \phi) + k_2 F_2(\theta_s, \theta_v, \phi) \quad (1.14)$$

where θ_s is the sun zenith angle, θ_v is the view zenith angle, ϕ is the relative azimuth angle, $F_{1,2}$ are the kernels that represent the volume scattering and the geometric scattering respectively and $k_{0,1,2}$ are the model parameters associated to each kernel. F_1 models de medium as a collection of randomly located facets absorbing and scattering radiation. It represent leaves of canopies, characterized by a nonnegligible transmittance, but can also model behavior of dust, fine structures and porosity of bare soils. F_2 takes into account the geometrical structure of opaque reflectors and shadowing effects. It represents mainly irregularities and roughness of bare soil surfaces and structured features of low transmittance canopies. Each of the kernels describes different spatial scales of the vegetation cover: the geometric

kernel describes the landscape structure while the volume kernel represents the canopy structure. F_1 and F_2 are fixed functions of the observation geometry that have been derived from physical considerations of the radiative transfer at the surface, but k_0 , k_1 , and k_2 are free parameters. In the following, we will use V (for Volume) as k_1/k_0 and R (for Roughness) as k_2/k_0 .

The “Ross Thick Li Sparse reciprocal combination”, hereafter referred as the Ross-Li model, was selected for the processing of MODIS land surface measurements (Lucht et al., 2000). The volume scattering kernel (F_1), is based on the Rossthick function derived by Roujean et al. (1992) and is described by

$$F_1(\theta_i, \theta_v, \phi) = \frac{4}{3\pi} \frac{1}{\cos \theta_i + \cos \theta_v} \left[\left(\frac{\pi}{2} - \xi \right) \cos \xi + \sin \xi \right] - \frac{1}{3} \quad (1.15)$$

where

$$\cos \xi = \cos \theta_i \cos \theta_v + \sin \theta_i \sin \theta_v \cos \phi \quad (1.16)$$

The geometric kernel (F_2), is based on the LiSparse-Reciprocal model (Li and Strahler, 1992) but considering the reciprocal form given by Lucht (1998). It is given by the proportions of sunlit and shaded scene components in a scene consisting of randomly located spheroids of height-to-center-of-crown h and crown vertical to horizontal radius ratio b/r .

$$F_2(\theta_i, \theta_v, \phi) = O(\theta_i', \theta_v', \phi) - \sec \theta_i' - \sec \theta_v' + \frac{1}{2} (1 + \cos \xi') \sec \theta_i' \sec \theta_v' \quad (1.17)$$

where

$$\theta' = \arctg \left(\frac{b}{r} \operatorname{tg} \theta \right) \quad (1.18)$$

CHAPTER 1

Theoretical Background

$$O(\theta_i', \theta_v', \phi) = \frac{1}{\pi} (t - \sin t \cos t) (\sec \theta_i' + \sec \theta_v') \quad (1.19)$$

$$\cos \xi' = \cos \theta_i' \cos \theta_v' + \sin \theta_i' \sin \theta_v' \cos \phi \quad (1.20)$$

$$\cos t = \min \left(1, \frac{h \sqrt{D'^2 + (tg \theta_i' tg \theta_v' \sin \phi)^2}}{b \sec \theta_i' + \sec \theta_v'} \right) \quad (1.21)$$

$$D' = \sqrt{tg^2 \theta_i' + tg^2 \theta_v' - 2tg \theta_i' tg \theta_v' \cos \phi} \quad (1.22)$$

The dimensionless crown relative height and shape parameters h/b and b/r are within the kernel and should therefore be preselected. For MODIS processing, $h/b = 2$ and $b/r = 1$, i.e. the spherical crowns are separated from the ground by half their diameter. Generally, the shape of the crowns affects the BRDF more than their relative height.

Regarding the RossThick function (F_1), although this kernel aims at modeling the radiative transfer within the vegetation canopy, it does not account for the so-called hot spot or opposition effect, which occurs when viewing and illumination directions coincide (Breon et al., 2002). For viewing geometries close to backscattering, a strong reflectance peak is observed that is not accounted for in the linear model. Maignan et al. (2004) proposed a modification of the volumetric kernel in order to correct the hot spot effect. In this case, F_1 is written as

$$F_1^{HS}(\theta_i, \theta_v, \phi) = \frac{4}{3\pi} \frac{1}{\cos \theta_i + \cos \theta_v} \left[\left(\frac{\pi}{2} - \xi \right) \cos \xi + \sin \xi \right] \left[1 + \left(1 + \frac{\xi}{\xi_0} \right)^{-1} \right] - \frac{1}{3} \quad (1.23)$$

where ξ_0 is equal to 1.5° .

Maignan et al. (2004) showed that a slightly better fit to space borne measurements could be obtained through this correction for the Hot-Spot effect. Additionally, they also evaluated the importance of hot spot modeling

on the target albedo estimate. The hot spot generates a large reflectance increase, but limited to a small angular domain. Breon et al. (2002) predicted a negligible impact on the albedo. In fact, a model that does not account for the hot spot, fitted over well distributed measurements, tends to underestimate the BRDF close to backscattering and to overestimate it in other directions. This should lead to compensation of errors on the albedo estimate. However, when we work with remote sensing data we may do not dispose of well distributed measurements so this compensation may not occur. Therefore, the next objective of this thesis will be the analysis of the influence of considering this corrected kernel instead of the Ross thick function in the surface albedo estimation. This study will be developed taking advantage of the airborne images retrieved during the EODIX field campaign, which we will describe in the next chapter. In this framework, we will also evaluate the MODIS BRDF/albedo product using in situ albedo measurements in addition to airborne hyperspectral imagery.

The validation of the MODIS BRDF/albedo product has been studied in previous works. Jin et al. (2003) evaluated its accuracy by using only observations from the MODIS instrument aboard Terra platform and over homogeneous regions at local solar noon. They found that the MODIS albedo product met an absolute accuracy requirement of 0.02 in spring and summer, identifying them as the growing seasons. However, during the winter season they observed lower albedo estimations than the field values. Liang et al. (2002) validated the MODIS black-sky albedo product scaling up the ground measurements to MODIS resolution using high resolution Enhanced Thematic Mapper Plus (ETM+) imagery. In this work the authors considered that the surface is Lambertian, so the retrieved surface reflectance of different spectral bands are equivalent to surface spectral albedos. Despite this approach, the comparison showed a good agreement. Roesch et al. (2004) compared MODIS albedo at 0.05° with in situ measurements collected at Baseline Surface Radiation Network sites during snow-free periods. The results showed a good agreement, although MODIS generally underestimated the reflectivity. Coddington et al. (2008) compared the spectral surface albedo derived from the airborne Solar Spectral Flux Radiometer (SSFR) with the MODIS albedo product. They centred the analysis over two sites (an urban area and a ranch land whose primary

CHAPTER 1

Theoretical Background

vegetation cover was parched grass) where in situ albedo measurements were retrieved during the campaign. Their results showed a MODIS underestimation of 0.025-0.05 for the urban area and a MODIS overestimation of 0.02-0.05 for the rural area regarding the SSFR results. Liu et al. (2009) evaluated the ability of the MODIS albedo product to represent albedos at all diurnal solar zenith angles through a comparison with field measurements from the Surface Radiation Budget Network and the Atmospheric Radiation Measurement Southern Great Plains. They found a high correlation between in situ and satellite albedos for almost all cases. Additionally, they observed negative mean biases, which magnitude increased as the solar zenith angle increased, meaning that the MODIS algorithm underestimates albedo as compared with the ground measurements. Recently, Cescatti et al. (2012) compared MODIS albedo retrievals with surface measurements taken at 53 FLUXNET sites that met strict conditions of land cover homogeneity. They observed a good agreement for forest sites. On the contrary, in case of non-forest sites with larger albedo values (grasslands and croplands) MODIS generally underestimated in situ measurements across the seasonal cycle.

1.5. BRDF INVERSION MODELS

In the previous section we described some BRDF models. The next issue will be the derivation of the BRDF parameters from remotely sensed data. In this sense, we will dispose of surface reflectance images as well as their corresponding geometry images (solar zenith angles, view zenith angles and relative azimuth angles) which are the necessary inputs for the estimation of the kernel functions. Next, we describe two different inversion methods, first the inversion method used in the MODIS BRDF/albedo product (MCD43) and after that a method proposed by Vermote et al. (2009).

1.5.1. MODIS BRDF/Albedo product inversion

For view-illumination geometries typical of medium-resolution sensors such as Terra and Aqua MODIS, in order to obtain enough bidirectional observations to retrieve the BRDF free parameters, a period of sequential measurement is usually needed to accumulate sufficient observations. During this temporal window the model parameters are assumed to be constant. This method is currently used to derive the MCD43 product, which combines Terra and Aqua data to invert the BRDF model parameters over a composite period of 16 days, although it provides images every 8 days. Given reflectance observations ρ made at angles $(\theta_i, \theta_v, \phi)$, minimization $\partial e^2 / \partial f_k = 0$ of a least-squares error function

$$e^2 = \frac{1}{d} \sum_l \frac{(\rho(\theta_{i,l}, \theta_{v,l}, \phi_l) - R(\theta_{i,l}, \theta_{v,l}, \phi_l))^2}{\omega_l} \quad (1.24)$$

leads to analytical solutions for the model parameters k_k (Strahler et al., 1999)

$$k_k = \sum_i \left\{ \sum_j \frac{\rho(\theta_{i,j}, \theta_{v,j}, \phi_j) - F_i(\theta_{i,j}, \theta_{v,j}, \phi_j)}{\omega_j} \times \left(\sum_l \frac{F_i(\theta_{i,l}, \theta_{v,l}, \phi_l) - F_k(\theta_{i,l}, \theta_{v,l}, \phi_l)}{\omega_l} \right)^{-1} \right\} \quad (1.25)$$

where $R(\theta_i, \theta_v, \phi)$ is the reflectance derived from the BRDF model, ω_l is a weight given to each respective observation (e.g., $\omega_l=1$ or $\omega_l=\rho(\theta_i, \theta_v, \phi_l)$), and d are the degrees of freedom (number of observations minus number of parameters k_k).

The term in brackets that is to be inverted is the inversion matrix of the linear system which states the minimization problem.

One limitation of this method is the assumption of a stable target over the temporal compositing period. Another limitation is that it requires several cloud-free measurements of the target over the compositing period.

CHAPTER 1

Theoretical Background

In addition, the observation geometry of these measurements may not be suitable to properly constrain the BRDF model.

1.5.2. VJB method

Vermote et al. (2009) proposed a method for the inversion of the BRDF model with less constraint on the stability of the target. This method, hereafter referred to as VJB, accounts for the fact that the target reflectance changes during the year, but assumes that the BRDF shape variations are limited. Another way of presenting the hypothesis is that k_0 , k_1 and k_2 vary in time, but k_1 and k_2 stay proportional to k_0 . Additionally, the difference between the successive observations is mainly attributed to directional effects while the variation of $k_0(t)$ are supposed small. Therefore, V and R can be derived through the minimization of the day-to-day variations of $k_0(t)$.

$$\rho(t_i) [1 + VF_1^{i+1} + RF_2^{i+1}] \approx \rho(t_{i+1}) [1 + VF_1^i + RF_2^i] \quad (1.26)$$

This leads to a system of equations that can only be solved through iteration. The objective is to minimize the merit function:

$$M = \sum_{i=1}^{N-1} \frac{(\rho_{i+1} [1 + VF_1^i + RF_2^i]) - (\rho_i [1 + VF_1^{i+1} + RF_2^{i+1}])^2}{day^{i+1} - day^i + 1} \quad (1.27)$$

So R and V are solved by the classic derivation of the merit function that is

$$\frac{dM}{dV} = \frac{dM}{dR} = 0 \quad (1.28)$$

which leads to

$$\begin{pmatrix} \sum_{i=1}^{N-1} \Delta^i \rho F_1 \Delta^i \rho F_1 & \sum_{i=1}^{N-1} \Delta^i \rho F_1 \Delta^i \rho F_2 \\ \sum_{i=1}^{N-1} \Delta^i \rho F_2 \Delta^i \rho F_1 & \sum_{i=1}^{N-1} \Delta^i \rho F_2 \Delta^i \rho F_2 \end{pmatrix} \otimes \begin{pmatrix} V \\ R \end{pmatrix} = \begin{pmatrix} -\sum_{i=1}^{N-1} \Delta^i \rho \Delta^i \rho F_1 \\ -\sum_{i=1}^{N-1} \Delta^i \rho \Delta^i \rho F_2 \end{pmatrix} \quad (1.29)$$

where

$$\begin{aligned} \Delta^i d &= day_{i+1} - day_i + 1 \\ \Delta^i \rho &= (\rho_{i+1} - \rho_i) / \sqrt{\Delta^i d} \\ \Delta^i \rho F_1 &= (\rho_{i+1} F_1^i - \rho_i F_1^{i+1}) / \sqrt{\Delta^i d} \\ \Delta^i \rho F_2 &= (\rho_{i+1} F_2^i - \rho_i F_2^{i+1}) / \sqrt{\Delta^i d} \end{aligned} \quad (1.30)$$

In order to estimate V and R to apply equation (1.29) each year of the dataset considered is segmented into five different classes of NDVI with equal population. Then, R and V are inverted for each of these classes and band. After that, one can generate a linear function (two coefficients) that represents V and R as a function of the NDVI. However, this fitting must be weighted by each NDVI class error bar in order to minimize outlier influence. The error bars are estimated by running the inversion ten times, each time removing 10% of the data set at random. Finally, these functions can be applied to each NDVI image obtaining instantaneous BRDF parameters.

The reason of assuming a dependency of V and R with the NDVI over a year is that BRDF have been shown to be significantly different for bare soil and vegetated surfaces, because vegetated surfaces show higher anisotropy than bare soil (Bacour and Breon, 2005). Also, the NDVI is sensitive to the presence of vegetation, is easy to derive, and minimizes the directional effects (Franch et al., 2013).

This method, in contrast to the MODIS BRDF/albedo product inversion, can generate a product with the same frequency as the

CHAPTER 1

Theoretical Background

observations, which is particularly useful for monitoring rapid changes of vegetation cover, e.g., for agricultural areas.

Breon and Vermote (2012) compared this method with the MCD43 MODIS product for the correction of the surface reflectance time series. They worked with MODIS CMG data along 2003 analyzing a representative set of +100 targets selected on the basis of the location of AERONET sites. Their results showed that the performances of the two approaches are very similar, demonstrating that a simple four-parameter NDVI-scaled model performs as well as a more complex model with many more degrees of freedom.

The third objective of this thesis is to complete the Breon and Vermote (2012) study comparing the MCD43 product with the VJB method through the white sky albedo parameter. In this study we focus our analysis on MODIS CMG Collection 6 data from both Aqua and Terra satellites over a Europe scene from 2002 until 2011. Additionally, with the aim of improving the time processing of the VJB method and strengthen it in this thesis we present three different inversion methods based on the original algorithm that we also compare to the MCD43 product. We will develop these proposed methods in Chapter 2.

1.6. ALBEDO ESTIMATION

Albedo is defined as the ratio of the radiant flux reflected from a unit surface area into the whole hemisphere to the incident radiant flux or hemispherical angular extent (Schaepman-Strub et al., 2006). While reflectance is defined as this same fraction for a single incident angle, albedo is the directional integration of reflectance over all sun-view geometries (Pinty and Verstraete, 1992). Since the BRDF describes the directional dependence of the land reflectance as function of the sun-target-sensor geometry, the surface albedo is derived integrating the BRDF model over all view and illumination angles.

Downwelling flux may be written as the sum of a direct component and a diffuse component. Black-sky albedo or directional-hemispherical reflectance (DHR) is defined as albedo in the absence of a diffuse component and is a function of solar zenith angle. Whitesky albedo or bihemispherical reflectance (BHR) is defined as albedo in the absence of a direct component when the diffuse component is isotropic. It is a constant. Therefore, the albedo can be written by integrals of the BRDF model through the black-sky albedo (BSA) and the white-sky albedo (WSA).

$$\alpha_{bs}(\theta_i, \lambda) = \sum_k f_k(\lambda) h_k(\theta_i) \quad (1.31)$$

$$\alpha_{ws}(\lambda) = \sum_k f_k(\lambda) H_k \quad (1.32)$$

where

$$h_k(\theta_i) = \int_0^{2\pi} \int_0^{\pi/2} k_k(\theta_i, \theta_v, \phi) \sin \theta_v \cos \theta_v d\theta_v d\phi \quad (1.33)$$

$$H_k = 2 \int_0^{\pi/2} h_k(\theta_i) \sin \theta_i \cos \theta_i d\theta_i \quad (1.34)$$

where $k_k(\theta_i, \theta_v, \phi)$ are the BRDF model parameters.

Strahler et al. (1999) proposed analytical expressions for these integrals parameterizing them by polynomials of the solar zenith angle.

$$\alpha_{ws}(\lambda) = k_0(\lambda) H_{iso} + k_1(\lambda) H_{geo} + k_2(\lambda) H_{vol} \quad (1.35)$$

$$\begin{aligned} \alpha_{bs}(\theta, \Lambda) = & k_0(\Lambda) (g_{0iso} + g_{1iso} \theta^2 + g_{2iso} \theta^3) + \\ & + k_1(\Lambda) (g_{0geo} + g_{1geo} \theta^2 + g_{2geo} \theta^3) + k_2(\Lambda) (g_{0vol} + g_{1vol} \theta^2 + g_{2vol} \theta^3) \end{aligned} \quad (1.36)$$

Table 1.1 shows the value of the coefficients of (1.35) and (1.36) equations.

CHAPTER 1

Theoretical Background

Table 1.1. Coefficients for the Black sky albedo and White sky albedo polynomials.

	k= Isotropic	k= RossThick	k= LiSparse	k= RossThick Maignan
g_{0k} (term)	1.0	-0.007574	-1.284909	0.010939
g_{1k} (term)	0.0	-0.070987	-0.166314	-0.024966
g_{2k} (term)	0.0	0.307588	0.041840	0.132210
White-sky integral	1.0	0.189184	-1.377622	0.095307

The albedo, $\alpha(\theta, \lambda)$, under actual atmospheric conditions can also be modeled quite accurately as an interpolation between the black-sky (direct beam) albedo and white-sky (completely diffuse) albedo as a function of the fraction of diffuse skylight $S(\theta, \tau(\lambda))$, which, in turn, is a function of optical depth τ (Lewis and Barnsley, 1994; Lucht et al., 2000).

$$\alpha(\theta, \lambda) = [1 - S(\theta, \tau(\lambda))] \alpha_{bs}(\theta, \lambda) + S(\theta, \tau(\lambda)) \alpha_{ws}(\lambda) \quad (1.35)$$

Finally, the spectral to broadband conversion is achieved following Liang (2000) for the particular case of MODIS.

$$\begin{aligned} \alpha_{short} = & 0.160\alpha_1 + 0.291\alpha_2 + 0.243\alpha_3 + 0.116\alpha_4 + 0.112\alpha_5 \\ & + 0.081\alpha_7 - 0.0015 \end{aligned} \quad (1.36)$$

where α_i represents the albedo of MODIS band i .

CHAPTER 2

METHODOLOGY

This chapter is divided into three sections focusing on each one of the objectives of this thesis: analysis of the surface anisotropy influence in the atmospheric correction scheme, test of the MCD43 surface albedo estimation through two different BRDF models in the framework of the EODIX field campaign and the inter comparison of the MODIS albedo product with the VJB method and the proposed methods.

2.1. ANISOTROPY INFLUENCE STUDY

Figure 2.1 presents the methodology followed in the study of the surface anisotropy influence in the atmospheric correction scheme.

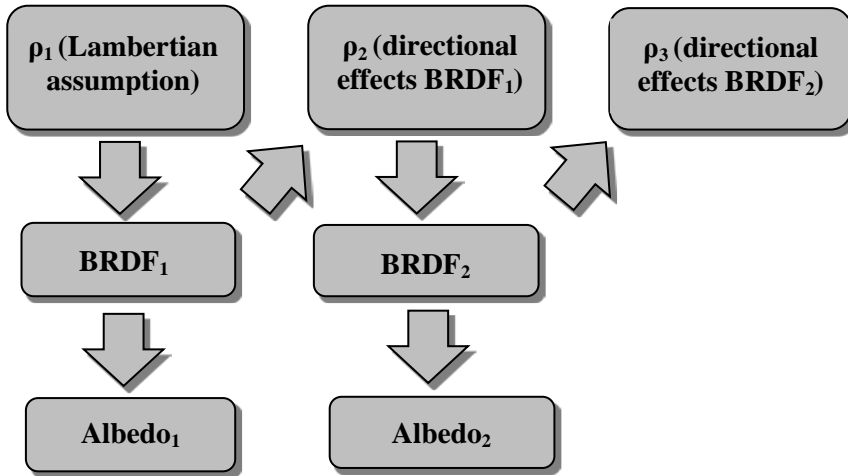


Figure 2.1. Description of the methodology used in this work.

Since CMG data provides surface reflectance estimations, first of all we inverted the atmospheric correction from these data in order to get to the LIB data. This process was carried out with the radiative transfer code 6S (Vermote et al., 2006) considering the surface as uniform and Lambertian. The necessary inputs in this process were the aerosol optical thickness at 550 nm, as well as the geometrical conditions of the pixel considered (day of the year, solar zenith angle, view zenith angle and relative azimuth angle). Additionally, we considered a continental aerosol model. Next, we estimated the surface reflectance (ρ_1) from raw data analogously as shown in the MODIS surface reflectance Algorithm Theoretical Background Document (ATDB, Vermote et al., 1999), and as shown in Chapter 1, considering the surface as uniform and Lambertian. In this step we obtained the equivalent to the MODIS surface reflectance product (MOD09) from which we start so the necessary inputs were the same as described in the inversion of the atmospheric correction. From this data we computed the BRDF model parameters ($BRDF_1$) and the albedo ($albedo_1$). Since these BRDF and albedo were derived from Lambertian data, we then used $BRDF_1$ in 6S in order to estimate the surface reflectance from raw data but considering the coupling between the BRDF and the downward radiance as shown in equation (1.7).

We considered this surface reflectance, ρ_2 , to retrieve a new BRDF ($BRDF_2$) and albedo ($albedo_2$). Finally, from $BRDF_2$ we estimated a final surface reflectance ρ_3 .

The BRDF was estimated using a kernel-based BRDF model based on the Ross-thick function derived by Roujean et al. (1992) but corrected for the Hot-Spot process proposed by Maignan et al. (2004) and on the Li-sparse model (Li and Strahler, 1986) but considering the reciprocal form given by Lucht (1998). In order to invert the BRDF parameters we followed the VJB method, which is briefly described in Chapter 1.

Finally, the albedo was derived by integrals of the BRDF model through a simple parametrization by polynomials of the solar zenith angle (Strahler et al., 1999). The conversion from spectral to broadband albedo was achieved using the equation proposed by Liang (2000).

In Chapter 4 we show the results obtained when comparing ρ_1 with ρ_2 and ρ_3 . With that aim we will estimate the Root Mean Square, RMS, relative error defined as:

$$RMS(\%) = \left[\frac{\sum_n \left(\frac{\rho_1 - \rho_{2,3}}{\rho_1} \right)^2}{n} \right]^{1/2} \quad (2.1)$$

2.2. TEST OF THE MCD43 SURFACE ALBEDO ESTIMATION

In order to test the MCD43 product, we first centered the attention on the airborne images. First of all they were corrected atmospherically with the radiative transfer code 6S (Vermote et al., 2006). The necessary inputs in this process were the aerosol optical thickness at 550 nm (which was retrieved continuously during the campaign with a CE318 sunphotometer),

CHAPTER 2

Methodology

the water vapor content (considered from a local radiosounding simultaneous to the airborne overpass), as well as the geometrical conditions of each pixel of each image (day of the year, solar zenith angle, view zenith angle and relative azimuth angle). Then, we tested the atmospheric correction comparing the results with in situ data acquired with spectral radiometers (that we describe in Chapter 3).

After that, we derived the airborne BRDF with the two different BRDF models: the RossThick-LiSparse-Reciprocal (RTLSR) model and the same model but corrected for the Hot-Spot process proposed by Maignan et al. (2004) (RTLSR-HS). First of all, we georeferenced every image and masked out the regions which did not correspond to the common area. Then, we inverted the models by using a least-squares method. Afterward, we estimated the white-sky albedo and black-sky albedo following equations (1.30) and (1.31). Since the black-sky albedo depends on the solar zenith angle, each airborne image had different black-sky albedo, but equal white sky albedo. Finally, with the fraction of diffuse skylight we derived the blue-sky albedo following equation (1.34) and estimated the broadband albedo following Liang (2000). We also estimated the broadband blue sky albedo, which was also evaluated with in situ measurements.

Beside, in order to compare the airborne images to the MCD43 product, since the MCD43A1 MODIS product consists on the BRDF parameters, we derived the blue sky broadband albedo following the same methodology as airborne data and considering the same angular conditions. Finally, we compared airborne to MODIS broadband blue sky albedo images.

2.3. EVALUATION OF BRDF INVERSION METHODS

In this study we will compare the MCD43 product with the results obtained from the VJB method and the results obtained with three methods proposed. Since the temporal resolution of the MODIS product is eight days

while the other methods provide daily albedo estimation, during the whole study we averaged each eight days a total of sixteen days in order to be sure we were comparing equivalent results.

2.3.1. 4parameter method

The 4parameter method consists of considering that R and V are represented by a linear function of the NDVI (that coincides with the assumption of the VJB method). That is:

$$V = V_0 + V_1 NDVI \quad (2.2)$$

$$R = R_0 + R_1 NDVI \quad (2.3)$$

However, compared to the VJB method we include this assumption into the merit function, which can be written as

$$M = \sum_{i=1}^{N-1} \frac{A_i^2}{\Delta^i d} \quad (2.4)$$

where

$$A_i = \rho_{i+1} \left[1 + (V_0 + V_1 NDVI_{av,i}) F_1^i + (R_0 + R_1 NDVI_{av,i}) F_2^i \right] - \rho_i \left[1 + (V_0 + V_1 NDVI_{av,i}) F_1^{i+1} + (R_0 + R_1 NDVI_{av,i}) F_2^{i+1} \right] \quad (2.5)$$

$$\Delta^i d = day_{i+1} - day_i + 1 \quad (2.6)$$

where $NDVI_{av,i}$ is the average of $NDVI_i$ and $NDVI_{i+1}$. A_i can also be written as

$$A_i = V_0 (\rho_{i+1} F_1^i - \rho_i F_1^{i+1}) + V_1 NDVI_{av,i} (\rho_{i+1} F_1^i - \rho_i F_1^{i+1}) + R_0 (\rho_{i+1} F_2^i - \rho_i F_2^{i+1}) + R_1 NDVI_{av,i} (\rho_{i+1} F_2^i - \rho_i F_2^{i+1}) + (\rho_{i+1} - \rho_i) \quad (2.7)$$

CHAPTER 2

Methodology

In this case there are four unknowns (V_0 , V_1 , R_0 and R_1) so the derivation of the merit function now is

$$\frac{dM}{dV_0} = \frac{dM}{dV_1} = \frac{dM}{dR_0} = \frac{dM}{dR_1} = 0 \quad (2.8)$$

Therefore

$$\frac{dM}{dV_0} = \sum_{i=1}^{N-1} \frac{(\rho_{i+1}F_1^i - \rho_i F_1^{i+1})}{\Delta^i d} 2A_i = \sum_{i=1}^{N-1} \frac{\Delta^i \rho F_1}{\sqrt{\Delta^i d}} 2A_i = 0 \quad (2.9)$$

$$\frac{dM}{dV_1} = \sum_{i=1}^{N-1} \frac{(\rho_{i+1}F_1^i - \rho_i F_1^{i+1})NDVI_{av,i}}{\Delta^i d} 2A_i = \sum_{i=1}^{N-1} \frac{\Delta^i \rho F_1 NDVI_{av,i}}{\sqrt{\Delta^i d}} 2A_i = 0 \quad (2.10)$$

$$\frac{dM}{dR_0} = \sum_{i=1}^{N-1} \frac{(\rho_{i+1}F_2^i - \rho_i F_2^{i+1})}{\Delta^i d} 2A_i = \sum_{i=1}^{N-1} \frac{\Delta^i \rho F_2}{\sqrt{\Delta^i d}} 2A_i = 0 \quad (2.11)$$

$$\frac{dM}{dR_1} = \sum_{i=1}^{N-1} \frac{(\rho_{i+1}F_2^i - \rho_i F_2^{i+1})NDVI_{av,i}}{\Delta^i d} 2A_i = \sum_{i=1}^{N-1} \frac{\Delta^i \rho F_2 NDVI_{av,i}}{\sqrt{\Delta^i d}} 2A_i = 0 \quad (2.12)$$

where

$$\begin{aligned} \Delta^i \rho &= (\rho_{i+1} - \rho_i) / \sqrt{\Delta^i d} \\ \Delta^i \rho F_1 &= (\rho_{i+1}F_1^i - \rho_i F_1^{i+1}) / \sqrt{\Delta^i d} \\ \Delta^i \rho F_2 &= (\rho_{i+1}F_2^i - \rho_i F_2^{i+1}) / \sqrt{\Delta^i d} \end{aligned} \quad (2.13)$$

Which leads to

$$A \otimes \begin{pmatrix} V_0 \\ V_1 \\ R_0 \\ R_1 \end{pmatrix} = \begin{pmatrix} -\sum_{i=1}^{N-1} \Delta^i \rho \Delta^i \rho F_1 \\ -\sum_{i=1}^{N-1} \Delta^i \rho \Delta^i \rho F_1 NDVI \\ -\sum_{i=1}^{N-1} \Delta^i \rho \Delta^i \rho F_2 \\ -\sum_{i=1}^{N-1} \Delta^i \rho \Delta^i \rho F_2 NDVI \end{pmatrix} \quad (2.14)$$

Where A is

$$A = \begin{pmatrix} \sum_{i=1}^{N-1} (\Delta^i \rho F_1)^2 & \sum_{i=1}^{N-1} (\Delta^i \rho F_1)^2 NDVI & \sum_{i=1}^{N-1} \Delta^i \rho F_1 \Delta^i \rho F_2 & \sum_{i=1}^{N-1} \Delta^i \rho F_1 \Delta^i \rho F_2 NDVI \\ \sum_{i=1}^{N-1} (\Delta^i \rho F_1)^2 NDVI & \sum_{i=1}^{N-1} (\Delta^i \rho F_1)^2 NDVI^2 & \sum_{i=1}^{N-1} \Delta^i \rho F_1 \Delta^i \rho F_2 NDVI & \sum_{i=1}^{N-1} \Delta^i \rho F_1 \Delta^i \rho F_2 NDVI^2 \\ \sum_{i=1}^{N-1} \Delta^i \rho F_1 \Delta^i \rho F_2 & \sum_{i=1}^{N-1} \Delta^i \rho F_1 \Delta^i \rho F_2 NDVI & \sum_{i=1}^{N-1} (\Delta^i \rho F_2)^2 & \sum_{i=1}^{N-1} (\Delta^i \rho F_2)^2 NDVI \\ \sum_{i=1}^{N-1} \Delta^i \rho F_1 \Delta^i \rho F_2 NDVI & \sum_{i=1}^{N-1} \Delta^i \rho F_1 \Delta^i \rho F_2 NDVI^2 & \sum_{i=1}^{N-1} (\Delta^i \rho F_2)^2 NDVI & \sum_{i=1}^{N-1} (\Delta^i \rho F_2)^2 NDVI^2 \end{pmatrix} \quad (2.15)$$

We have used the same notation describe in equation (1.28). In this way, each parameter will be estimated inverting this matrix over each year of the dataset but avoiding the classification depending on the NDVI which slows the time processing. This method, as well as the VJB method, provides a product with the same frequency as the observations.

2.3.2. 5parameter Rsqr method

Next, we will consider that the V parameter depends linearly with the NDVI but the R parameter presents a second degree dependency. The R parameter is linked to the geometrical kernel which models the surface roughness. A quadratic dependency of R with the NDVI should describe adequately, for instance, agricultural areas. Along these surfaces low NDVI values describe bare soils where R should be low. The first stages of vegetation growth should increase R (increase the roughness of the surface)

CHAPTER 2

Methodology

until a maximum value. Finally, as crops get denser one may expect R to decrease. Therefore, this method assumption can be written as:

$$V = V_0 + V_1 NDVI \quad (2.16)$$

$$R = R_0 + R_1 NDVI + R_2 NDVI^2 \quad (2.17)$$

Now the derivation of the merit function is

$$C \otimes \begin{pmatrix} V_0 \\ V_1 \\ R_0 \\ R_1 \\ R_2 \end{pmatrix} = \begin{pmatrix} -\sum_{i=1}^{N-1} \Delta^i \rho \Delta^i \rho F_1 \\ -\sum_{i=1}^{N-1} \Delta^i \rho \Delta^i \rho F_1 NDVI \\ -\sum_{i=1}^{N-1} \Delta^i \rho \Delta^i \rho F_2 \\ -\sum_{i=1}^{N-1} \Delta^i \rho \Delta^i \rho F_2 NDVI \\ -\sum_{i=1}^{N-1} \Delta^i \rho \Delta^i \rho F_2 NDVI^2 \end{pmatrix} \quad (2.18)$$

where C is

$$C = \begin{pmatrix} \sum_{i=1}^{N-1} (\Delta^i \rho F_1)^2 & \sum_{i=1}^{N-1} (\Delta^i \rho F_1)^2 NDVI & \sum_{i=1}^{N-1} \Delta^i \rho F_1 \Delta^i \rho F_2 & \sum_{i=1}^{N-1} \Delta^i \rho F_1 \Delta^i \rho F_2 NDVI & \sum_{i=1}^{N-1} \Delta^i \rho F_1 \Delta^i \rho F_2 NDVI^2 \\ \sum_{i=1}^{N-1} (\Delta^i \rho F_1)^2 NDVI & \sum_{i=1}^{N-1} (\Delta^i \rho F_1)^2 NDVI^2 & \sum_{i=1}^{N-1} \Delta^i \rho F_1 \Delta^i \rho F_2 NDVI & \sum_{i=1}^{N-1} \Delta^i \rho F_1 \Delta^i \rho F_2 NDVI^2 & \sum_{i=1}^{N-1} \Delta^i \rho F_1 \Delta^i \rho F_2 NDVI^3 \\ \sum_{i=1}^{N-1} \Delta^i \rho F_1 \Delta^i \rho F_2 & \sum_{i=1}^{N-1} \Delta^i \rho F_1 \Delta^i \rho F_2 NDVI & \sum_{i=1}^{N-1} (\Delta^i \rho F_2)^2 & \sum_{i=1}^{N-1} (\Delta^i \rho F_2)^2 NDVI & \sum_{i=1}^{N-1} (\Delta^i \rho F_2)^2 NDVI^2 \\ \sum_{i=1}^{N-1} \Delta^i \rho F_1 \Delta^i \rho F_2 NDVI & \sum_{i=1}^{N-1} \Delta^i \rho F_1 \Delta^i \rho F_2 NDVI^2 & \sum_{i=1}^{N-1} (\Delta^i \rho F_2)^2 NDVI & \sum_{i=1}^{N-1} (\Delta^i \rho F_2)^2 NDVI^2 & \sum_{i=1}^{N-1} (\Delta^i \rho F_2)^2 NDVI^3 \\ \sum_{i=1}^{N-1} \Delta^i \rho F_1 \Delta^i \rho F_2 NDVI^2 & \sum_{i=1}^{N-1} \Delta^i \rho F_1 \Delta^i \rho F_2 NDVI^3 & \sum_{i=1}^{N-1} (\Delta^i \rho F_2)^2 NDVI^2 & \sum_{i=1}^{N-1} (\Delta^i \rho F_2)^2 NDVI^3 & \sum_{i=1}^{N-1} (\Delta^i \rho F_2)^2 NDVI^4 \end{pmatrix} \quad (2.19)$$

2.3.3. 5parameter Vsqr method

Finally, we consider that R depends linearly with the NDVI but V presents a second degree dependency. The V parameter is linked to the volume kernel which models a collection of randomly located facets absorbing and scattering radiation which represent mainly leaves of canopies and can also model the behavior of dust, fine structures and porosity of bare soils (Roujean et al., 1992). As the vegetation grows and the NDVI get higher values, one may expect V to increase. In this case, the assumption is written as

$$V = V_0 + V_1NDVI + V_2NDVI^2 \quad (2.20)$$

$$R = R_0 + R_1NDVI \quad (2.21)$$

As well as the 5parameter Rsqr method we have included another parameter to the VJB model. Following the same scheme as the previous method, now the derivation of the merit function is

$$B \otimes \begin{pmatrix} V_0 \\ V_1 \\ V_2 \\ R_0 \\ R_1 \end{pmatrix} = \begin{pmatrix} -\sum_{i=1}^{N-1} \Delta^i \rho \Delta^i \rho F_1 \\ -\sum_{i=1}^{N-1} \Delta^i \rho \Delta^i \rho F_1 NDVI \\ -\sum_{i=1}^{N-1} \Delta^i \rho \Delta^i \rho F_1 NDVI^2 \\ -\sum_{i=1}^{N-1} \Delta^i \rho \Delta^i \rho F_2 \\ -\sum_{i=1}^{N-1} \Delta^i \rho \Delta^i \rho F_2 NDVI \end{pmatrix} \quad (2.22)$$

where B is

CHAPTER 2

Methodology

$$B = \begin{pmatrix}
 \sum_{i=1}^{N-1} (\Delta^i \rho F_1)^2 & \sum_{i=1}^{N-1} (\Delta^i \rho F_1)^2 NDVI & \sum_{i=1}^{N-1} (\Delta^i \rho F_1)^2 NDVI^2 & \sum_{i=1}^{N-1} \Delta^i \rho F_1 \Delta^i \rho F_2 & \sum_{i=1}^{N-1} \Delta^i \rho F_1 \Delta^i \rho F_2 NDVI \\
 \sum_{i=1}^{N-1} (\Delta^i \rho F_1)^2 NDVI & \sum_{i=1}^{N-1} (\Delta^i \rho F_1)^2 NDVI^2 & \sum_{i=1}^{N-1} (\Delta^i \rho F_1)^2 NDVI^3 & \sum_{i=1}^{N-1} \Delta^i \rho F_1 \Delta^i \rho F_2 NDVI & \sum_{i=1}^{N-1} \Delta^i \rho F_1 \Delta^i \rho F_2 NDVI^2 \\
 \sum_{i=1}^{N-1} (\Delta^i \rho F_1)^2 NDVI^2 & \sum_{i=1}^{N-1} (\Delta^i \rho F_1)^2 NDVI^3 & \sum_{i=1}^{N-1} (\Delta^i \rho F_1)^2 NDVI^4 & \sum_{i=1}^{N-1} \Delta^i \rho F_1 \Delta^i \rho F_2 NDVI^2 & \sum_{i=1}^{N-1} \Delta^i \rho F_1 \Delta^i \rho F_2 NDVI^3 \\
 \sum_{i=1}^{N-1} \Delta^i \rho F_1 \Delta^i \rho F_2 & \sum_{i=1}^{N-1} \Delta^i \rho F_1 \Delta^i \rho F_2 NDVI & \sum_{i=1}^{N-1} \Delta^i \rho F_1 \Delta^i \rho F_2 NDVI^2 & \sum_{i=1}^{N-1} (\Delta^i \rho F_2)^2 & \sum_{i=1}^{N-1} (\Delta^i \rho F_2)^2 NDVI \\
 \sum_{i=1}^{N-1} \Delta^i \rho F_1 \Delta^i \rho F_2 NDVI & \sum_{i=1}^{N-1} \Delta^i \rho F_1 \Delta^i \rho F_2 NDVI^2 & \sum_{i=1}^{N-1} \Delta^i \rho F_1 \Delta^i \rho F_2 NDVI^3 & \sum_{i=1}^{N-1} (\Delta^i \rho F_2)^2 NDVI & \sum_{i=1}^{N-1} (\Delta^i \rho F_2)^2 NDVI^2
 \end{pmatrix}$$

(2.23)

CHAPTER 3

MATERIAL

In this chapter we describe all the data used in this thesis, which can be divided into two categories: the EODIX field campaign database and the MODIS CMG database.

3.1. EODIX database

3.1.1. Study area and field campaign

Barrax area is located in the south-eastern of Spain, within La Mancha, a plateau 700 m above sea level, and it is in the Western part of the province of Albacete, 28 km from the city of Albacete (39°3'N, 2°60'W). The area is characterised by a flat morphology (differences in elevation range up to 2 m only) and large, uniform land-use units. The dominant cultivation pattern in the 10,000 ha area is approximately 65% dry land

CHAPTER 3

Material

(two-thirds in winter cereals, one-third fallow) and 35% irrigated crops (75% corn, 15% barley and 10% others, including alfalfa) (Moreno et al. 2001). The climate of Barrax is of Mediterranean type, with heavy rainfalls in spring and autumn and dry in summer. It presents a high level of continentality, with quite sudden changes from cold months to warm months and high thermal oscillations in all seasons between the maximum and minimum daily temperatures.

Several remote sensing field campaigns have been carried out over the Barrax test site during the last years, such as SPARC 2004 field campaign (Sobrino et al., 2009), which established Barrax as an appropriate site for the calibration/validation of remote sensing images. This paper is focused on the field campaign developed in the framework of the EODIX project. It was carried out from the 10th to the 13th of June 2011, where extensive in-situ and airborne measurements were carried out over several crops and natural areas.

3.1.2. In situ data

The calibration and validation activities were carried out simultaneously to the airborne overpass. In this paper we distinguish two kind of in situ measurements: surface reflectance and albedo measurements. On one hand, the surface reflectance was retrieved over different surface types of the test area in order to obtain sufficient representative spectra. A transect concurrently to the airborne overpass, starting half an hour before and ending half an hour after, was performed with an ASD Field Spec 3 spectroradiometer. In this way, four different fields were characterized: bare soil, alfalfa, barley and green grass. Additionally, a goniometer was placed in a corn field with a GER 1500 (Figure 3.1a). Nadir measurements retrieved during airborne overpass were also considered in the validation. On the other hand, we estimated albedo measurements from two albedometers located in two meteorological stations, one in a barley field (Figure 3.1b) and the other in a wheat field (Figure 3.1c). Furthermore, the angular surface reflectance measurements from the goniometer were inverted in order to estimate the surface albedo.

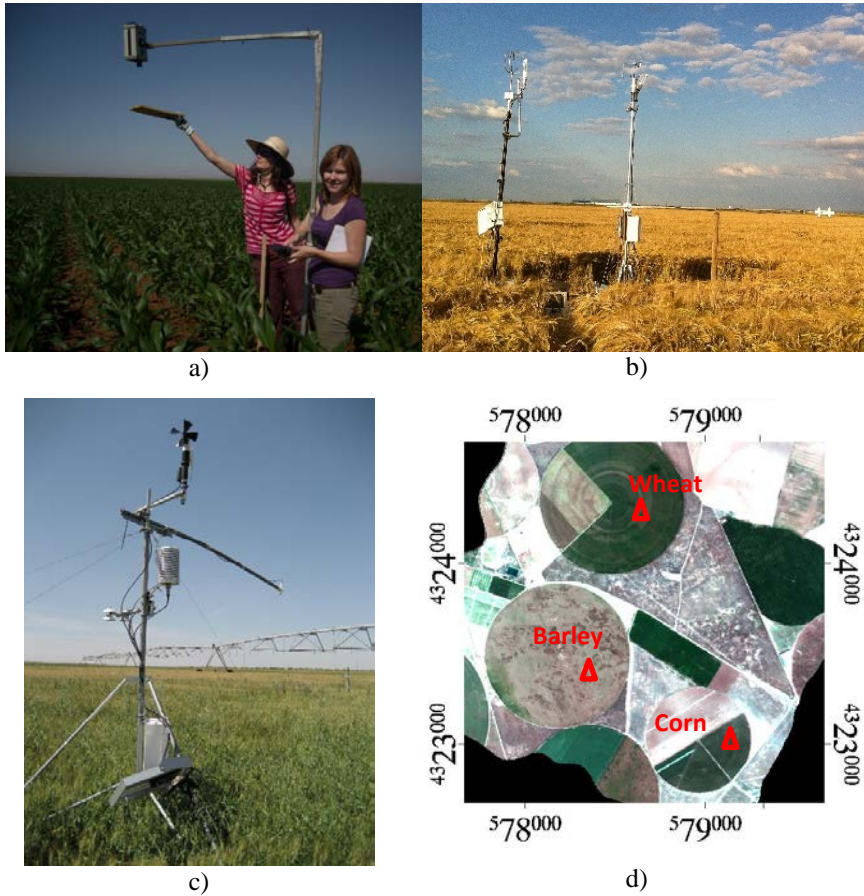


Figure 3.1. In situ albedo measurements from a) a goniometer in a corn field, b) an albedometer located in a meteo station in a barley field and c) an albedometer located also in a meteo station but in a wheat field. D) AHS RGB image and position of the validation points (triangles)

Finally, the aerosol optical thickness needed in the atmospheric correction was retrieved with a CE318 sunphotometer. The CE318 is a commercial sunphotometer designed for the automatic measurement of direct solar irradiance and sky radiance. The unit employed in this campaign

CHAPTER 3

Material

was an extended version, measuring in channels centered at 340, 380, 440, 500, 670, 870, 940, 1020 and 1640 nm, with the 940 nm channel being dedicated to obtain the atmospheric columnar water vapour.

3.1.3. Airborne data

The airborne data used in this work were acquired by the Airborne Hyperspectral Scanner (AHS) (Sobrino et al., 2009), which is an 80-bands airborne imaging radiometer. It is property of INTA and it is operated by technical staff of its Remote Sensing Lab. The AHS is a linescanner with a concept shared with classical airborne line-scanners, like Airborne Thematic Mapper - ATM , MIVIS (Multispectral Infrared and Visible Imaging Spectrometer) and MAS (MODIS Airborne Simulator). The sensor was installed in the INTA's C-212 200 EC-DUQ airplane, and was integrated with a GPS-INS POS/AV 410 V5 provided by Applanix.



Figure 3.2. AHS sensor. Scan-head and operator console and INTA C-212-200 EC-DUQ airplane.

The AHS has 63 bands in the reflective part of the electromagnetic spectrum, 7 bands in the 3 to 5 microns range and 10 bands in the 8 to 13 microns region. AHS has been configured with very distinct spectral performances depending on the spectral region considered. In the VIS/NIR range, bands are relatively broad (28-30 nm): the coverage is continuous from 0.43 up to 1.0 μm . In the SWIR range, there is an isolated band centered at 1.6 μm with a 90 nm width, used to simulate the corresponding band found in a number of satellite missions. Next, there is a set of

continuous, fairly narrow bands (18-19 nm) between 1.9 and 2.5 μm , which are well suited for soil/geologic studies. In the MWIR and LWIR regions, spectral resolution is about 300 to 500 nm, and the infrared atmospheric windows (from 3 to 5 μm and from 8 to 13 μm) are fully covered. These spectral features allow to state that AHS is best suited for multipurpose studies/campaigns, in which a wide range of spectral regions have to be covered simultaneously, especially if no detailed spectroscopy is required. In particular, AHS is a very powerful instrument for thermal remote sensing. The AHS field of view (FOV) is $\pm 45^\circ$, and the instantaneous FOV is 2.5 mrad.

Our study will be centered on the bands equivalent to MODIS. Table 3.1 shows the equivalence that has been considered between both sensors.

Table 3.1. Equivalence between AHS and MODIS bands.

MODIS (nm)	AHS (nm)
Band 1: 645 ± 25	Band 8: 650 ± 14
Band 2: 859 ± 18	Band 15: 856 ± 14
Band 3: 469 ± 10	Band 2: 471 ± 14
Band 4: 555 ± 10	Band 5: 560 ± 14
Band 5: 1240 ± 10	Band 20: 1001 ± 14
Band 6: 1640 ± 12	Band 21: 1588 ± 45
Band 7: 2130 ± 25	Band 35: 2134 ± 45

The data used in this work was acquired in straight line at an altitude of 2545m above sea level the 12th of June of 2011. The resulting data have a ground spatial resolution of 4m. During this campaign several flights were achieved from 9 to 10 UTC in order to obtain enough bidirectional observations to retrieve the BRDF of the test area. Figure 3.3 shows the location of the flight lines. These were planned considering the symmetry of the BRDF in the orthogonal plane.

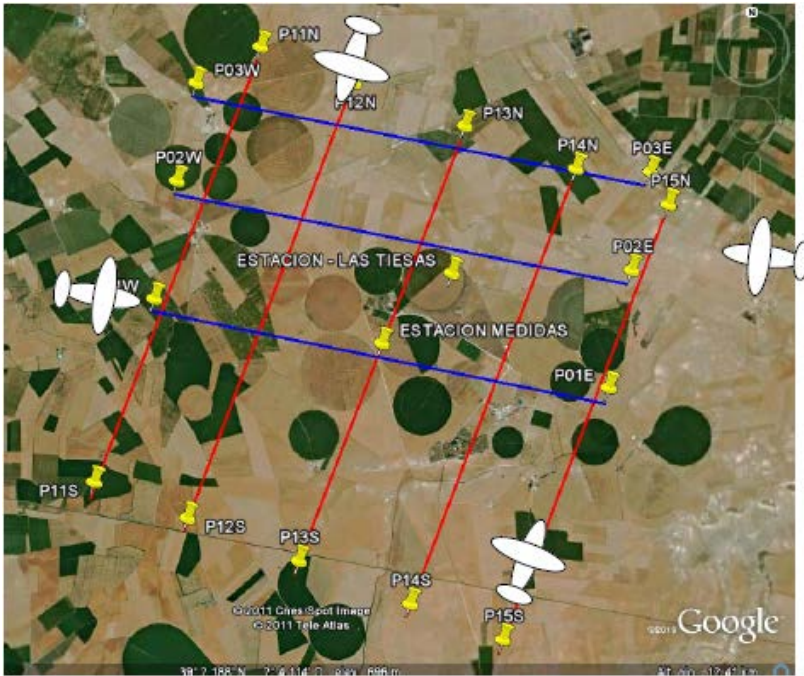


Figure 3.3. Flight lines over the test area the 12th of June 2011.

In order to achieve view zenith angles near to 60° a 15° wedge was placed under the AHS tilting the sensor during all the flights.

3.1.4. Satellite data

The MODIS BRDF/Albedo Model Parameters product (MCD43A1) contains three-dimensional (3D) data sets providing users with weighting parameters for the models used to derive the Albedo and BRDF products (MCD43A3 and MCD43A4) with a spatial resolution of 500 m. The models rely on multi-date, atmospherically corrected, cloud-cleared input data measured over 16-day periods. Both Terra and Aqua data are used in the generation of this product, providing the highest probability for quality input data and designating it as an MCD, meaning Combined, product.

3.2. MODIS CMG database

MODIS (or Moderate Resolution Imaging Spectroradiometer) is a key instrument aboard the Terra (EOS AM) and Aqua (EOS PM) satellites. Terra's orbit around the Earth is timed so that it passes from north to south across the equator in the morning, while Aqua passes south to north over the equator in the afternoon. Terra MODIS and Aqua MODIS are viewing the entire Earth's surface every 1 to 2 days, acquiring data in 36 spectral bands, or groups of wavelengths. These data improve our understanding of global dynamics and processes occurring on the land, in the oceans, and in the lower atmosphere. MODIS is playing a vital role in the development of validated, global, interactive Earth system models able to predict global change accurately enough to assist policy makers in making sound decisions concerning the protection of our environment.

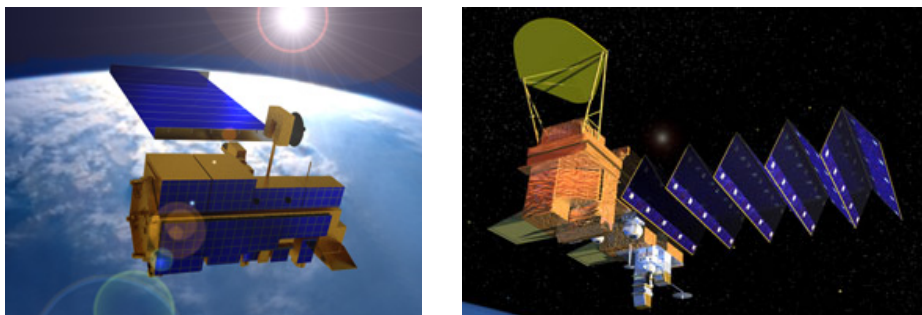


Figure 3.4. Terra (left) and Aqua (right) platforms.

The MODIS instrument provides high radiometric sensitivity (12 bit) in 36 spectral bands ranging in wavelength from 0.4 μm to 14.4 μm . The responses are custom tailored to the individual needs of the user community and provide low out-of-band response. Two bands are imaged at a nominal resolution of 250 m at nadir, with five bands at 500 m, and the remaining 29 bands at 1 km. A ± 55 -degree scanning pattern at the EOS orbit of 705 km achieves a 2,330 km swath and provides global coverage every one to two days.

CHAPTER 3

Material

Table 3.2. MODIS spectral bands.

Band	Bandwidth (nm)	Spatial resolution (m)	Band	Bandwidth (nm)	Spatial resolution (m)
1	620 – 670	250	20	3.660 - 3.840	1000
2	841 – 876	250	21	3.929 - 3.989	1000
3	459 – 479	500	22	3.929 - 3.989	1000
4	545 – 565	500	23	4.020 - 4.080	1000
5	1230 – 1250	500	24	4.433 - 4.498	1000
6	1628 – 1652	500	25	4.482 - 4.549	1000
7	2105 – 2155	500	26	1.360 - 1.390	1000
8	405 – 420	1000	27	6.535 - 6.895	1000
9	438 – 448	1000	28	7.175 - 7.475	1000
10	483 – 493	1000	29	8.400 - 8.700	1000
11	526 – 536	1000	30	9.580 - 9.880	1000
12	546 – 556	1000	31	10.780 - 11.280	1000
13	662 – 672	1000	32	11.770 - 12.270	1000
14	673 – 683	1000	33	13.185 - 13.485	1000
15	743 – 753	1000	34	13.485 - 13.785	1000
16	862 – 877	1000	35	13.785 - 14.085	1000
17	890 – 920	1000	36	14.085 - 14.385	1000
18	931 – 941	1000			
19	915 – 965	1000			

The Scan Mirror Assembly uses a continuously rotating double-sided scan mirror to scan ± 55 degrees and is driven by a motor encoder built to operate at 100 percent duty cycle throughout the 6-year instrument design life. The optical system consists of a two-mirror off-axis afocal telescope, which directs energy to four refractive objective assemblies; one for each of the VIS, NIR, SWIR/MWIR and LWIR spectral regions to cover a total spectral range of 0.4 to 14.4 μm .

A high-performance passive radiative cooler provides cooling to 83K for the 20 infrared spectral bands on two HgCdTe Focal Plane Assemblies (FPAs). Photodiode-silicon readout technology for the visible and near infrared provides unsurpassed quantum efficiency and low-noise readout with exceptional dynamic range. Analog programmable gain and offset and FPA clock and bias electronics are located near the FPAs in two dedicated electronics modules, the Space-viewing Analog Module (SAM) and the Forward-viewing Analog Module (FAM). A third module, the Main Electronics Module (MEM) provides power, control systems, command and telemetry, and calibration electronics.

The system also includes four on-board calibrators as well as a view to space: a Solar Diffuser (SD), a v-groove Blackbody (BB), a Spectroradiometric calibration assembly (SRCA), and a Solar Diffuser Stability Monitor (SDSM).

The first MODIS Flight Instrument, ProtoFlight Model or PFM, is integrated on the Terra (EOS AM-1) spacecraft. Terra successfully launched on December 18, 1999. The second MODIS flight instrument, Flight Model 1 or FM1, is integrated on the Aqua (EOS PM-1) spacecraft; it was successfully launched on May 4, 2002. These MODIS instruments offer an unprecedented look at terrestrial, atmospheric, and ocean phenomenology for a wide and diverse community of users throughout the world.

The MODIS Climate Modeling Grid (CMG) surface reflectance data (M{O/Y}DCMG) are gridded in the linear latitude, longitude projection at 0.05° resolution. Science Data Sets provided for this product include surface reflectance values for Bands 1–7, brightness temperatures for Bands 20, 21, 31, and 32, solar and view zenith angles, relative azimuth angle, ozone, granule time, quality assessment, cloud mask, aerosol optical thickness at 550 nm and water vapor content. These data were used with two objectives:

1. to analyze the influence of the anisotropy of the surface in the atmospheric correction

CHAPTER 3

Material

2. to evaluate the difference of considering MODIS MCD43 product instead of using the inversion method proposed by Vermote et al. (2003) or the improvements proposed in this thesis.

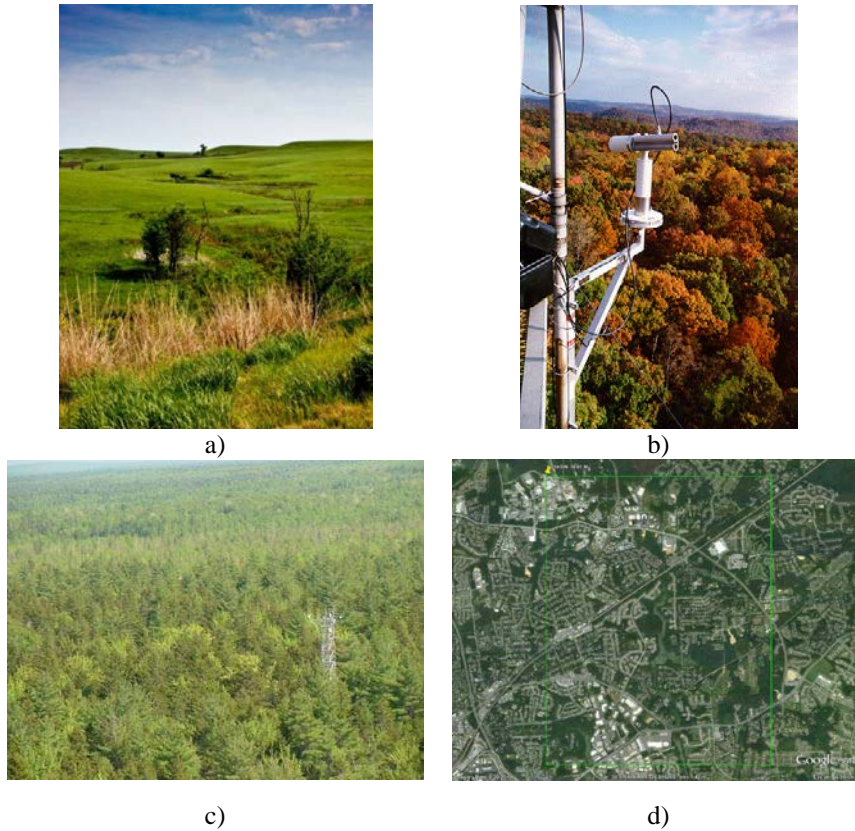


Figure 3.4. Study sites: a) KONZA EDC, b) Walker Branch, c) Howland and d) GSFC.

In the first study we analyzed daily data from both Aqua and Terra platforms between 2003 and 2006 at four different Aeronet sites (each one of them corresponded to one CMG pixel) located in the United States of America (Figure 3.4): KONZA EDC (39.10°N , 96.60°W) which is a prairie region whose land cover type is grass, Walker Branch (36.0°N , 84.30°W) a broadleaf forest, Howland (45.20°N , 68.75°W) a boreal-northern hardwood

transitional forest and GSFC (39.00°N, 76.85°W) which is a mixture of vegetation and urban residential areas. Additional information about these sites can be found in Morisette et al. (2002).

In the second study we worked with daily data from both Aqua and Terra platforms over a European scene from 2002 through 2011. The MODIS product considered in this study was the MCD43 BRDF/Albedo Snow-free Quality product (MCD43C2). Analogously to the MCD43A1 product described in the previous section, it contains the weighting parameters for the models used to derive the Albedo and Nadir BRDF-Adjusted Reflectance (NBAR) products (MCD43C3 and MCD43C4) but describing only snow-free conditions with a spatial resolution of 0.05°.

Additionally, we worked with the Land Cover Type Yearly CMG which is a lower spatial resolution (0.05°) product and provides the dominant land cover type and also the sub-grid frequency distribution of land cover classes. The CMG product (MCD12C1) is derived using the same algorithm that produces the V005 Global 500 m Land Cover Type product (MCD12Q1). It contains three classification schemes, which describe the land cover properties derived from observations spanning a year's input of Terra and Aqua MODIS data. The primary land cover scheme, which we consider in this paper, identifies 17 land cover classes defined by the International Geosphere Biosphere Programme (IGBP), which includes 11 natural vegetation classes, 3 developed and mosaicked land classes, and 3 non-vegetated land classes.

CHAPTER 3
Material

CHAPTER 4

RESULTS

This chapter presents the results obtained in this thesis. Analogously to the methodology chapter, we divide the results into three sections addressing specifically one of the objectives developed in this thesis.

4.1. ANISOTROPY INFLUENCE STUDY

We first analyze the influence of considering the surface anisotropy instead of the Lambertian assumption in the atmospheric correction scheme. Figure 4.1 shows the V and R values in band 2 versus the NDVI classes that were estimated for each area in order to apply the VJB methodology.

CHAPTER 4

Results

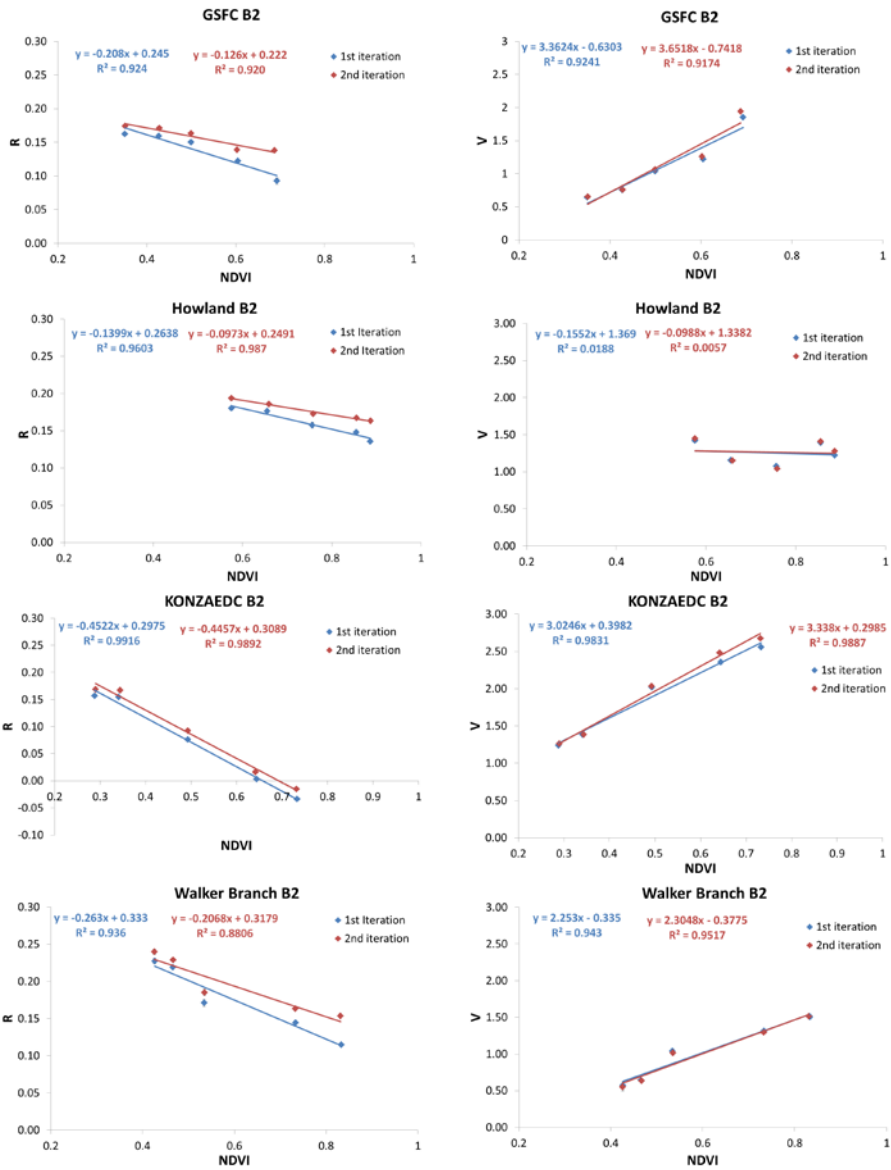


Figure 4.1. Plots of the V and R parameters in band 2 versus the NDVI classes considered in each area in order to apply the VJB methodology.

The plots show the expected increase of V and decrease of R with increasing NDVI. Additionally, the linear fit that allows the estimation of V and R parameters for each NDVI value through the time series present a good correlation coefficient for every area except in case the V parameter in the Howland site. This particular area also presents the lowest variability of NDVI. Nevertheless, the standard deviation of the data was low and equal to 0.01. These plots also show that the difference between the first iteration and the second iteration is more noticeable in the R parameter than in V .

Figure 4.2 presents the temporal evolution of V and R in the particular case of KONZA EDC.

In this study we analyzed every MODIS band in the VNIR spectral range (band 1 to band 7), though, we just include band 1 (centered at 646.3 nm), band 2 (centered at 858.5 nm) and band 4 (centered at 553.7 nm) results, considering each one as representative of the red, near infrared and green spectral region respectively. We have not included the blue band results as this band is used primarily for the aerosol retrievals (Vermote & Kotchenova, 2008). In this figure the first iteration (black) is referred to $BRDF_1$ parameters and the second iteration Coddington, to $BRDF_2$ parameters.

These figures show that the difference between $BRDF_1$ and $BRDF_2$ is greater in bands 1 and 4 than in band 2. Also it is more noticeable in the parameter R than V . The analysis of the other bands leads to similar conclusions. The R parameter shows slightly negative values in band 2 during the summer. This is because the numerical solution of the least squares fit sometimes provides slightly negative (and unphysical) k_2 values. This parameter, which determines the magnitude of geometric and shadowing effects, is significant only when LAI is weak (<0.5), and becomes negligible for larger LAI (Roujean et al., 1992).

CHAPTER 4

Results

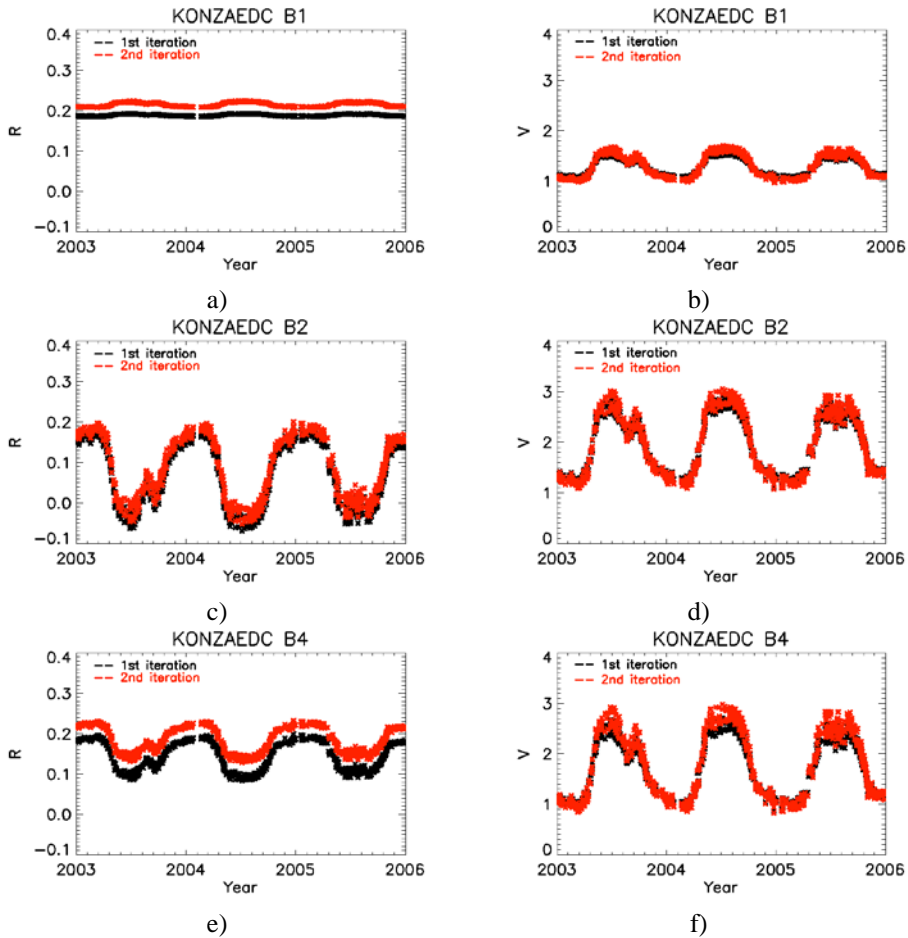


Figure 4.2. Temporal evolution of R and V.

Figure 4.3 shows the pixel-by-pixel comparison of the BRDF corrected reflectance (ρ_2 and ρ_3) versus the Lambertian reflectance (ρ_1) for GSFC site. We divided the analysis into three particular cases: high amount of aerosols (AOT > 0.3), forward scattering direction (relative azimuth angles greater than 90° but less than 270°) and backward scattering direction (relative azimuth angles less than 90° and greater than 270°). The plots show a slope of regression near to one and a good correlation between the BRDF

corrected and Lambertian reflectances. However, the slope as well as the error slightly increases for higher amounts of aerosols.

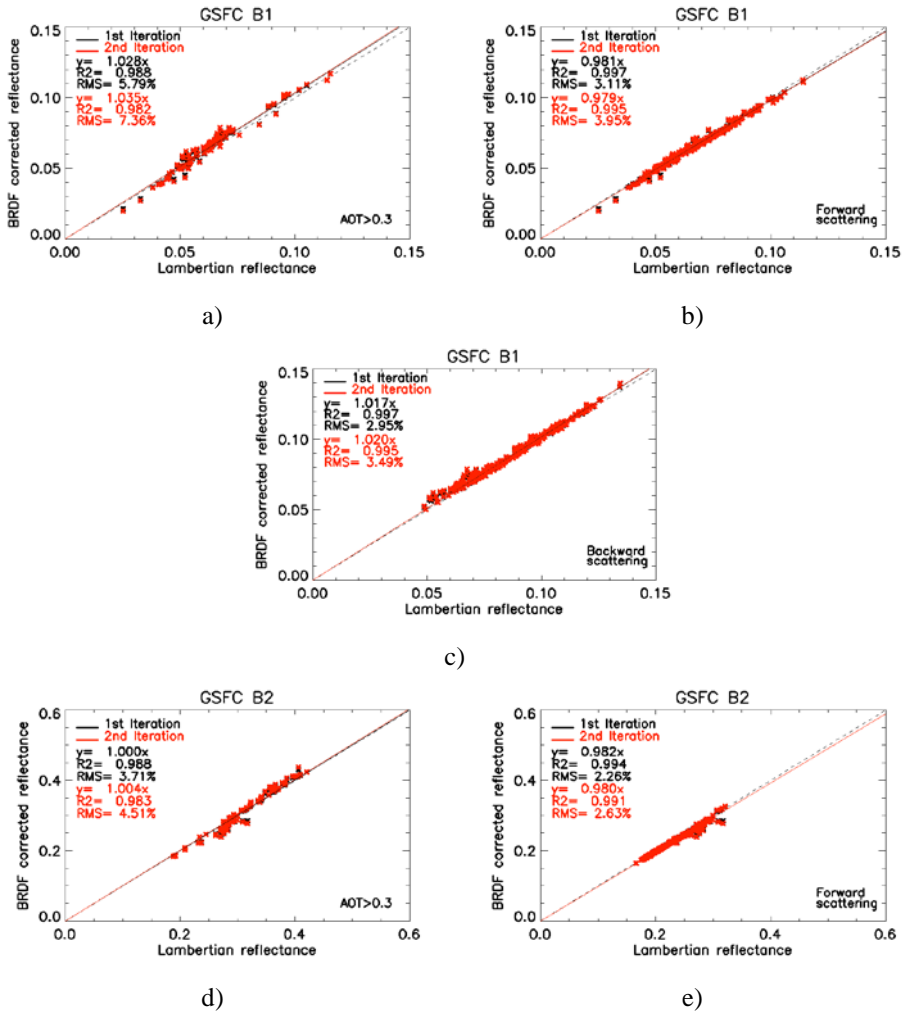


Figure 4.3. Pixel-by-pixel comparison of BRDF corrected reflectance obtained from BRDF1 (first iteration, black) and from BRDF2 (second iteration, red) versus the Lambertian reflectance for GSFC site.

CHAPTER 4

Results

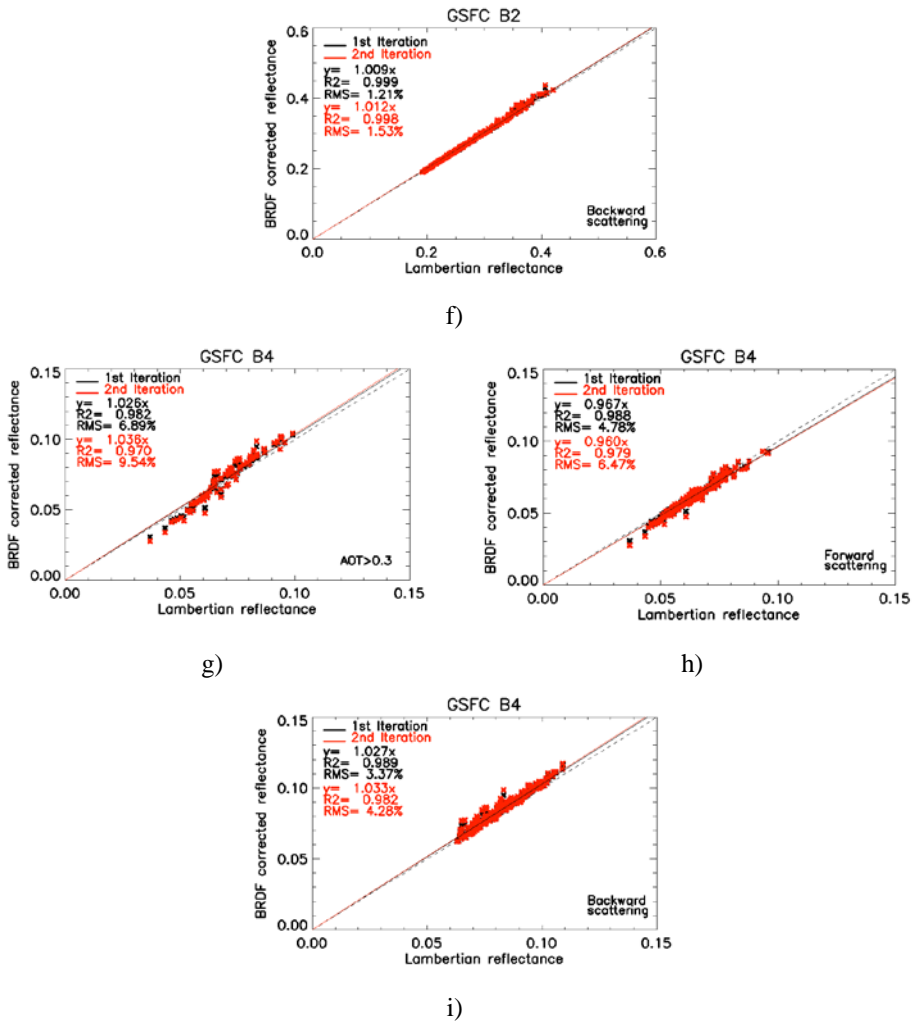


Figure 4.3. Pixel-by-pixel comparison of BRDF corrected reflectance obtained from BRDF1 (first iteration, black) and from BRDF2 (second iteration, red) versus the Lambertian reflectance for GSFC site (continued).

Table 4.1 shows the RMS relative error (see eq. 2.1) for every site.

Table 4.1. Relative RMS when estimating the surface reflectance from a Lambertian assumption versus considering BRDF₁ (ρ_2) or BRDF₂ (ρ_3).

RMS (%)			AOT>0.3	<i>Forward Scattering</i>	<i>Backward Scattering</i>
Howland	B1	ρ_2	7.54	3.85	2.01
		ρ_3	8.79	4.52	2.21
	B2	ρ_2	4.21	1.84	0.95
		ρ_3	4.66	2.00	1.06
	B4	ρ_2	9.53	5.91	2.81
		ρ_3	12.10	7.49	3.34
KONZA EDC	B1	ρ_2	6.26	3.28	2.21
		ρ_3	7.14	3.77	2.52
	B2	ρ_2	4.03	2.05	0.57
		ρ_3	4.31	2.18	0.70
	B4	ρ_2	7.61	4.96	2.36
		ρ_3	9.29	6.04	2.98
GSFC	B1	ρ_2	5.79	3.11	2.95
		ρ_3	7.36	3.95	3.49
	B2	ρ_2	3.71	2.26	1.21
		ρ_3	4.51	2.63	1.53
	B4	ρ_2	6.89	4.78	3.37
		ρ_3	9.54	6.47	4.28
Walker Branch	B1	ρ_2	5.80	2.96	2.86
		ρ_3	6.90	3.49	3.26
	B2	ρ_2	3.46	1.92	1.28
		ρ_3	3.98	2.11	1.51
	B4	ρ_2	7.36	4.92	3.47
		ρ_3	9.48	6.18	4.18

CHAPTER 4

Results

At first glance, the error committed when assuming a Lambertian surface is higher in band 1 (between 2% and 9%) and in band 4 (between 3% and 12%) than in band 2 (between 0.7% and 5%), which is in agreement with the variation in V and R between iterations presented in Figure 4.2. The difference between ρ_2 and ρ_3 is less significant in bands 1 and 2 than band 4, where the difference is more noticeable and leads to the highest errors in ρ_3 . Besides, the particular case of high amount of aerosols shows the highest errors when compared to the forward and backward scattering errors. Finally, regarding the two scattering directions, the forward scattering shows the highest errors. This might be because the atmosphere (especially the molecular scattering) scatters at large angles away from the forward direction (Vermote et al., 2006). Comparing the errors committed depending on each surface we observe that the highest errors correspond to the Howland pixel while the other surfaces present similar results. This shows that the anisotropy correction does not depend on the heterogeneity of the surface (since GSFC is the most heterogeneous pixel and has similar errors to Walker Branch and KONZA EDC, which were homogeneous). Howland is situated at the north of the United States and during the winter has limited observations because of clouds cover. Therefore, the particular case of Howland highest errors should be due to its limited observations and bad atmospheric conditions.

Next, we studied the impact of the BRDF correction on the NDVI. Figure 4.4 shows the NDVI values obtained from $BRDF_2$ and $BRDF_3$ correction versus the NDVI estimated considering the Lambertian assumption in case of the GSFC site. The plots show a good agreement between the different approaches with slopes near to one and low RMS. In this case, we did not observe any significant difference between the RMS values depending on the forward or backward scattering or for high aerosol amount, although this last case presented slightly higher errors. Additionally, the RMS between the first iteration and the second iteration (that is, considering $BRDF_2$ or $BRDF_3$) showed similar values.

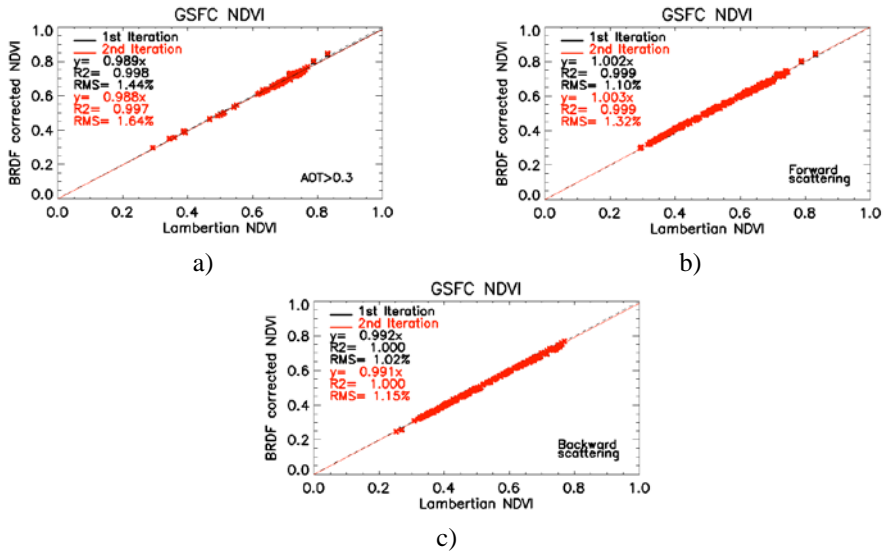


Figure 4.4. Pixel-by-pixel comparison of BRDF corrected NDVI obtained from BRDF₁ (first iteration, black) and from BRDF₂ (second iteration, red) versus the Lambertian NDVI for GSFC site.

Table 4.2 shows the relative RMS estimated for every site.

Table 4.2. Relative RMS when estimating the NDVI from a Lambertian assumption versus considering BRDF₁ (NDVI₂) or BRDF₂ (NDVI₃).

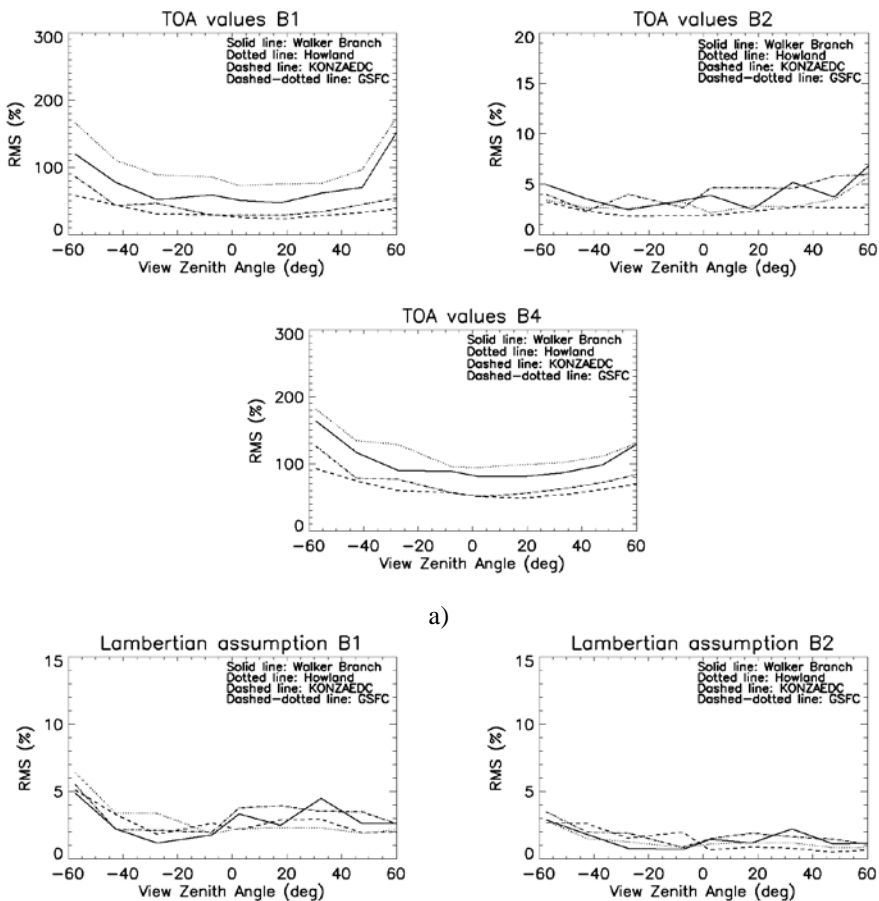
RMS (%)		AOT>0.3	Forward Scat.	Backward Scat.
Howland	NDVI ₂	0.6	0.7	0.4
	NDVI ₃	0.7	0.8	0.5
KONZA EDC	NDVI ₂	2.2	1.4	1.1
	NDVI ₃	2.6	1.7	1.3
GSFC	NDVI ₂	1.4	1.1	1.0
	NDVI ₃	1.6	1.3	1.2
Walker Branch	NDVI ₂	0.6	0.8	0.7
	NDVI ₃	0.7	0.9	0.8

CHAPTER 4

Results

KONZA EDC presented the highest errors in case of high aerosol amounts which reached 2.6%. However, excepting this particular situation we obtained RMS values around 1%.

In order to evaluate the atmospheric effect, analogously to Hu et al. (1999), Figure 4.5 displays the relative RMS between ρ_3 (considering it as the nearest to the true value) and (a) the top of atmosphere (TOA) reflectance, (b) ρ_1 and (c) ρ_2 versus the view zenith angle and for each zone.



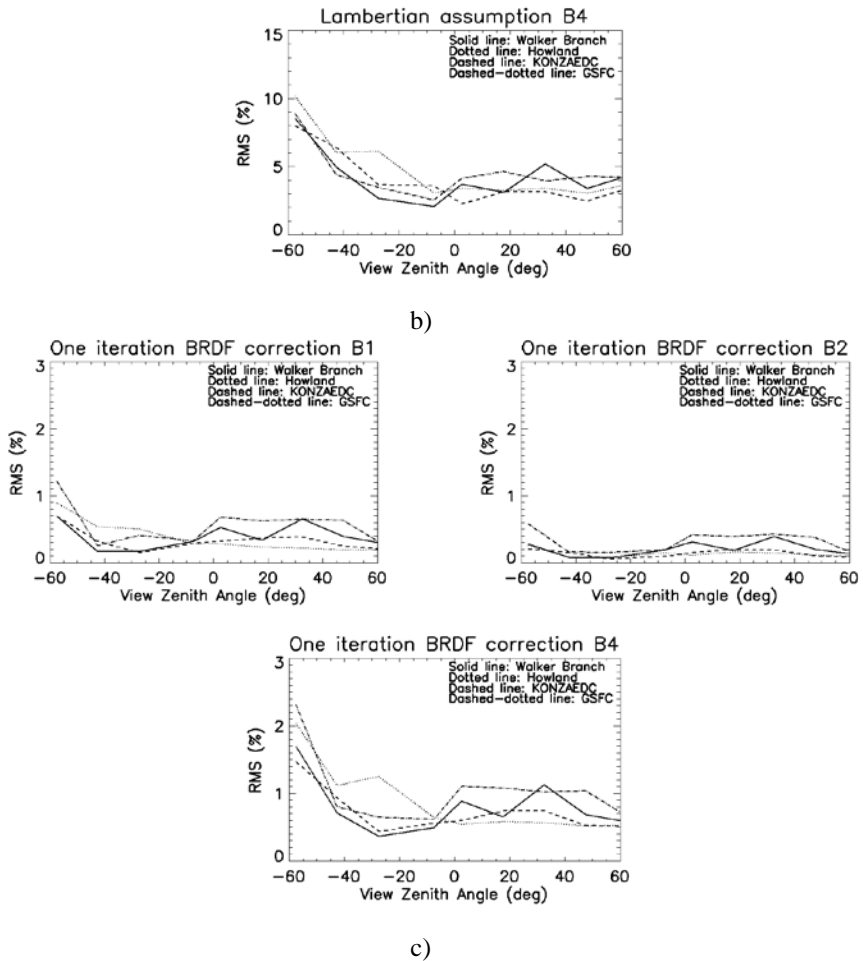


Figure 4.5. Relative RMS between ρ_3 (considering it as the nearest to the true value) and (a) the top of atmosphere (TOA) reflectance, (b) ρ_1 and (c) ρ_2 versus the view zenith angle and for each zone.

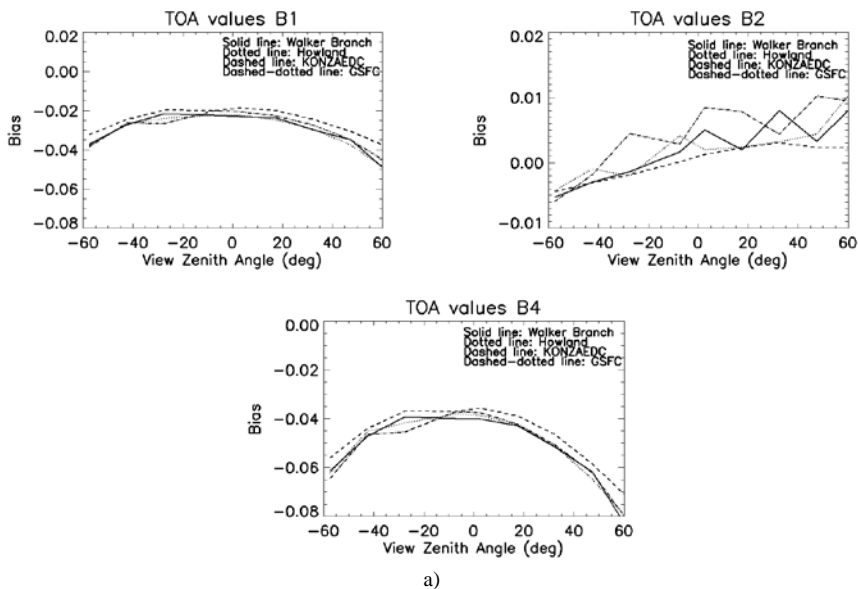
From these plots, we can see that the atmospheric effect is larger in band 4 (green) than in band 1 (Coddington et al. (2008)) and mostly than band 2 (near infrared). This is consequence of the decreasing of the atmospheric scattering when the wavelength increases and also of the larger effect of the

CHAPTER 4

Results

atmospheric path radiance on the small reflectances of vegetated land covers (Walker Branch, Howland and KONZA EDC) in the red and green bands relative to its effect on their larger reflectances in the near infrared. Additionally, focusing on bands 1 and 4, we noticed higher errors in the forward scattering direction (negative view zenith angles) than in the backscattering direction, as we have seen in Table 4.1. This conclusion agrees with Lee and Kaufman (1986) results which showed that the largest differences between the upward emerging radiance for a Lambertian surface versus for a non-Lambertian surface occurred at backscattering region. However, they defined the backscattering direction for relative azimuth angles of 180° , which corresponds in our notation to the forward scattering direction. Centering our attention on the magnitude of the relative RMS obtained in Figure 4.5b and Table 4.1, the errors are no higher than 8% in the red band and no higher than 12% in the green band. These values, though, are lower than Wang et al. (2010) results, which showed errors as high as 15% in the red band and 40% in the green band.

Figure 4.6 shows the bias between ρ_3 and the TOA reflectance (a), ρ_1 (b) and ρ_2 (c) versus the view zenith angle for each zone.



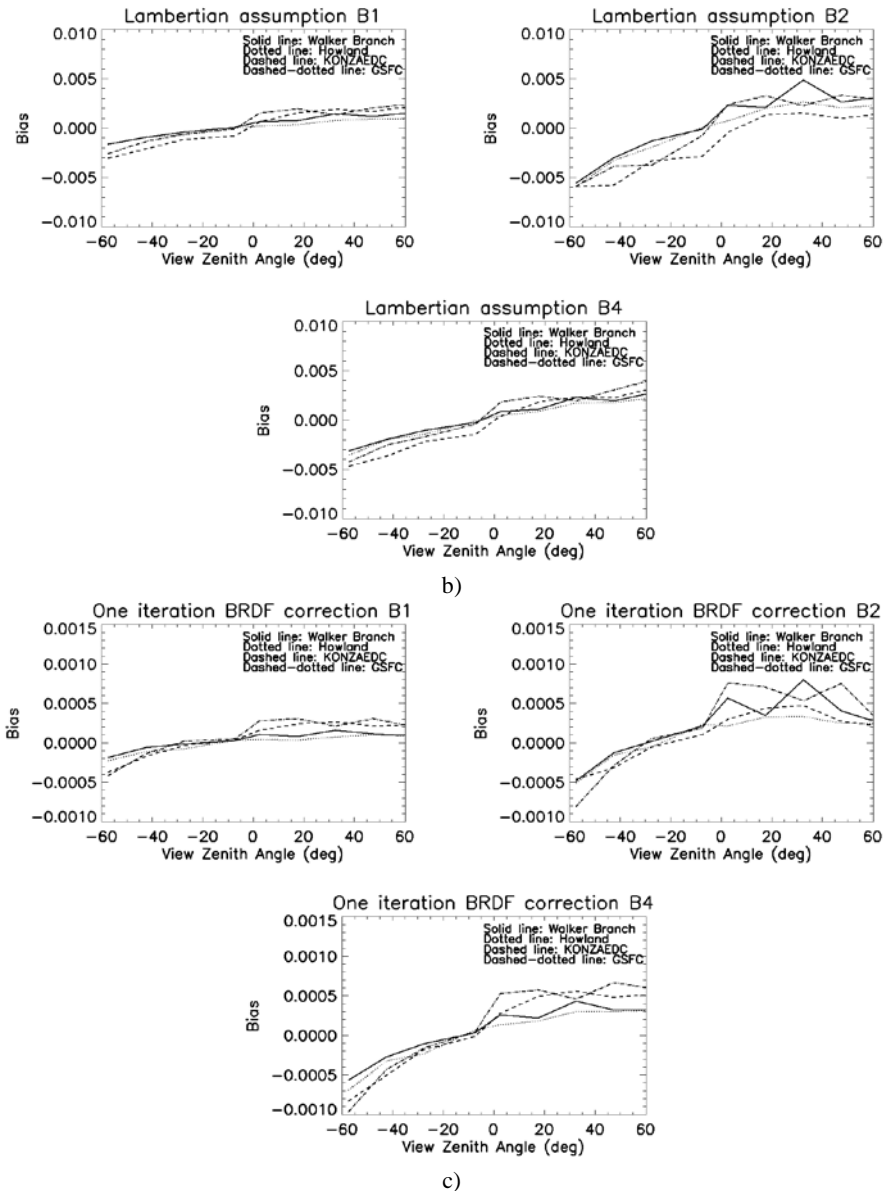


Figure 4.6. Bias obtained considering the average of ρ_3 minus a) Top of Atmosphere reflectances, b) ρ_1 and c) ρ_2 versus the view zenith angle and for each zone (continued).

CHAPTER 4

Results

Band 4 presents the highest bias for TOA reflectances. For every zone and for bands 1 and 4, we obtain negative values that decrease (increase in absolute magnitude) for off-nadir view zenith angles. These results show that TOA reflectances overestimate the true reflectance value (ρ_3). However, band 2 presents much lower bias than bands 1 and 4 in TOA reflectances and leads to positive values. This is another result that evidences the larger atmospheric effect over the visible region than the near infrared. Furthermore, focusing on (b) and (c) plots we observe negative bias for negative view zenith angles (backscattering) and vice versa. These results lead to equivalent conclusions to Lee and Kaufman (1986), where they showed that the upward radiance for large solar zenith angles, in the backscattering direction (equivalent in our notation to the forward scattering) is larger for a Lambertian surface than for a non-Lambertian surface (overestimation). This effect also occurs (Figure 4.6c) in case of considering the first iteration of the BRDF in the surface reflectance estimation (ρ_2) but the bias is reduced considerably. This underestimation at the forward scattering direction ($\rho_1 < \rho_3$) can be caused by the Ross-Thick component of the BRDF model since it is based on volumetric scattering of leaves which have zero transmittance. This would especially have an impact in the near infrared.

Finally, we study the influence of considering the surface anisotropy in the surface albedo estimation. In ideal conditions, albedo (an integrated function of BRDF) should not be highly impacted by the Lambertian errors because, as we have seen in Figure 4.6b, the surface reflectance overestimation ($\rho_1 > \rho_3$) at negative view angles will be compensated by its underestimation ($\rho_1 < \rho_3$) at positive view angles. Table 4.3 shows the relative RMS and the bias of the white sky albedo between its estimation from $BRDF_2$ (albedo₂) versus considering $BRDF_1$ (albedo₁) for every site.

Analogously to Table 4.1, band 2 presents lower errors than band 1 and 4 but, in this case, the difference is less significant than in case of the surface reflectance. Additionally, the high amount of aerosols provides the highest RMS. The results show errors in the white sky albedo from 1.5 to

5.0% both in the red and the green bands and from 0.7 to 3.0% in the near infrared. Regarding the bias, we obtained negative values at every site and band, which implies that albedo_1 is greater than albedo_2 . Additionally, band 2 shows the highest values which is due to its higher albedo than bands 1 and 4 in the case of vegetated sites.

Table 4.3. Relative RMS when estimating the white sky albedo from BRDF_2 (albedo_2) versus considering BRDF_1 (albedo_1).

RMS (%)		AOT>0.3	<i>Forward Scattering</i>	<i>Backward Scattering</i>	Bias ($\text{albedo}_2 - \text{albedo}_1$) $\cdot 10^{-4}$
Howland	B1	4.99	2.24	1.66	-0.01
	B2	2.90	1.12	0.79	-11.60
	B4	4.69	2.01	1.24	-0.69
KONZA EDC	B1	3.83	1.35	0.84	-4.51
	B2	3.11	1.21	0.86	-22.20
	B4	3.92	1.51	0.99	-6.44
GSFC	B1	2.19	1.30	1.51	-0.87
	B2	1.78	1.06	1.27	-10.30
	B4	2.09	1.36	1.58	-1.27
Walker Branch	B1	2.32	1.34	1.44	-0.85
	B2	1.88	1.11	0.95	-12.90
	B4	2.60	1.58	1.45	-1.54

Figure 4.7 displays the relative RMS and the bias of the white sky broad band albedo between albedo_2 and albedo_1 . From these plots we get RMS errors between 0.5 and 1.5% but there is no tendency depending on the view zenith angle. Furthermore, we obtain bias between -0.0015 and 0, being their values mostly negative independently of the site and the view zenith angle. This implies that in almost every case albedo_1 is greater than albedo_2 , which is in contrast with the Wang et al. (2010) results, which

CHAPTER 4

Results

showed that “Lambertian” albedo is slightly lower than the BRDF corrected albedo. In addition, we do not observe any dependency with the view zenith angle.

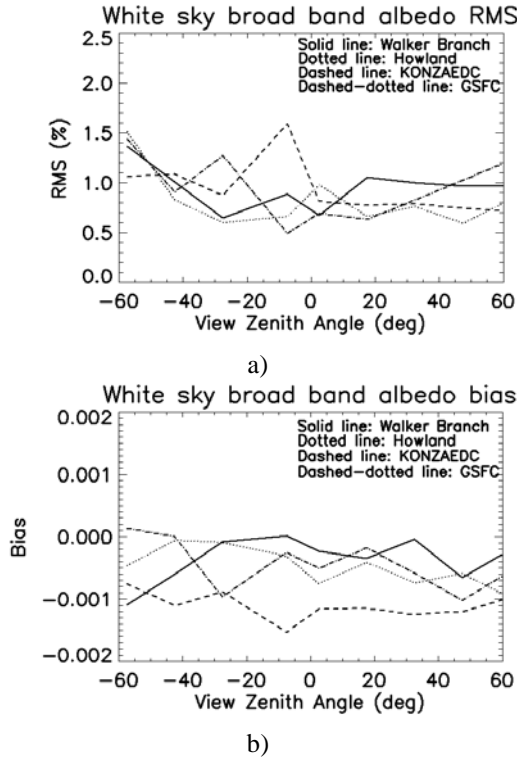


Figure 4.7. White sky broad band albedo relative RMS (a) and bias (b) obtained comparing the albedo_2 to albedo_1 for each site

Table 4.4 shows the relative RMS and the bias between albedo_2 and albedo_1 for every view zenith angle. The table shows similar RMS for every site of around the 1%, which agrees with Hu et al. (1999) and Lyapustin (1999) results. Additionally, we obtained a bias of around $-4 \cdot 10^{-4}$ in every zone except for KONZAEDC, which presents a higher bias of $10.3 \cdot 10^{-4}$.

Table 4.4. RMS and bias of the white sky broad band albedo when comparing albedo₁ to albedo₂

	Howland	KONZA EDC	GSFC	Walker Branch
RMS (%)	1.00	0.97	1.07	1.01
Bias (albedo₂- albedo₁)	$-4.7 \cdot 10^{-4}$	$-10.3 \cdot 10^{-4}$	$-3.9 \cdot 10^{-4}$	$-4.5 \cdot 10^{-4}$

As a general conclusion, the Lambertian assumption leads to a maximum of 1% RMS in the albedo estimation consequently in the following studies, where we study BRDF algorithms and BRDF inversion methods through the albedo, we assumed the Lambertian approximation.

4.2. TEST OF THE MCD43 SURFACE ALBEDO ESTIMATION

In this section we evaluate the MCD43 product over a heterogeneous agricultural area through the blue sky albedo estimation. In this way, we take advantage of airborne and in situ measurements carried out during the EODIX campaign.

4.2.1. Atmospheric correction

First of all, airborne images were atmospherically corrected with the 6S radiative transfer code (Vermote et al., 2006). Following the previous section results, in this step we considered the surface as uniform and Lambertian. We just corrected the AHS bands equivalent to MODIS bands (Table 3.1). Surface reflectance images were tested with in situ measurements. A total of five different surfaces were taken into account: corn, bare soil, alfalfa, barley and green grass. Since each surface was observed by the AHS with different angles and in situ measurements were retrieved at nadir, we only considered airborne images that observed each validation point with view zenith angles lower than 25°.

Figure 4.8 displays the airborne versus the in situ surface reflectance considering all flights (with this condition) and all variable surface types. In

CHAPTER 4

Results

this graph, singular in situ values presents different airborne estimations and, among them, the most dispersed points correspond to higher view zenith angles. Overall, every data presented a good correlation with in situ values.

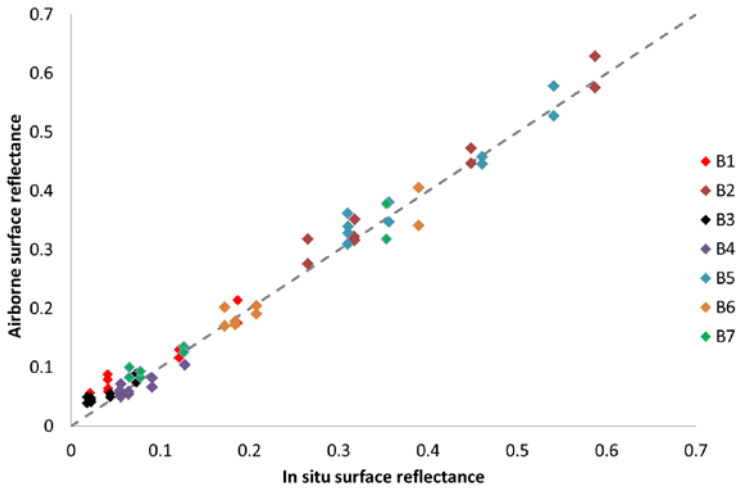


Figure 4.8. Airborne surface reflectance test over in situ measurements for each band.

Table 4.5 presents the Bias, standard deviation and Root Mean Square Error (RMSE).

Table 4.5. Test of surface reflectance airborne images.

	Bias	Stddev	RMSE
Band 8 (Band 1 MODIS)	0.02	0.019	0.03
Band 15 (Band 2 MODIS)	0.015	0.02	0.03
Band 2 (Band 3 MODIS)	0.017	0.009	0.02
Band 5 (Band 4 MODIS)	-0.006	0.013	0.014
Band 20 (Band 5 MODIS)	0.012	0.02	0.03
Band 21 (Band 6 MODIS)	-0.004	0.02	0.02
Band 35 (Band 7 MODIS)	0.007	0.019	0.02

Generally, the table shows RMSE around 0.03. The lowest error corresponds to MODIS band 4 with a RMSE of 0.014. These results show the good performance of the atmospheric correction.

4.2.2. Airborne albedo estimation

Once tested the surface reflectivity airborne images, we obtained the BRDF and tested them with ground data. In the material section, Figure 3.1d showed the position of the three validation points considered: two meteorological stations (one in a barley field and the other in a wheat field) and a goniometer in a corn field.

Figure 4.9 shows the airborne blue sky broadband albedo estimation versus the in situ albedo. Since eight different flights were performed within one hour (from 9 am until 10 am UTC), we averaged the albedo obtaining three different measurements that represented the albedo that corresponded to 9, 9:30 and 10. We must emphasize that the albedo of the corn field, which was derived from the goniometer corresponds to the visible blue sky albedo, since the GER radiometer (used in the goniometer) reaches 1500 nm only. Thus, it was compared to airborne visible blue sky albedo. Additionally, the in situ albedo of the corn was estimated with both with the RTLSR model and with the RTLSR-HS model.

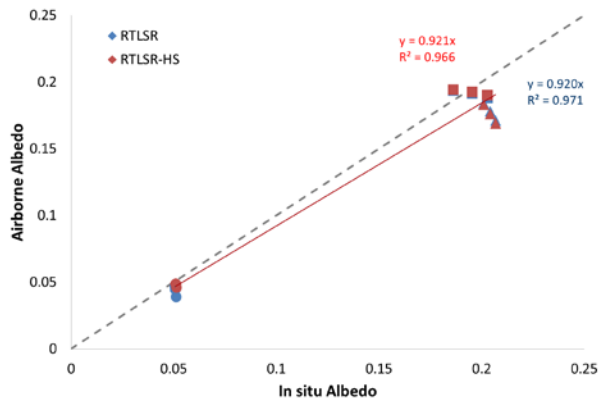


Figure 4.9. Albedo test in the corn (circles), wheat (squares) and barley (triangles) fields.

CHAPTER 4

Results

From the plot we observe that both models present similar results with slopes near to one and high correlation coefficients which show a good agreement between airborne and in situ albedo values. The barley field presents the worst correlation, where both models underestimate the in situ measurement. The greatest difference between both models corresponds to the corn field. While the RTLSR-HS model provided a good estimation, the RTLSR model underestimated it slightly. Finally, both the RTLSR and the RTLSR-HS models presented a RMSE of 0.018.

Figure 4.10 shows a broadband albedo airborne image estimated with both methods. The images show that the RTLSR method tends to underestimate the left side of the image and this is corrected in the RTLSR-HS image. Additionally, centering the attention in the top of the images we observe higher values of albedo, which was associated to the Hot Spot effect. This effect seems to be less influent in the RTLSR-HS image.

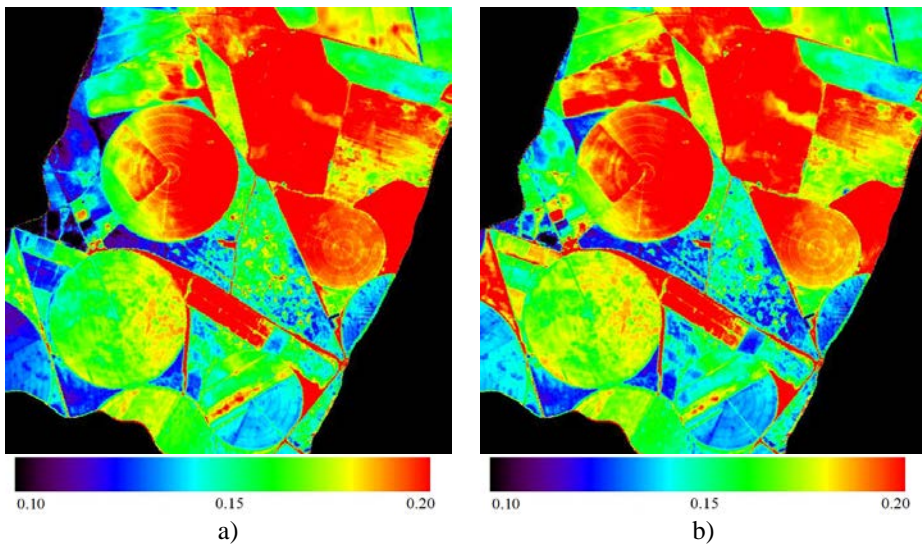


Figure 4.10. Broadband blue sky albedo airborne image using a) the RTLSR model and b) the RTLSR-HS model

4.2.3. Aggregation

After testing AHS albedo images, we aggregated them into the MODIS spatial resolution (500m). We assume a linearly average of the high resolution AHS image in order to compare directly both products.

Figure 4.11 shows an example of the difference between AHS and MODIS resolutions and the location of the MODIS nearest pixels to in situ albedo measurements. The equivalence between the MODIS pixels over the AHS image shows that in case of the barley field, the MODIS pixel was homogeneous, while in case of the wheat and corn fields they were heterogeneous.

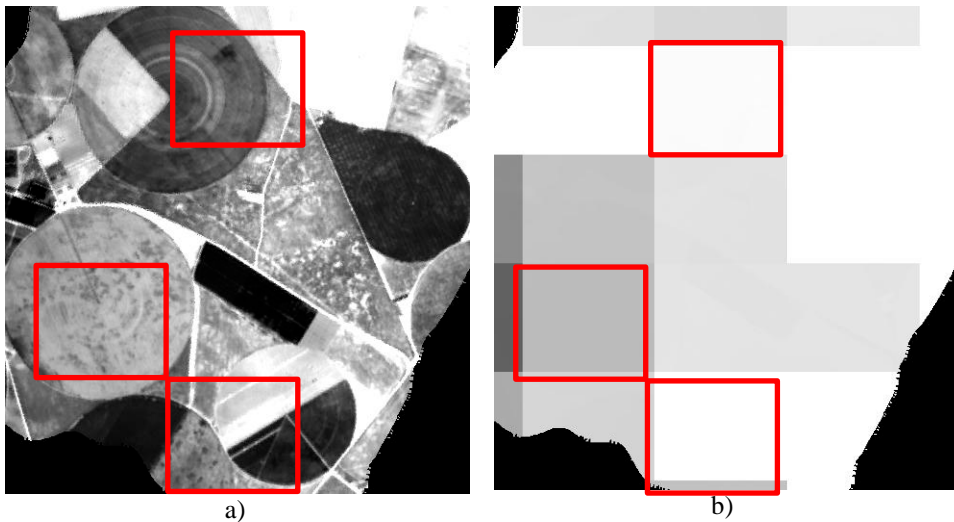


Figure 4.11. (a) Blue-sky broadband albedo airborne image from the RTLSR model. Squares: equivalence between MODIS pixels (b) and AHS area averaged (a).

Figure 4.12 presents the albedo derived from the MODIS product versus the albedo estimated from AHS images for these pixels.

CHAPTER 4

Results

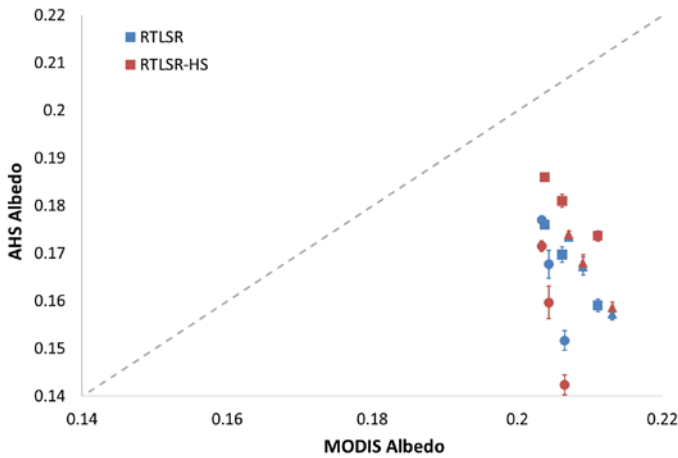


Figure 4.12. MODIS and AHS albedo comparison of the nearest pixel to the corn (circles), wheat (squares) and barley (triangles) fields.

First, we observe that the MODIS albedo did not change significantly between each surface. In case of the AHS albedo derived from the RTLSR BRDF model the difference between each pixel was lower than the RTLSR-HS model. Secondly, MODIS albedo estimations were higher than AHS albedos. The corn field pixel, which was the most heterogeneous pixel (as shown by the error bars in the plot), shows the greatest difference between the albedo estimated from the RTLSR-HS model and the MODIS product. The RMSE obtained comparing AHS to MODIS albedo product was 0.04 for both models. Thirdly, taking advantage of the barley field, whose MODIS pixel was homogeneous, the in situ and the satellite albedo should be comparable. Therefore, while the MODIS albedo was (0.210 ± 0.003) the in situ albedo measurement was (0.204 ± 0.003) . This singular case shows that the MODIS product presents a good agreement with in situ data when considering a homogeneous pixel.

From this study we conclude that the RTLSR-HS model provides equivalent results to the RTLSR model outside the Hot Spot region thus they can be used indistinctly. Consequently, in the following section we compare the albedo derived from MODIS MCD43 data, which is estimated using the

RTLSR model with other methods that consider the RTLSR-HS model since it corrects the hot spot effect. Furthermore, from the MODIS product evaluation we have noted the difficulty of validating it over heterogeneous areas, which can lead to errors in the MODIS algorithm.

4.3. EVALUATION OF BRDF INVERSION METHODS

Finally, in the last section we evaluate four different BRDF inversion methods (that were briefly described in Chapter 1 and Chapter 2) through the broadband white sky albedo estimation. Following the first section results conclusions in order to obtain the BRDF with the VJB method and the proposed methods we worked with the M{O,Y}D09 surface reflectance data, which was estimated assuming the Lambertian approximation. Additionally, although the MCD43 product derives the BRDF with the RTLSR model, in case of the VJB and the proposed methods we considered the RTLSR-HS model, which lead to equivalent results as shown in the previous section results.

In order to compare the three methodologies, next, we analyze in detail a particular pixel centered in the AERONET site in Ispra, Italy (45.5°N, 8.5°E) which is a mixed forest/urban pixel. Figure 4.13 presents the temporal evolution of the broadband white sky albedo derived with the different methodologies.

The plot shows that the VJB method provides similar results to the proposed methods, for years 2002, 2003, 2005, 2006, 2008 and 2010. In 2004 VJB presents slightly lower values than the proposed methodologies, while for 2007 and 2009 it shows slightly higher albedo values. Comparing the three proposed methodologies, we did not observe significant differences between them during 2002, 2003, 2004, 2006 and 2009. The 5parameter Rsqr method showed similar results to the 4parameter method although it showed slightly lower values during 2005 and 2010 and higher values during 2007 and 2008 when compared to 5parameter Vsqr method. The MCD43 product temporal evolution seems to be noisier than the other

CHAPTER 4

Results

methodologies. The highest differences between the MODIS product and the other methods were detected during the end of spring and beginning of summer, when higher albedo values were measured. Furthermore, both the VJB as well as the proposed methods provided data continuously, while the MCD43 product, which was filtered following the quality flag labels, did not provided values during some periods of winter or spring. Comparing the number of data provided by the VJB and the proposed methods with the total data provided by the MCD43 product, the fraction of data provided by the MCD43 product was 70%. The total RMSE of each method against the MCD43 product in this site was 0.008 in case of the VJB method and 0.009 in case of the proposed methods which supposes a relative error of 5 – 6%.

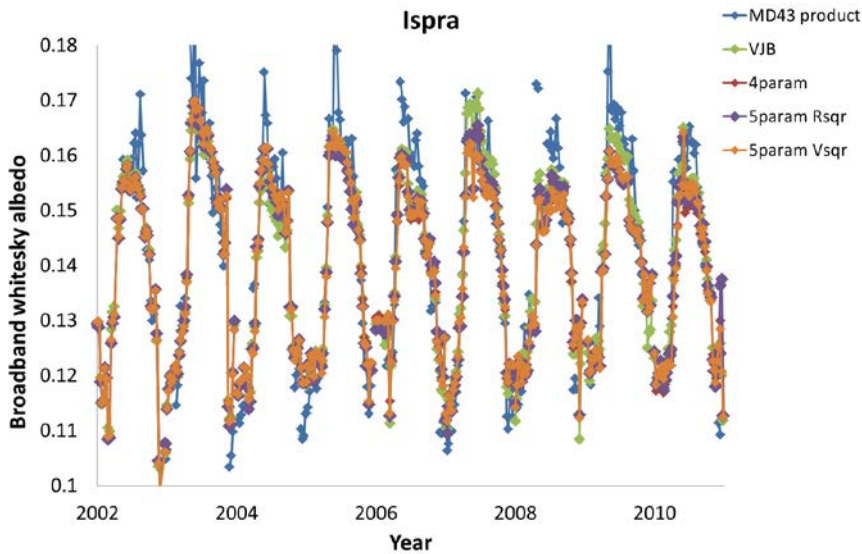


Figure 4.13. Temporal evolution of the broadband white sky albedo derived with the different methodologies at the Ispra site.

Figure 4.14 shows R and V plots of MODIS band 2 versus the five NDVI classes of the Ispra pixel considered in the VJB method in 2007. The graphs represent the VJB method as well as the three proposed methods fittings. Although the proposed methods consider every data to compute V

and R (not just five NDVI classes), Figure 4.14 provides V and R approached behavior as function of NDVI.

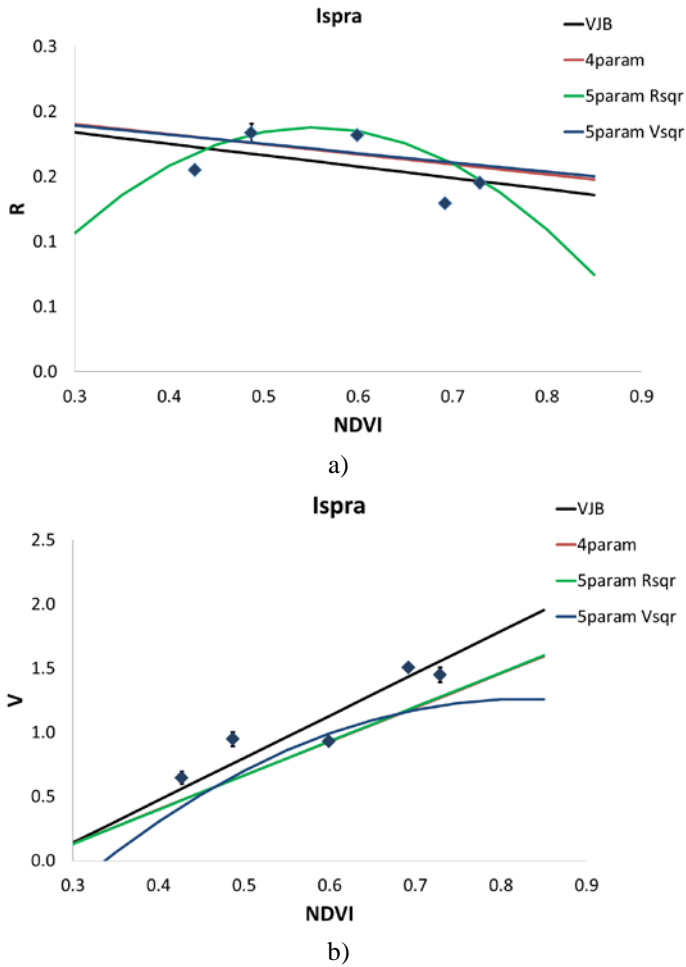


Figure 4.14. R and V parameters (band 2) versus the five NDVI classes of the Ispra pixel considered in the VJB method in 2007.

At first glance, V is more linear than R when represented versus NDVI so a second degree fitting is more convenient in case of the R

CHAPTER 4

Results

parameter. Therefore, the 5parameter Rsqr method fits well R data while it seems to slightly underestimate V data. On the contrary, 5parameter Vsqr method does not fit V data underestimating them and R fitting is similar to VJB method.

Figure 4.14 shows that the 4parameter linear fit provides slightly higher R values than the VJB method (in Figure 4.14a it is coincident to 5parameter Vsqr fitting) and lower V values than the VJB method (in Figure 4.14b it is coincident to 5parameter Rsqr fitting). In fact, although both methods assume V and R linear dependency with the NDVI, each one of them solves the problem differently. Since the volume kernel is always positive and the geometric kernel is always negative the 4parameter method provides lower albedo values than the VJB method in this particular case.

Next, Figure 4.15 shows the RMSE between considering the VJB method and the proposed methods versus the MCD43 product of an average year at the Ispra site. The RMSE of an average year is defined as the RMSE of each Day Of the Year (DOY) through every year studied (from 2002 until 2011), and quantifies the difference of the tested methods throughout the year.

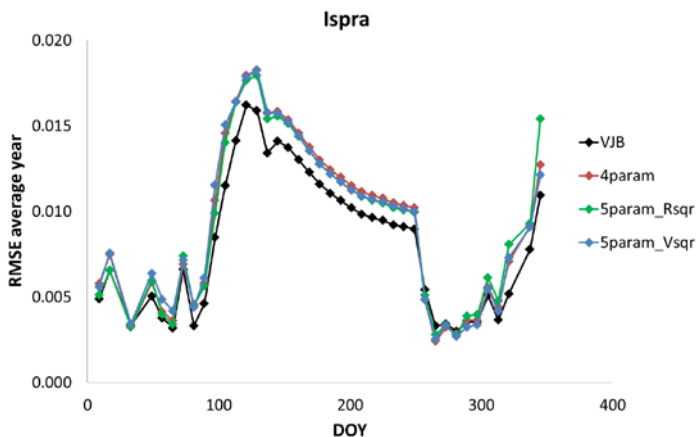


Figure 4.15. Average year RMSE at the Ispra site between the proposed methods and the VJB method regarding the MCD43 product.

The plot shows that the highest errors (from 0.013 to 0.017) were obtained from DOY 100 until 150 (from the 10th of April until the 30th of May), that is, during the spring season. Therefore, the error could be associated to the MCD43 product assumption of stable surface during 16 days which could lead to higher errors when the surface is changing. We also obtain high errors by the end of the year, which can be associated to the decrease of number of observations in the BRDF inversion algorithms. Nevertheless, the errors obtained during these periods suppose a maximum of 8% while during the rest of the average year this error stays below 5%. The VJB method provides slightly lower RMSE values than the proposed methods. The highest difference between them (0.001 approximately) was observed from DOY 100 to 250 (spring and summer seasons).

In order to see the spatial variability of the methods when compared to the MODIS product, Figure 4.16 shows the relative RMS for each method along the Europe scene on a particular 16-day period that corresponds to the 28th of July until the 13th of August of 2003.

Figure 4.16a shows the percentage of the difference between the broadband white sky albedo derived with the VJB method and the MCD43 product. Similarly, Figure 4.16b (4.16c and 4.16d) shows the percentage of the difference between the broadband white sky albedo derived with the 4parameter method (5parameter Rsqr and 5parameter Vsqr method respectively) and the MCD43 product. In this particular case, the proposed method presents lower errors (in absolute magnitude) than the VJB method. Comparing Figure 4.16a and 4.16b, the VJB method presents higher positive differences with the MCD43 product than the other methods particularly in the northern latitudes along the cloud mask neighboring pixels, along the east of Spain and north of Egypt. Adversely, the 4parameter method shows slightly higher positive differences with the MCD43 product than the VJB method in the west of Algeria (that does not correct the 5parameter Rsqr but the 5parameter Vsqr does) and lower negative differences along the center of Spain (where 5parameter Vsqr provides similar values and 5parameter Rsqr better results), France, the Adriatic east coast, Italy and Turkey. The center of Spain, France, the Adriatic coast and Turkey present better results with 5parameter Rsqr and 5parameter Vsqr

CHAPTER 4

Results

than 4parameter.

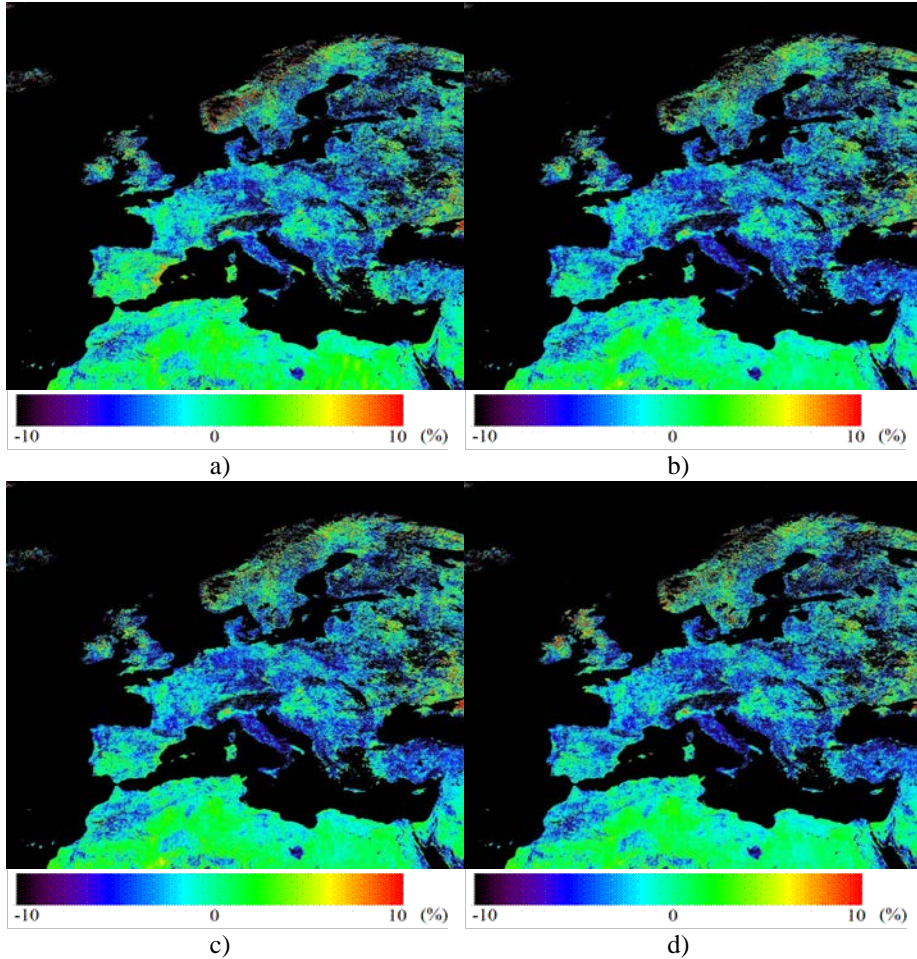


Figure 4.16. Percentage of the difference of the broadband white sky albedo of a Europe scene corresponding to the period from the 28th of July until the 13th of August of 2003 derived from a) the VJB method versus the MCD43 product and b) the method presented in this thesis versus the MCD43 product.

To better analyze Figure 4.16 images, Figure 4.17 represents the VJB method as well as the proposed methods images versus the MCD43 product.

The plots show that every method can be fitted to a regression line presenting near to one slope and high correlation coefficients which confirms a good agreement with the MCD43 product. Every method shows a RMSE of 0.010. The VJB method data shows slightly higher dispersion than the proposed methods, showing a standard deviation of 0.010 which is the main factor while it was equal to 0.009 in case of the other methods. However, the VJB method presents the lowest bias. We get similar correlation coefficient for all methods, although 4parameter method presents the highest and VJB method the lowest value.

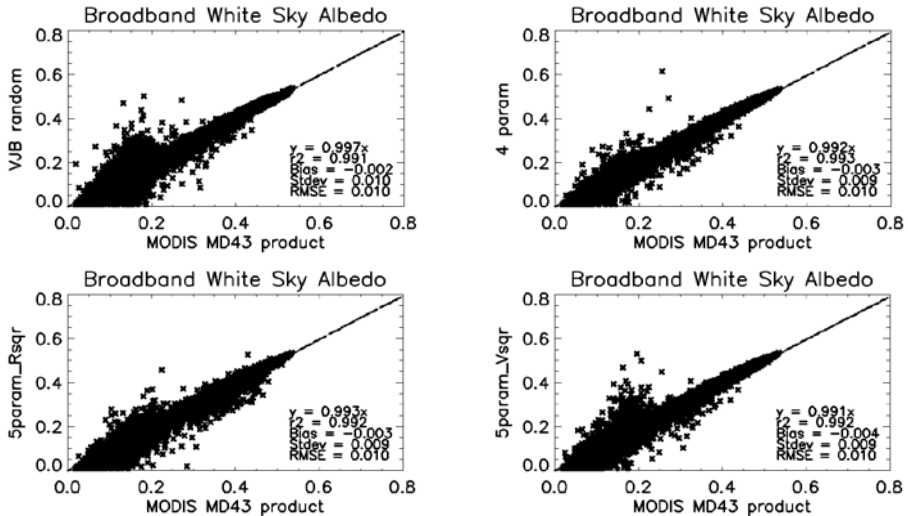


Figure 4.17. Broadband white sky albedo images of the Europe scene corresponding to the period from the 28th of July until the 13th of August of 2003 derived from the VJB, 4parameter, 5parameter Rsq and 5parameter Vsqr methods versus the MCD43 product.

Then, we consider all the data to analyze the error through the time series. Figure 4.18 shows the percentage of the total RMSE of the VJB method (Figure 5a) and the proposed methods (Figure 5b, 5c and 5d) against the MCD43 product.

CHAPTER 4

Results

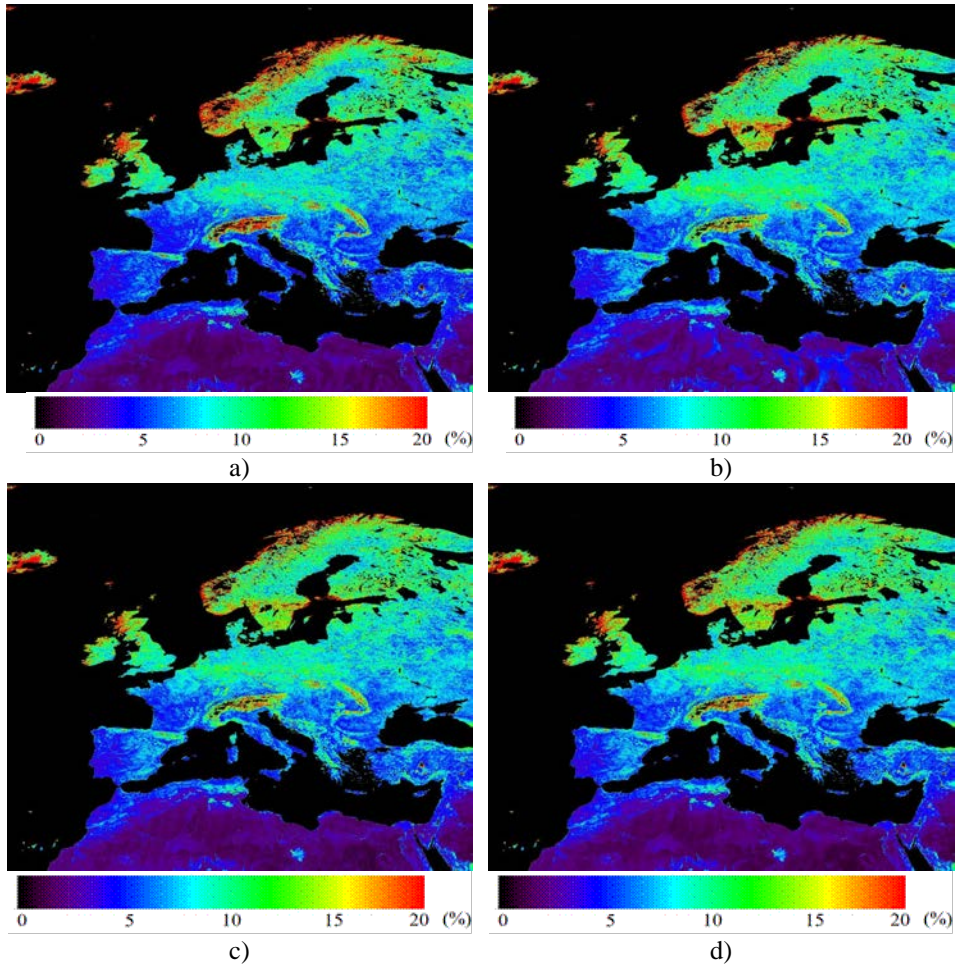


Figure 4.18. Percentage RMSE of a) the VJB method, b) the 4parameter method, c) the 5parameter Rsqr method and d) the 5parameter Vsqr method against the MCD43 product.

The images display that southern latitudes present lower errors while they increase for northern latitudes. Also we obtain higher errors for mountainous areas. Comparing VJB and 4parameter methods, generally the VJB presents higher errors than the proposed along the mountainous areas as the Scandinavian mountains, the Alps or the Carpathians across Central and

Eastern Europe and also in Scotland. However, the 4parameter method provides higher errors along the north of Africa, east of Spain, Italy, Germany and south of Sweden. Regarding 5parameter Rqr and 5parameter Vsqr, we observe better results than 4parameter. The improvement is more noticeable in Germany, Sweden and Northern Africa. If we estimate the total RMSE of the Europe scene we obtain an error of 5.0% in case of the VJB method and 6.1%, 5.1% and 5.3% in case of the 4parameter, 5parameter Rsqr and 5parameter Vsqr methods respectively.

Figure 4.19 shows the histogram of Figure 4.18 images and it shows two peaks. The first one is the highest one for every method and corresponds to 1.5% RMSE in case of VJB (which present the highest number of pixels), 5parameter Rsqr and 5parameter Vsqr. However, 4parameter first peak is located around 2% RMSE and shows the lowest number of pixels. The second peak, that represents similar number of pixels in every method, is centered around 6% RMSE for VJB and around 7% for the other methods. From this plot the conclusion is that most pixels present RMSE around 2% although there are other significant number of pixels that present a RMSE around 6% or 7%. The best results were observed for the VJB method, although 5parameter Rsqr and 5parameter Vsqr showed similar profiles.

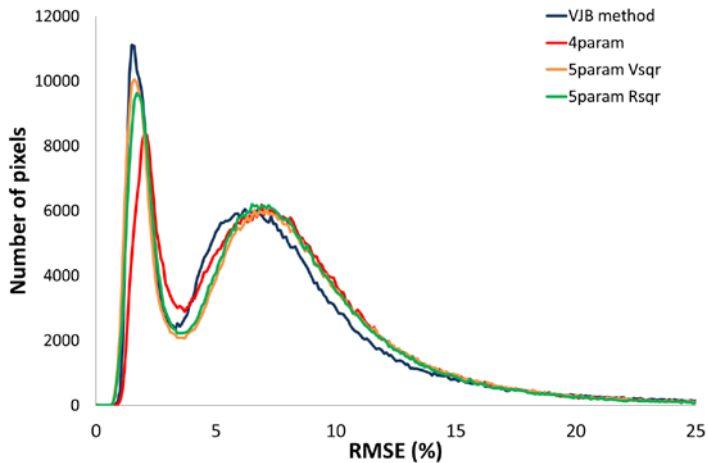


Figure 4.19. Histogram of Figure 4.18 images.

CHAPTER 4

Results

Finally, we analyzed the difference between each method dividing the study into different classes extracted from the MCD12C1 MODIS product. Figure 4.20 displays the spatial distribution of each class through the Europe scene.

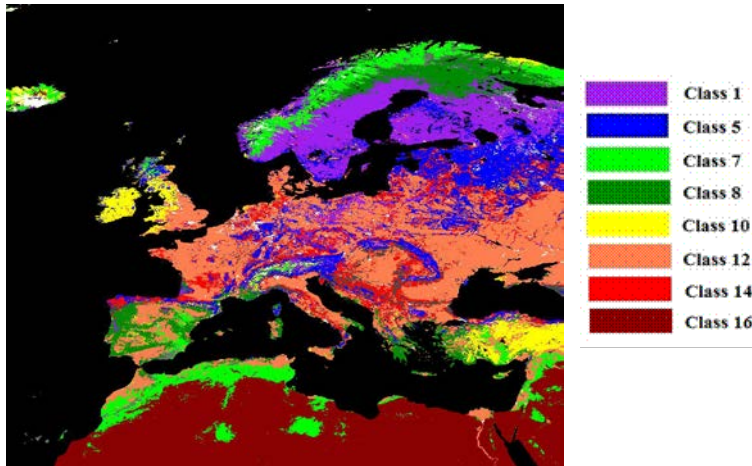


Figure 4.20. Land Cover Type Yearly Climate Modeling Grid (MCD12C1 MODIS product) and the classes considered in this study.

In this study we will consider only the most representative classes of the considered scene. Table 4.6 shows the land cover classification types.

Table 4.6. Land cover classification types considered in this study.

Class	Land cover type
1	Evergreen Needleleaf forest
5	Mixed forest
7	Open shrublands
8	Woody savannas
10	Grasslands
12	Croplands
14	Cropland/Natural vegetation mosaic
16	Barren or sparsely vegetated

Analogously to the Ispra analysis, Figure 4.21 shows the RMSE of the average year for each class for each method against the MCD43 product. The plots show that the highest errors were obtained for class 1 and 5 (the classes that represent forests) during the winter. Looking at Figure 4.20 those classes (mostly class 1) are located along the northern latitudes or along rugged mountainous areas that during the winter are covered by snow. Since the snow pixels were masked along both the MCD43 product as well as the MODIS reflectance data (from which we obtained the albedo with the other methods), during the winter the RMSE was estimated considering much less data than during the rest of the year. Additionally, these data could be contaminated by clouds or even snow which the cloud or snow masks did not consider. Previous studies that validated the surface albedo of the MCD43 product with in situ measurements also found larger differences in winter season (Jin et al., 2003; Cescatti et al., 2012). Jin et al. (2003) suggested that this was the result of the increased heterogeneity of surface reflectivity due to the presence of residual snow and canopy heterogeneity.

The highest errors were observed for Class 1 and 5 during the winter provided by the 4parameter method followed by the 5parameter Vsqr method while 5parameter Rsqr lead to similar RMSE as compared to the VJB method. From DOY 20 to 305, RMSE changed from 0.01 to 0.02, obtaining the poor results with the 5parameter Vsqr method during the spring and similar results with the other methods.

Regarding the other classes, the RMSE generally presented values between 0.01 and 0.02. These classes, that describe mainly stable surfaces along the year, correspond to most of the surface in the central and southern latitudes. The lowest errors were obtained for class 16 (barren or sparsely vegetated), where the errors decreased below 0.01.

CHAPTER 4

Results

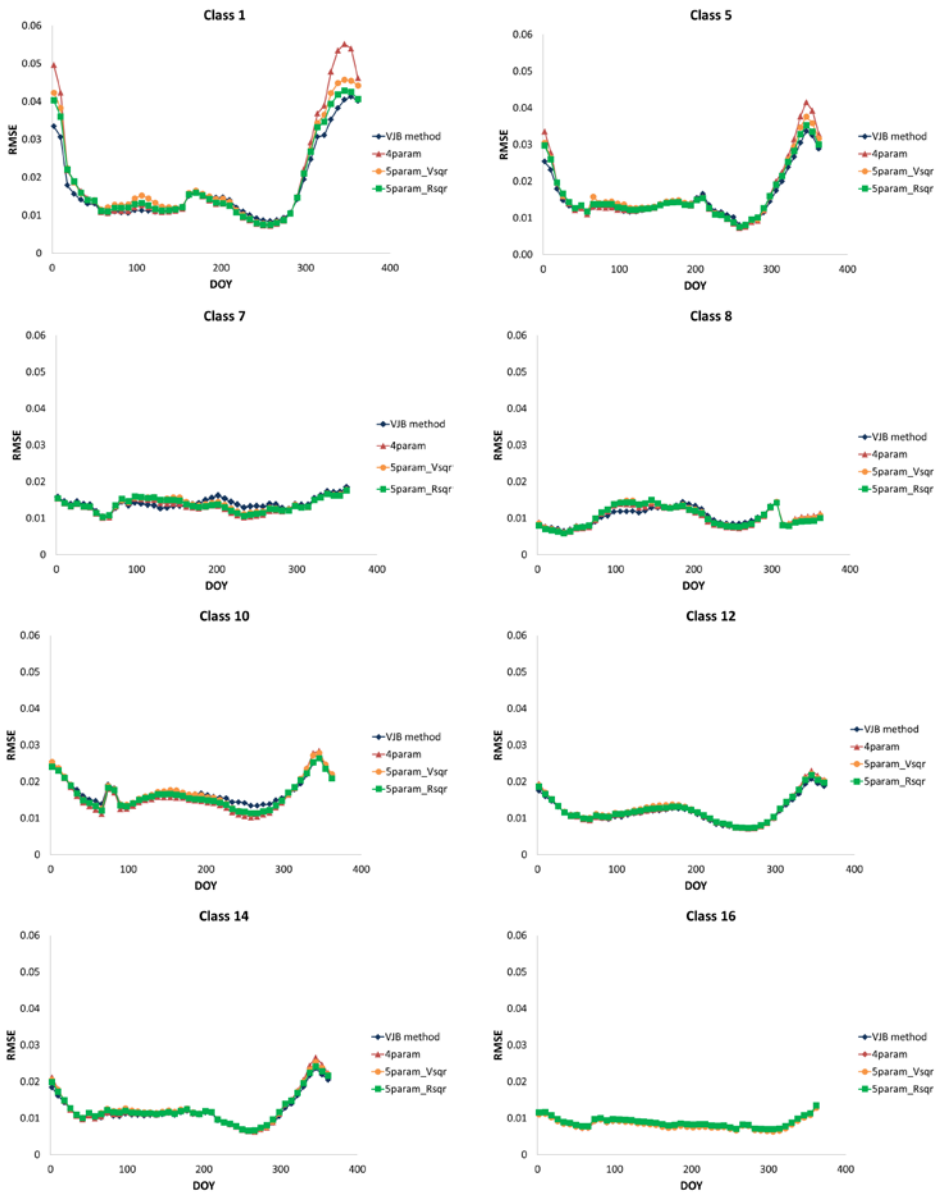


Figure 4.21. Average year RMSE for each class of the Europe scene between the proposed methods and the VJB method regarding the MCD43 product.

Comparing the VJB method with the other methods, they provided similar results to the VJB method. The highest differences between the proposed methods and VJB (leaving class 1 and 5 aside) were detected for classes 7 (open shrublands), 8 (woody savannas) and 10 (grasslands). In case of classes 7 and 8, VJB led to slightly lower RMSE than the other methods from DOY 100 to 150 (spring). However, for classes 7 and 10, the other methods provided slightly better results from DOY 200 to 300 (end of summer and fall). Locating these classes in Figure 4.20, class 7 is present in Norway, east of Spain and the Mediterranean coast of Africa, class 8, is located in the east of Norway and center of Spain and class 10 is found in the east of the United Kingdom, Ireland and Turkey. Most of these regions' different errors among methods were detected in Figure 4.18. Finally, in this analysis we did not see significant differences between the proposed methods (from class 7 to 16) showing similar RMSE. This must be a consequence of including several pixels (not just every pixel of the same class, but also the temporal evolution of each pixel for the same DOY through the years) into the RMSE estimation.

As a general overview, this study, that inter compare different inversion methods, shows that both the VJB method and the proposed methods provide equivalent results to the MCD43 MODIS product but with the advantage of a daily versus a 16-day basis temporal resolution. From the analysis presented, the best method that provides similar results to the VJB method is the 5parameter Rsqr method. Thus, we present an alternative method to the VJB that is more robust since it does not depend on the NDVI classification into five classes and improve its time processing.

CHAPTER 4
Results

CHAPTER 5

APPLICATION: ALBEDO ACCURACY IMPACT ON EVAPOTRANSPIRATION PRECISION

During the last decades several land surface energy models have developed accurate albedo estimations for achieving reliable daily evapotranspiration (ET) retrievals. Despite these improvements in the surface energy models, we detected a systematical erroneous approach that most studies assume. It consists of considering that the surface broadband albedo can be estimated directly as a weighted average of surface reflectance. However, this approach does not take into account the surface

CHAPTER 5

Application: Albedo accuracy impact on evapotranspiration precision

anisotropy, which is described by the BRDF. As we have explained in previous chapters, the surface albedo is related to land surface reflectance by directional integration and is therefore dependent on the BRDF. In this chapter, we analyze the influence of estimating the land surface albedo directly from the surface reflectance or through the BRDF integration in the estimation of energy balance components such as the net radiation, latent and sensible heat flux and, consequently, in the land surface ET. To this end, we processed remote sensing and in-situ meteorological data measured at the agricultural test site of Barrax in the framework of the EODIX field campaign.

5.1. INTRODUCTION

Detailed knowledge of land surface fluxes, especially latent and sensible components, is important for monitoring the climate of land surface, for evaluating parameterization schemes in weather and climate models used to predict flux exchanges between the surface and the lower atmosphere, and for agricultural applications such as irrigation scheduling (Courault, 2005). Evapotranspiration accounts for the flux of water evaporated at the Earth-atmosphere interface (from soil, water bodies and interception) and transpired by vegetation through stomata in its leaves as a consequence of photosynthetic processes. ET is an important component of the water cycle and is associated with latent heat flux (LE), a key link between the energy and water cycles. In other words, LE represents the energy needed for the ET process. Land ET is a central process in the climate system and a nexus of the water, energy and carbon cycles (Jung et al., 2010). Global land ET returns about 60% of annual land precipitation to the atmosphere (Oki and Kanae, 2006). Terrestrial ET can affect precipitation (Koster et al., 2004), and the associated LE helps to control surface temperatures, with important implications for regional climate characteristics such as the intensity and duration of heat waves (Seneviratne et al., 2006; Vautard et al., 2007). Therefore, in this context, accurate determination of ET is essential to estimate water balances.

The ET process is determined by the amount of energy available to vaporize water. Solar radiation is the largest energy source and is able to change large quantities of liquid water into water vapor. Net radiation (R_n) is the difference between incoming and outgoing radiation of both short and long wavelengths. It is the balance between the energy absorbed, reflected and emitted by the earth's surface or the difference between the incoming net shortwave and the net outgoing longwave radiation. The surface albedo plays an important role in deriving this parameter since it describes the ratio between the up-welling and down-welling incident shortwave irradiance upon a surface. Consequently, in surface balance applications, the surface albedo accuracy must affect directly the precision of the R_n and thus, indirectly the daily ET. Nevertheless, the impact of the albedo accuracy on surface energy balance parameters has not been investigated yet, to our knowledge. Basically, in case of ET models (Menenti and Choudhury, 1993; Bastiaanssen et al., 1998; Roerink et al., 2000; Su, 2002; Allen et al., 2007; Corbari et al., 2011), when there are no in-situ data available, the surface albedo can be estimated from different ways. Some studies replace the net radiative components, estimating proxy values following the land cover types. Most studies, however, assume the surface as Lambertian considering the equivalence of the albedo with the surface reflectance (French et al., 2005; Verstraeten et al., 2005; McCabe and Wood, 2006; Sobrino et al., 2007a; Timmermans et al., 2007; Tittebrand and Berger, 2008; Galleguillos et al., 2011; Vinukollu et al., 2011). All these works showed significant and relevant statistical results about the performance of the ET model without presenting any error sensibility of the albedo accuracy influence on the results.

The main objective of this work is to evaluate the impact of considering the surface broad-band albedo derived both from the integration of the BRDF and also from the weighted average of the surface reflectance on the R_n and on the daily ET estimation. In order to estimate the ET we used the Simplified Surface Energy Balance Index (S-SEBI) method developed by Roerink et al (2000). We chose this model since albedo accuracy may affect not just the R_n but also the sensible heat flux (H) and the LE estimation through the evaporative fraction (EF). This study was developed in the framework of the EODIX field campaign in Barrax taking

CHAPTER 5

Application: Albedo accuracy impact on evapotranspiration precision

advantage of the albedo images evaluated in Chapter 4.2. Additional information about the test site and the EODIX campaign is described in chapter 3.1. Next, we describe in situ and airborne data considered in this particular study.

5.2. DATA ACQUISITION

5.2.1. In-situ data

5.2.1.1. Continuous measurements

During the EODIX field campaign, two fixed meteorological and flux stations complemented with radiometric measurements were located in two different crops: a wheat and a barley field.

In case of the wheat field, we installed a meteorological station that measured R_n , air temperature, relative humidity and ground flux using a time step of 10 min.

Over the barley crop, the Politecnico di Milano group installed an eddy covariance tower. H and LE were measured by a tridimensional sonic anemometer (Young 81000) and open path gas analyzer (LICOR 7500) located at the top of a tower of 5 m high. Data were collected at high frequency (20Hz) and then averaged each minute. Energy fluxes were initially corrected applying instrumental and physical corrections (Corbari et al., 2012). In particular the Webb correction for density fluctuations (Webb et al. 1980) and the correction for buoyancy flux due to sonic temperature measurements (Liu et al. 2001) were considered. Moreover, tilt correction was implemented (Tanner and Thurtell 1969). Frequency response corrections (Massman 2000) and despiking procedure were also applied.

R_n , relative air humidity and air temperature were measured at 1 minute time step.

.2.1.1. Instantaneous measurements

Besides, calibration and validation activities were carried out simultaneously to the airborne overpass. Biogeophysical parameters such as land surface emissivity and temperature, in addition to visible and near-infrared surface reflectance were retrieved by transects over different surface types of the test area in order to obtain sufficient representative spectra. Thermal measurements (emissivity and land surface temperature, LST) were carried out using a CIMEL CE312-2 radiometer. The CIMEL CE312-2 is a radiance-based thermal-infrared radiometer composed of an optical head and a data storage unit. Its detector includes 6 bands, a broadband, 8-13 μm , and five narrower filters, at 8.1 – 8.5 μm , 8.5 – 8.9 μm , 8.9 – 9.3 μm , 10.3 – 11 μm and 11 – 11.7 μm . The emissivity characterization of different surfaces was carried out by means of the TES (Temperature and Emissivity Separation) algorithm (Gillespie et al., 1998) applied to ground-based measurements (Payan and Royer, 2004; Jiménez-Muñoz and Sobrino, 2006; Sobrino et al., 2009; 2011).

Regarding the VNIR measurements, on the one hand, transects were carried out using an ASD Field Spec 3 spectroradiometer and, on the other hand, we disposed of a GER-1500 spectroradiometer mounted in a goniometer system. These last measurements were carried out in a corn field in order to validate both the surface reflectance and the albedo derived from AHS imagery. More details of these measurements can be found in Chapter 3.1.2.

5.2.2. Airborne data

The airborne data studied in this work were acquired by the AHS instrument. Information about the sensor and flights geometry of acquisition was already discussed in Chapter 3.1.3. Table 5.1 summarizes all the data used in this chapter.

CHAPTER 5

Application: Albedo accuracy impact on evapotranspiration precision

Table 5.1. Data set used in this work retrieved during the EODIX field campaign

Type	Coordinates	Land Cover	Measurement
Meteorological and flux tower	39° 3' 46.4" N 2° 5' 33.8" W	Wheat	Rn, air temperature, relative humidity, soil moisture, ground flux
Meteorological and flux tower	39° 03' 17.3" N 2° 05' 38.9" W	Barley	Rn, air temperature, relative humidity, soil moisture, ground flux, H and LE
Land Leaving Radiance (transects)	Different locations	Bare soil, alfalfa, corn, barley, wheat and green grass	GER 1500, ASD and CIMEL CE 312-2
Airborne	39° 4' 1.6" N 2° 5' 30.3" W	All study area	AHS sensor (80 bands from 0.3 to 14.8 um)

5.3. METHODS

5.3.1. Atmospheric correction

A total of seven flight overpasses were achieved during the EODIX field campaign. These images were retrieved along different wavelengths from the visible to the thermal infrared. Thus, two different corrections were carried out in order to obtain the surface reflectance and albedo from the VNIR atmospheric correction, and LST and emissivity from the thermal atmospheric correction. During this campaign there was a high angular variability of airborne images not only due to the high AHS FOV but also because of the different flight geometries. The increasing of both the view and illumination zenith angle causes the decrease of atmospheric transmittance. Therefore, we considered very carefully each pixel's geometry of acquisition in the atmospheric correction of both the VNIR and the thermal spectral ranges.

Airborne images from the VNIR spectral range, were atmospherically corrected with the radiative transfer code 6S. Additional information about this process can be found in Chapter 2.2.

Thermal atmospheric correction was carried out using the MODerate resolution atmospheric TRANsmiission (MODTRAN) radiative transfer code (Berk et al. 1999). This process has been achieved in previous works and past field campaign carried out in the Barrax test area. A complete description of this process is well detailed in Sobrino et al (2006).

5.3.2. Albedo Estimations

In this work we take advantage of albedo airborne images processed in the test of the MCD43 surface albedo estimation study developed in Chapter 4.2. Following that study conclusions, we have considered RTLSR-HS albedo images. All the information about the method can be checked in Chapter 2.2.

5.3.3. Land Surface Temperature and emissivity

The long-wave component of the R_n and also most of the ET algorithm requires the LST and emissivity estimation. Thus, we used the Temperature and Emissivity Separation (TES) method proposed by Gillespie et al (1998). This method was initially developed for the Advanced Spaceborne Thermal Emission and Reflection Radiometer (ASTER), although it has led to satisfactory results in previous field campaigns using AHS images (Sobrino et al., 2007b).

Besides, the spectral emissivity (for each 10 thermal bands) was converted from narrow to broad-band by averaging every band's results for each pixel. A minimum error (less than ~1% relative error) is expected using this average.

Finally, we evaluated airborne results with in-situ LST and emissivity measurements.

CHAPTER 5

Application: Albedo accuracy impact on evapotranspiration precision

5.3.4. Net radiation estimations

The R_n was estimated using the relationship proposed by Bastiaanssen et al. (1998):

$$R_n = (1 - \alpha)R_{s\downarrow} + R_{L\downarrow} - R_{s\uparrow} - (1 - \varepsilon)R_{L\uparrow} \quad (5.1)$$

where $R_{s\downarrow}$ ($W\ m^{-2}$) is the at surface incoming direct and diffuse shortwave radiation, α is the surface broad-band albedo, $R_{L\downarrow}$ ($W\ m^{-2}$) is the incoming longwave radiation, $R_{s\uparrow}$ ($W\ m^{-2}$) is the outgoing shortwave radiation reflected by the surface, $R_{L\uparrow}$ ($W\ m^{-2}$) is the outgoing longwave radiation emitted from the surface and ε is the surface emissivity.

Two images of R_n were calculated by considering first the broad-band albedo derived from the BRDF and secondly the surface reflectance weighted average following Liang (2000) equation (Eq 1.36). $R_{s\downarrow}$ and $R_{L\downarrow}$ were estimated by averaging R_n in-situ measurements from both meteorological towers and were assumed constant for the whole study area. Besides, $R_{L\uparrow}$ was estimated using:

$$R_{L\uparrow} = \varepsilon\sigma T_s^4 \quad (5.2)$$

where T_s is the LST derived from AHS images and σ is the Stefan–Boltzmann constant.

5.3.5 Daily Evapotranspiration

Land surface ET is mostly influenced by R_n , which (following the energy balance equation) is equal to

$$R_n = H + LE + G \quad (5.3)$$

where G is the ground. Thus, the variations of the R_n (influenced by the albedo variability) should affect the estimation of surface fluxes and, therefore, the ET. Since G , H and LE are required to estimate the

instantaneous ET, these variables were computed using the following equations.

First, G flux can be derived from different assumptions. One approach is to consider G as a proportion of Rn estimated according to the surface features related to vegetation information (Bastiaanssen et al., 2000). Other methods include a thermal parameter such as the LST (Su, 2002). In this work, G flux was estimated using the equation proposed by Clothier et al. (1986) which is based on the first approach mentioned.

$$G = Rn \left(0.295 - 0.01331 \frac{\rho_{NIR}}{\rho_{IR}} \right) \quad (5.4)$$

where ρ_{NIR} and ρ_{IR} are the surface reflectance in the red and the near infrared channels respectively. It is important to denote that a proportion of the surface anisotropy effects may also be included in the surface reflectance ratio.

Secondly, in order to estimate H and LE, we used the Simplified Surface Energy Balance Index (S-SEBI) method developed by Roerink et al (2000). This method is based on the EF estimation using a scatterplot between the surface temperature and the surface albedo. In the plot, one can estimate a base line representative of the maximum sensible heat ($\lambda E = 0$) and the maximum potential ET ($\lambda E = \text{Max}$). When determining EF, an approximation (according to Roerink et al., 2000; Su & Menenti, 1999; Su et al., 1999; Verstraeten et al., 2005) is attempted:

$$EF = \frac{T_H - T_s}{T_H - T_{LE}} = \frac{a_H \alpha + b_H - T_s}{(a_H - a_{LE}) \alpha + b_H - b_{LE}} \quad (5.5)$$

where T_H is the LST for dry pixels; T_{LE} is the LST for wet pixels; α is surface albedo; a_H , a_{LE} are the slopes of the line of the higher and lower temperatures respectively as a function of surface albedo and b_H , b_{LE} are the intercepts of the linear fit of the higher and lower temperatures respectively as a function of surface albedo.

CHAPTER 5

Application: Albedo accuracy impact on evapotranspiration precision

In this paper, two albedo/temperature diagrams as well as two EF were estimated considering the albedo derived from the BRDF integration (hereafter referred to as α_{BRDF}) and also the albedo derived from the surface reflectance weighted average (α_{REF}). Initially, this method was developed for Landsat imagery where the surface broad-band albedo was estimated using the surface reflectance weighted average (Roerink et al., 2000). Therefore, we expect differences in the albedo/Temperature diagram when using α_{BRDF} , and consequently in the EF.

Thirdly, H and LE were derived from the following equations:

$$LE = EF(Rn - G) \quad (5.6)$$

$$H = (1 - EF)(Rn - G) \quad (5.7)$$

Finally, the instantaneous and the daily ET (ET_i and ET_d respectively) were estimated using the following equations.

$$ET_i = \frac{24 \cdot 3600 \cdot EF \cdot R_{ni}}{\lambda} \quad (5.8)$$

$$ET_d = \frac{24 \cdot 3600 \cdot EF \cdot R_{nd}}{\lambda} = \frac{24 \cdot 3600 \cdot EF \cdot C_{di} \cdot R_{ni}}{\lambda} \quad (5.9)$$

where R_{ni} is the instantaneous Rn for each image, R_{nd} is the daily Rn, λ is the latent heat of vaporization equal to 2,45 MJ/kg and C_{di} is the ratio between R_{nd} and R_{ni} proposed by Seguin and Itier, (1983).

C_{di} was estimated from in situ data measured in the meteorological station placed in the wheat field. Table 5.2 shows the R_{ni} values measured and the corresponding C_{di} value considering R_{nd} equal to 222.1 $\text{W}\cdot\text{m}^{-2}$.

Table 5.2. R_{ni} and C_{di} values obtained from the meteorological station in the wheat field.

Time (UTC)	R _{ni} (W.m ⁻²)	C _{di}
9:04	484.5	0.458
9:11	509.6	0.436
9:21	529.7	0.419
9:39	548.7	0.405
9:46	566.9	0.392
9:54	582.3	0.381
10:01	597.7	0.372

5.4. RESULTS

5.4.1. Albedo comparison

Surface reflectance images resulting from the atmospheric correction scheme were tested with in situ measurements retrieved by an ASD and a GER 1500 spectroradiometer providing a RMSE lower than 0.03 for every band. Additional information about the validation process can be found in Chapter 4.2.1.

The angular variation of each flight line during the EODIX 2011 field campaign was designed in order to study the angular variability of the surface reflectance and thermal parameters and also to estimate the BRDF. In this context, Figure 5.1 shows the angular variability of α_{BRDF} and α_{REF} AHS images acquired between 9 and 10 UTC. The first three images (9:04, 9:11 and 9:21) were acquired along the solar plane while the others were acquired along the orthogonal plane. In this work we have followed the Roujean et al. (1992) notation where negative view zenith angles (VZA) are located in the backward scattering direction and positive values are located in the forward scattering direction.

CHAPTER 5

Application: Albedo accuracy impact on evapotranspiration precision

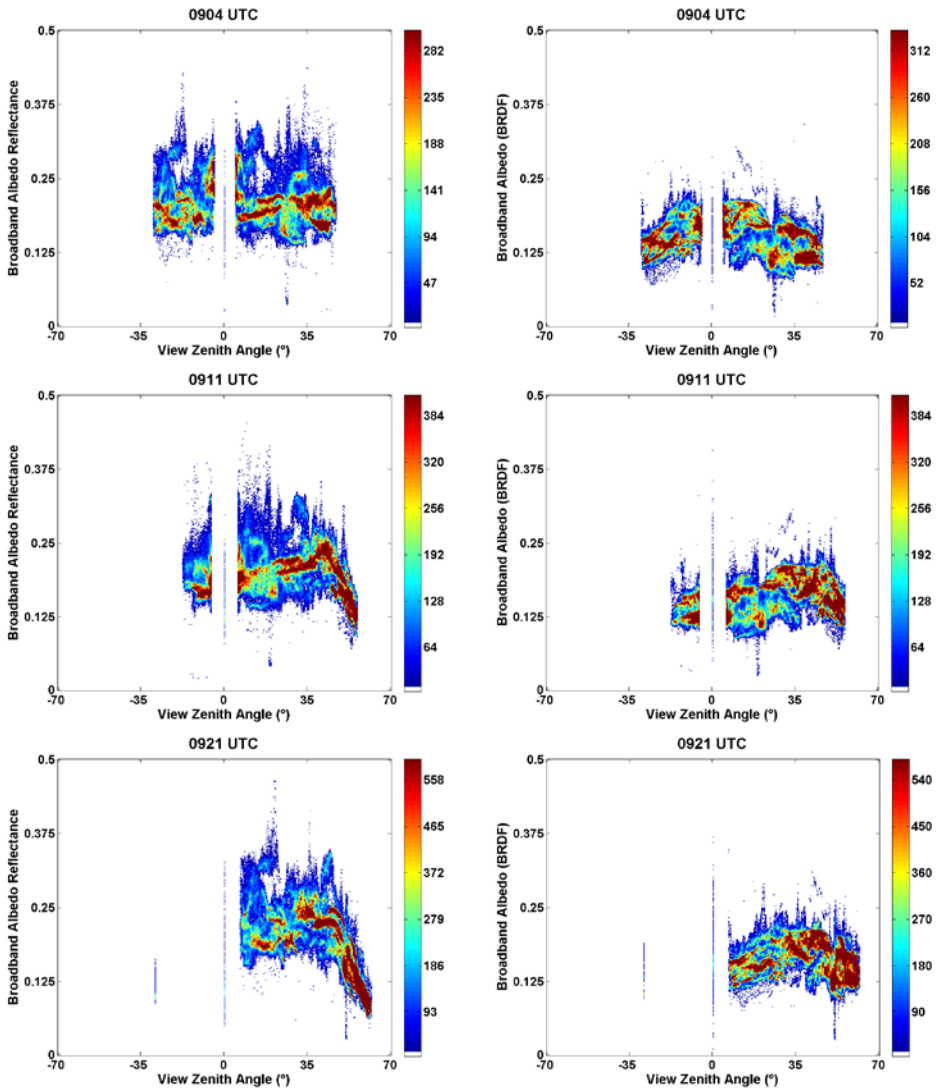


Figure 5.1. α_{REF} (left column) and α_{BRDF} (right column) along the main area during each flight overpass versus the VZA.

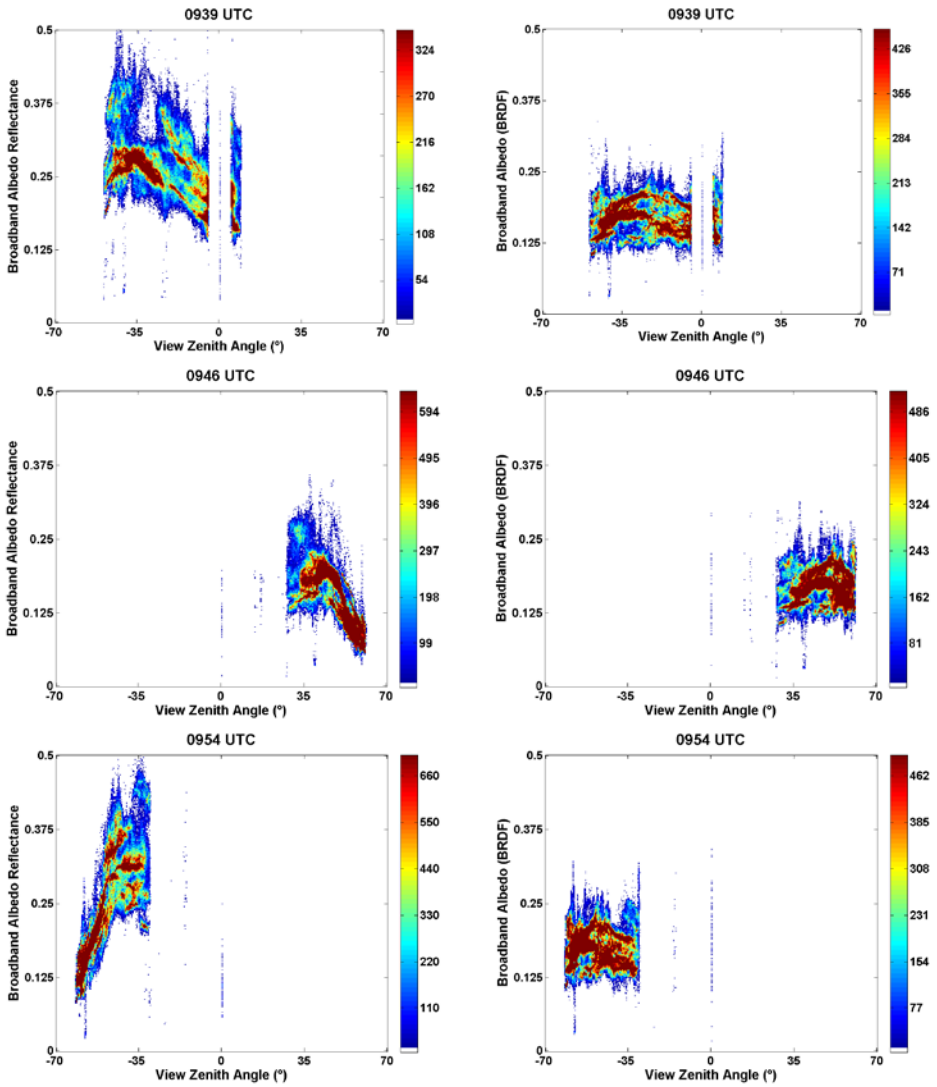


Figure 5.1. α_{REF} (left column) and α_{BRDF} (right column) along the main area during each flight overpass versus the VZA (continued).

CHAPTER 5

Application: Albedo accuracy impact on evapotranspiration precision

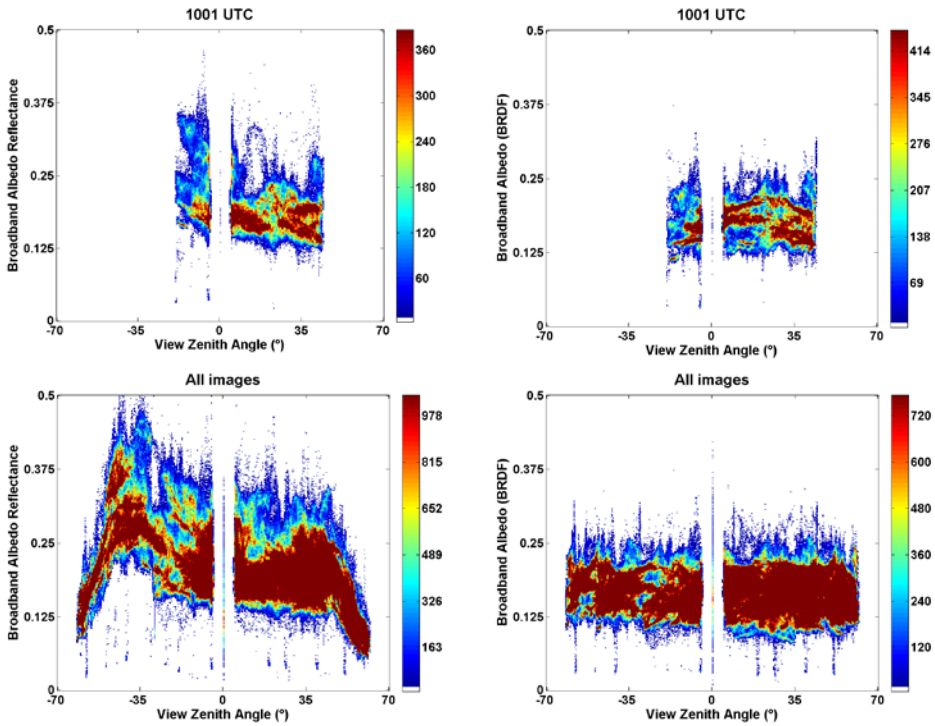


Figure 5.1. α_{REF} (left column) and α_{BRDF} (right column) along the main area during each flight overpass versus the VZA (continued).

At first glance, the VZA shows strong influences on α_{REF} while it does not present any influence on α_{BRDF} . Considering first the solar plane direction, α_{REF} decreases with the increasing of VZA. Regarding the orthogonal plane, the angular effect presents the highest influence on α_{REF} at 9:54, showing similar (or slightly lower) albedo values than α_{BRDF} for high VZA (in absolute magnitude) that increases with a pronounced slope reaching the maximum values around 35°, which coincides with the solar zenith angle at that time. The reason for this behavior is due to the hot spot effect which consists of a peak of reflectance obtained when Sun and view directions coincide in the backward scattering (Breon et al., 2002). The hot spot effect is also noticeable at 9:39 where the VZA at the center of the image was -40°. However, in this case, the surface reflectance decreases as

the VZA approaches to nadir. In case of 9:46 (+40°) image every VZA belongs to the forward scattering direction, consequently, we do not observe any hot spot effect showing a continuous decrease in the surface reflectance as the VZA increases. However, at 10:01 UTC, the VZA was close to the Nadir and α_{REF} presents the minimum dependency with the VZA. Including all images (last figure), the plot shows an important influence of the VZA when it gets higher values than 35° in case of α_{REF} evidencing a clear overestimation (or underestimation) of this parameter compared with the albedo derived from BRDF integration.

As an example, Figure 5.2 shows the linear comparison between α_{BRDF} and α_{REF} , in addition to the spatial variability of 9:39 and 10:01 images.

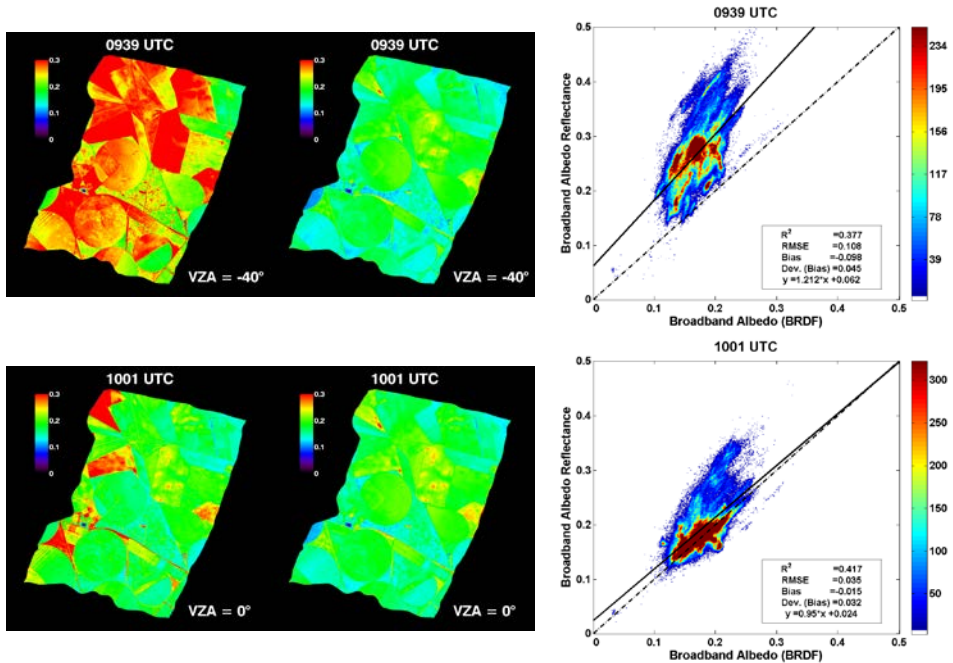


Figure 5.2. α_{REF} (left) and α_{BRDF} (center) AHS images of the main area and α_{REF} vs. α_{BRDF} scatterplot (right) for 9:39 and 10:01 images.

As commented in Figure 5.1 the highest error is evidenced for the 9:39 UTC image, which presents a RMSE of 0.11 and a clear overestimation

CHAPTER 5

Application: Albedo accuracy impact on evapotranspiration precision

of the albedo. The minimum error of 0.04 is obtained for the 10:01 UTC image which central VZA was near to nadir. However, the albedo is slightly overestimated mainly in the borders where the VZA presented higher values due to the high FOV of AHS.

The statistics for every image are detailed in Table 5.3. Generally, the broad-band albedo presents higher values when using directly the reflectance weighted average than the same magnitude estimated from the BRDF integration which leads to negative bias. Centering the attention in the mean values, α_{BRDF} presents lower values than α_{REF} and similar values when comparing each image. With reference to the bias, we get negative values in almost every case (albedo overestimation when considering α_{REF}) excepting 9:46 image (+40°) which coincides with the highest VZA in the forward scattering direction. This may be a consequence of the shadowing effect which reduces the surface reflectance values in this direction.

Table 5.3. Statistics for α_{BRDF} and α_{REF} for each AHS image.

UTC hour	VZA (°)	α_{BRDF}	α_{REF}	$\alpha_{\text{BRDF}} - \alpha_{\text{REF}}$		
		Mean	Mean	Bias	Stddev	RMSE
9:04	40	0.15	0.21	-0.06	0.03	0.07
9:11	0	0.16	0.20	-0.04	0.03	0.05
9:21	57	0.16	0.19	-0.03	0.05	0.05
9:39	-40	0.17	0.27	-0.10	0.05	0.11
9:46	40	0.17	0.15	0.03	0.05	0.05
9:54	-57	0.17	0.24	-0.07	0.08	0.10
10:01	0	0.18	0.19	-0.015	0.03	0.04

Considering every image, bias is equal to -0.07 with a RMSE of 0.07. It supposes a Relative RMSE of about 39% representing a clear error source when the albedo is approximated to a weighted average of the surface reflectance. However, as analyzed in previous figures, the highest errors correspond to VZA higher than 35°. Therefore, the Lambertian assumption can be considered in case of sensors with reduced FOV and in case of near to nadir observations.

5.4.2. Net radiation

Figure 5.3 presents the Rn estimated from α_{BRDF} and from α_{REF} .

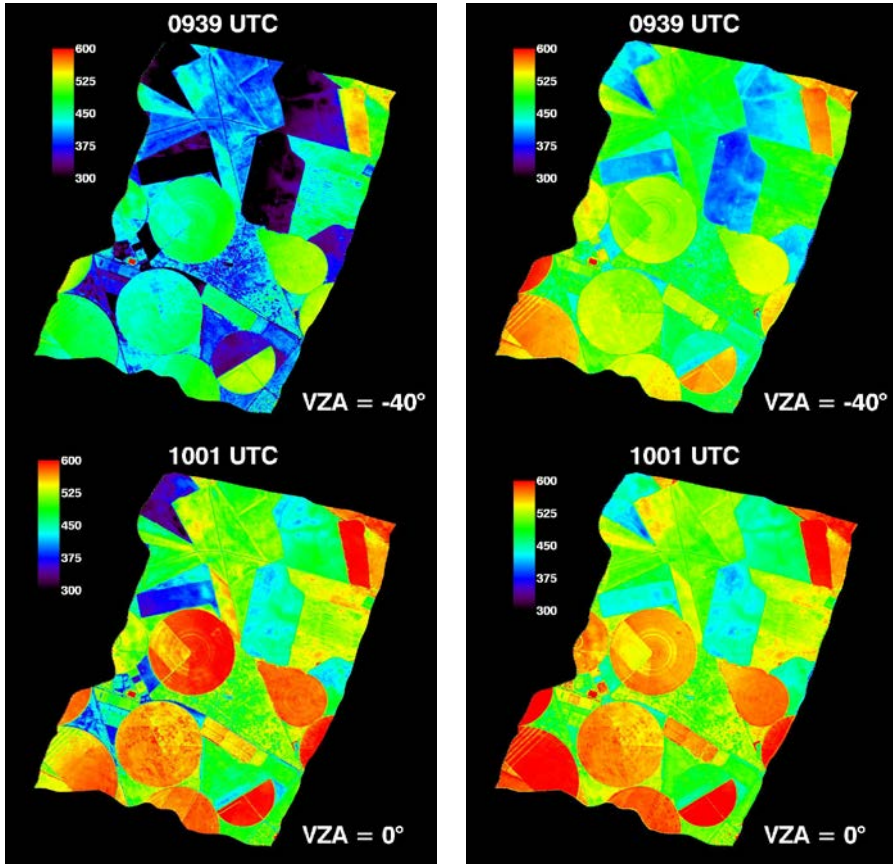


Figure 5.3. Rn images ($\text{W}\cdot\text{m}^{-2}$) at 9:39 (-40° VZA) and at 10:01 (0° VZA) from α_{REF} (left) and from α_{BRDF} (right).

Generally, the highest Rn (independently on the albedo considered) corresponds to water bodies. Besides, lowest values are characterized by bare soil with sparse vegetation cover. Comparing each albedo results, 9:39 image shows a clear underestimation of the Rn for high VZA when the α_{REF} is used. However, the difference between using α_{BRDF} and α_{REF} in the Rn

CHAPTER 5

Application: Albedo accuracy impact on evapotranspiration precision

magnitude is much less significant in case of near to nadir images. In this case, α_{REF} shows a slight overestimation in vegetated fields while presenting a clear underestimation in case of bare soils located in the left side of the image (backward scattering direction).

Table 5.4 shows the statistical results for each Rn image.

Table 5.4. Statistics of Rn for each AHS image.

UTC hour	VZA (°)	α_{BRDF}	α_{REF}	$\alpha_{BRDF} - \alpha_{REF}$		
		Mean ($W \cdot m^{-2}$)	Mean ($W \cdot m^{-2}$)	Bias ($W \cdot m^{-2}$)	Stddev ($W \cdot m^{-2}$)	RMSE ($W \cdot m^{-2}$)
9:04	40	460	418	43	24	49
9:11	0	487	457	30	24	39
9:21	57	505	485	21	35	41
9:39	-40	490	413	77	35	85
9:46	40	536	557	-20	37	42
9:54	-57	540	484	56	65	85
10:01	0	524	511	12	27	30
TOTAL				31	48	57

The mean value of Rn for each image derived using α_{BRDF} shows less standard deviation than α_{REF} results. Generally, using α_{REF} underestimates Rn showing positive bias in every flight excepting 9:46 image (+40°) which may be due to α_{REF} underestimation (shadowing effect). The highest bias and RMSE is obtained for the 9:39 and 9:54 images which includes the hot spot effect. The RMSE ranges from 30 to 85 $W \cdot m^{-2}$ which implies a relative error from 6 to 17%. Generally, considering the Lambertian assumption lead to an underestimation of 31 $W \cdot m^{-2}$ and a RMSE of 57 $W \cdot m^{-2}$.

5.4.3. Ground heat flux

Figure 5.4 displays G airborne images.

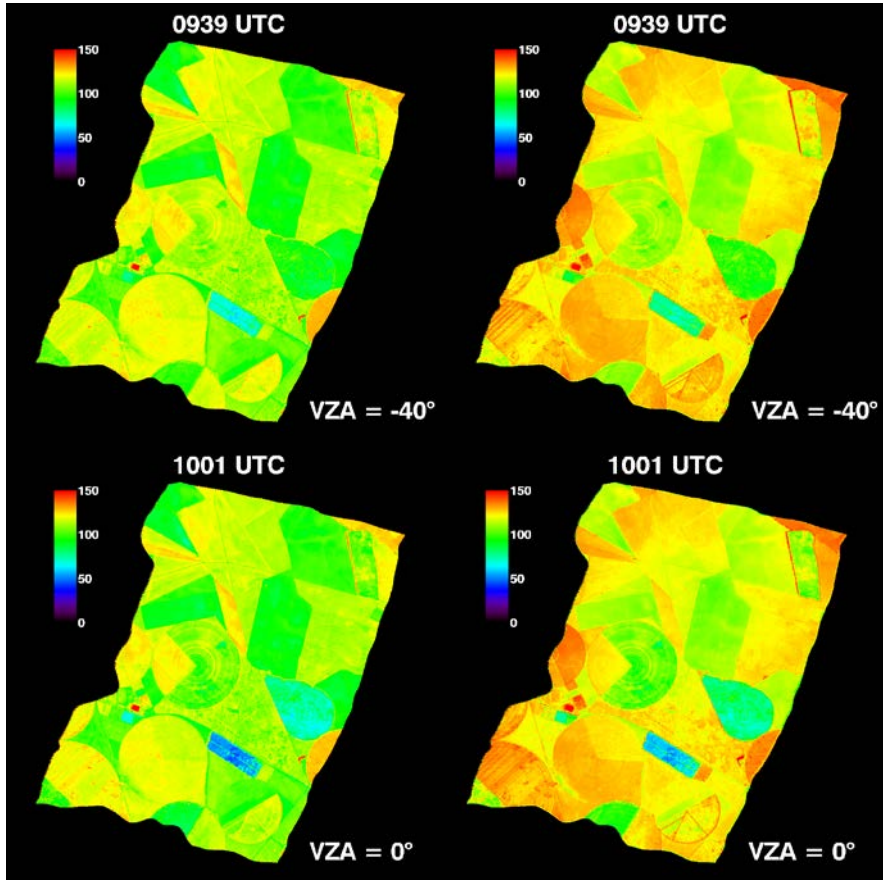


Figure 5.4. G using the albedo estimated from the reflectance (left) and the BRDF (right) 9:39 and 10:01 images (hot-spot (-40°) and Nadir VZA angles).

We observe lower G values when using α_{REF} instead of using α_{BRDF} mainly in bare soils with sparse vegetation. Besides, comparing 9:39 with 10:01 images slightly lower values are obtained both using either α_{REF} or α_{BRDF} . Nevertheless, the images do not present strong angular influences depending on the flight acquisition geometry. This can be attributed to the equation used for estimating G (Eq. 5.4) which considers that G is equal to the R_n multiplied by a term that includes the ratio between the NIR and the red surface reflectance. In a first approximation, the ratio between the

CHAPTER 5

Application: Albedo accuracy impact on evapotranspiration precision

reflectances should minimize the angular effects. However, rationing of the NIR and red spectral bands does not remove surface anisotropy influence due to the spectral dependence of the BRDF response (Gutman, 1991; Roujean et al., 1992). Therefore, when multiplying this term by R_n , this ratio angular dependency may minimize R_n 's.

5.4.4. S-SEBI diagram and Evaporative Fraction (EF)

EF was obtained from the surface temperature and albedo diagram following the S-SEBI method. Figure 5.5 shows the LST vs. α_{REF} and α_{BRDF} scatterplot. Analogously to the previous figures, we just present the plots for two images 9:39 UTC (-40° VZA) and 10:01 UTC (0° VZA). Every image include some pixels of water bodies with minimum values of LST and minimum albedo values located in the bottom of the wet boundary. 9:39 UTC shows high variability of α_{REF} ranging between 0.15 and 0.45. Besides, we observe lower range of α_{REF} values, fluctuating from 0.15 to 0.35, during the near to nadir pass at 10:01 showing the highest pixel frequency around 0.2. However, despite 9:39 image high variability H_{max} presents similar fitting values while LE_{max} parameters are slightly modified. Comparing α_{REF} to α_{BRDF} results we obtain different H_{max} and LE_{max} parameters both at 9:39 and at 10:01. Centering the attention in the LST- α_{BRDF} diagrams, the albedo shows less variability than α_{REF} ranging from 0.1 to 0.25 in both images. This low albedo variation is due to the low heterogeneity of land cover types along the main area during these time period which consists of bare soil areas with sparse vegetation, almost senescent wheat and barley fields and corn fields in the firsts growth stages which may lead to mixed vegetation and bare soil pixels. H_{max} presents slightly different slope when comparing the 9:39 to 10:01 image when using α_{BRDF} while its intercept as well as LE_{max} linear fit parameters shows similar results.

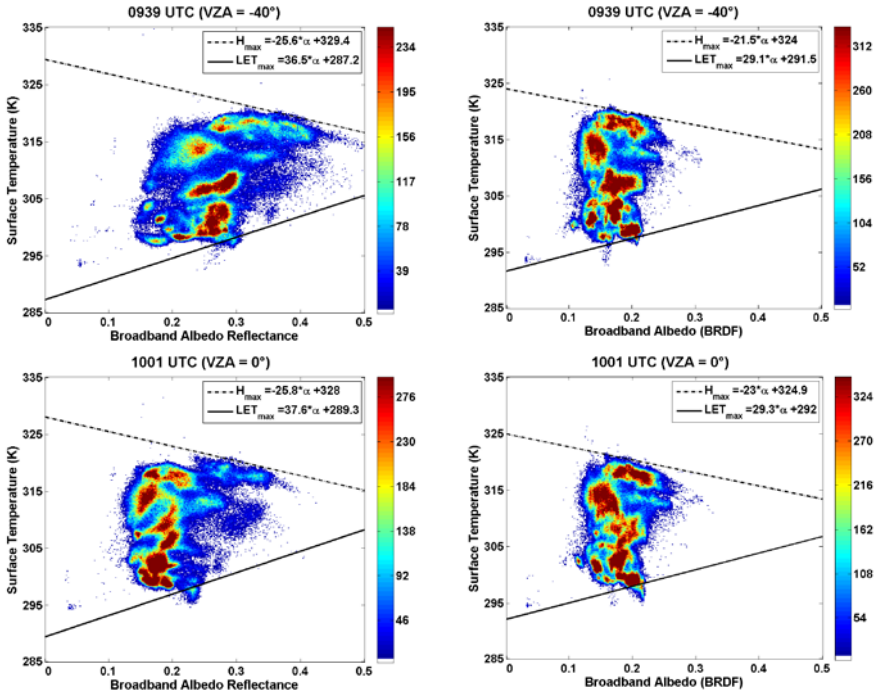


Figure 5.5. Albedo vs. Surface Temperature plots following the S-SEBI model for 9:39 and 10:01 UTC images. The linear fits indicate the upper and lower boundaries according to wet and dry surface assumptions respectively.

Table 5.5 shows the linear fit parameters of all the LST-albedo diagrams and the mean and standard deviation of each parameter. Comparing α_{REF} to α_{BRDF} results, we obtain similar average of H_{max} parameters while LE_{max} shows really different values. In fact, α_{REF} lead to significant higher slopes than α_{BRDF} . The table shows similar standard deviation for each parameter, although in case of α_{LE} when using α_{BRDF} corresponds to a much lower average than α_{REF} . Comparing each flight, H presents the highest difference at 9:54 which nominal VZA was -57° in the orthogonal plane and LE shows the maximum difference at 9:04 and at 9:21 which corresponding VZA were 40° and 57° in the solar plane respectively.

CHAPTER 5

Application: Albedo accuracy impact on evapotranspiration precision

Table 5.5. Linear fit parameters of every LST-albedo diagram, mean and standard deviation.

UTC hour	VZA(°) center	α_H (K)		b_H (K)		α_{LE} (K)		b_{LE} (K)	
		α_{REF}	α_{BRDF}	α_{REF}	α_{BRDF}	α_{REF}	α_{BRDF}	α_{REF}	α_{BRDF}
9:04	40	-51.8	-38.9	328	321	37.9	2.0	286	294
9:11	0	-42.9	-25.3	327	320	31.2	19.9	288	291
9:21	57	-39.7	-42.0	328	324	64.1	15.3	282	290
9:39	-40	-25.6	-21.5	329	324	36.5	29.1	287	292
9:46	40	-15.0	-36.1	321	325	43.3	18.8	287	290
9:54	-57	-9.1	-56.0	324	332	52.5	52.2	281	282
10:01	0	-25.8	-23.0	328	325	37.6	29.3	289	292
Mean		-30.0	-34.7	326	324	43.3	23.8	286	290
Stddev		15.5	12.4	3	4	11.3	15.6	3	4

The results from the table analysis regarding H parameters show similar results (in average) independently on the method considered. Hmax linear fit represents areas with low soil moisture content such as bare soil, fallow land and barren areas where the increasing of surface albedo leads to the decreasing of surface temperature. In contrast, LEmax correspond to areas where the increasing of albedo leads to increasing of temperature. These areas represent irrigated fields where all the energy provided by the increase of temperature is employed in the evaporation process. Results show that they presented the most significant changes when considering α_{REF} instead of α_{BRDF} .

Figure 5.6 presents EF images derived from Eq. 5.5. No strong differences are observed between the EF calculated using α_{BRDF} or α_{REF} . In fact, as seen in Table 5.5, these images do not suppose significant differences between Hmax and LEmax parameters. We observe a slight increase of EF in barren areas comparing 9:39 to 10:01 images both from α_{BRDF} and α_{REF} . Additionally, EF shows slightly lower values in vegetated areas at 10:01 regarding 9:39 using α_{REF} .

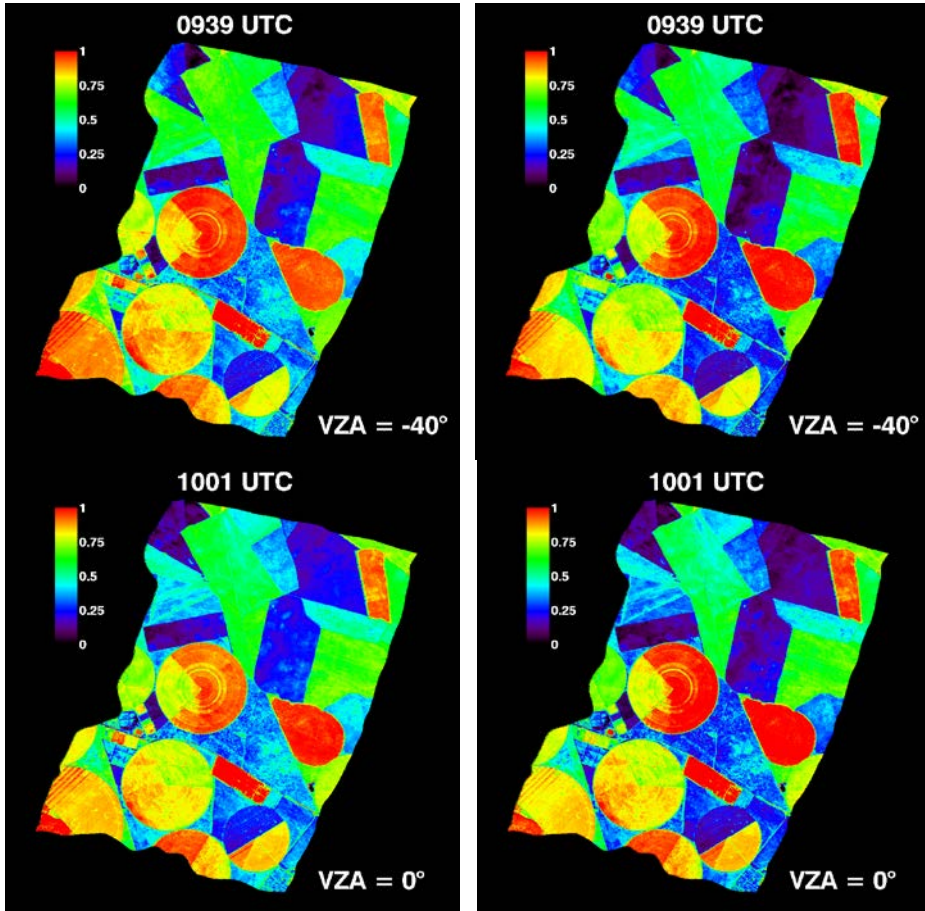


Figure 5.6. EF from α_{REF} (left) and from α_{BRDF} (right) at near to nadir VZA and VZA = -40°

5.4.5. H, LE and Daily Evapotranspiration

Figure 5.7 shows H estimation for observation angles close to nadir and at -40° . Generally, H is underestimated when using α_{REF} both at 9:39 and at 10:01 images. However, this underestimation is more obvious in bare soils with sparse vegetation at 9:39. Comparing 9:39 to 10:01 images, H

CHAPTER 5

Application: Albedo accuracy impact on evapotranspiration precision

showed stable values when using α_{BRDF} . However, in case of α_{REF} the near to nadir image presents slightly lower H values for bare soils and slightly higher values for vegetated fields than for 10:01 image.

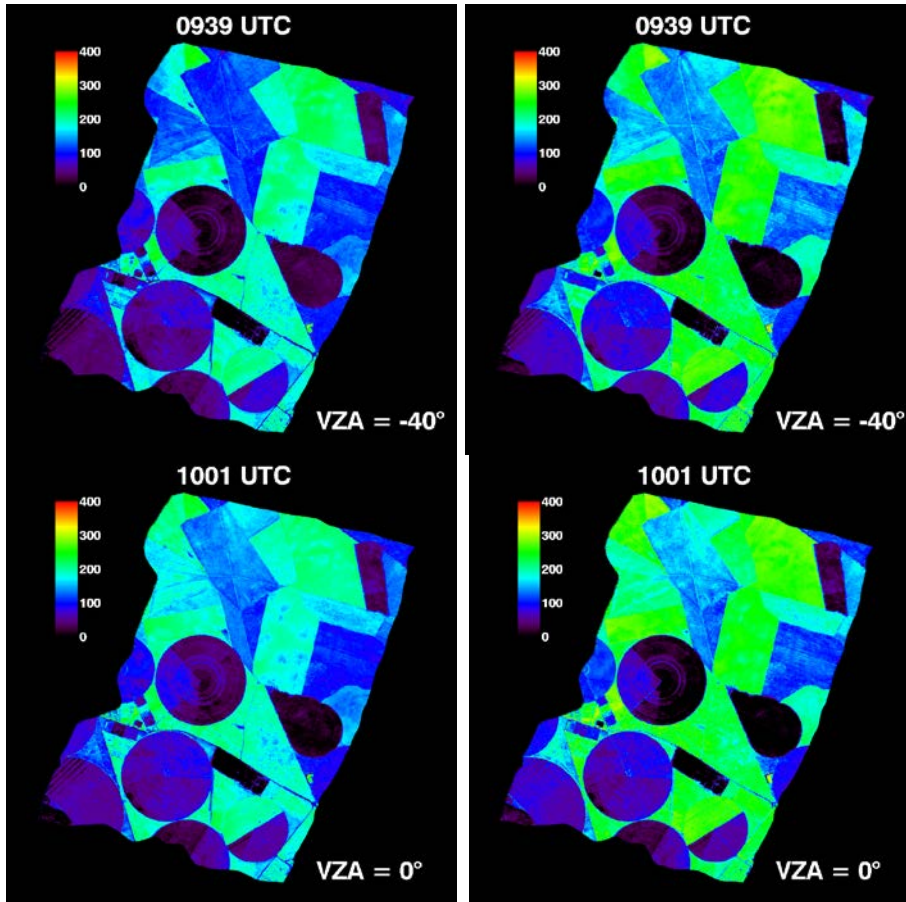


Figure 5.7. H (W/m^2) from α_{REF} (left) and from α_{BRDF} (right) at near to nadir VZA and VZA = -40°

LE images (Figure 5.8) present lower values in crops with denser vegetation when using α_{REF} both at 9:39 and at 10:01. This suggests that using α_{REF} to obtain LE may underestimate it over dense crops. In case of

barren areas, α_{REF} leads to slightly higher values than α_{BRDF} although this is more obvious at 9:39. LE shows stable values both using α_{BRDF} and α_{REF} .

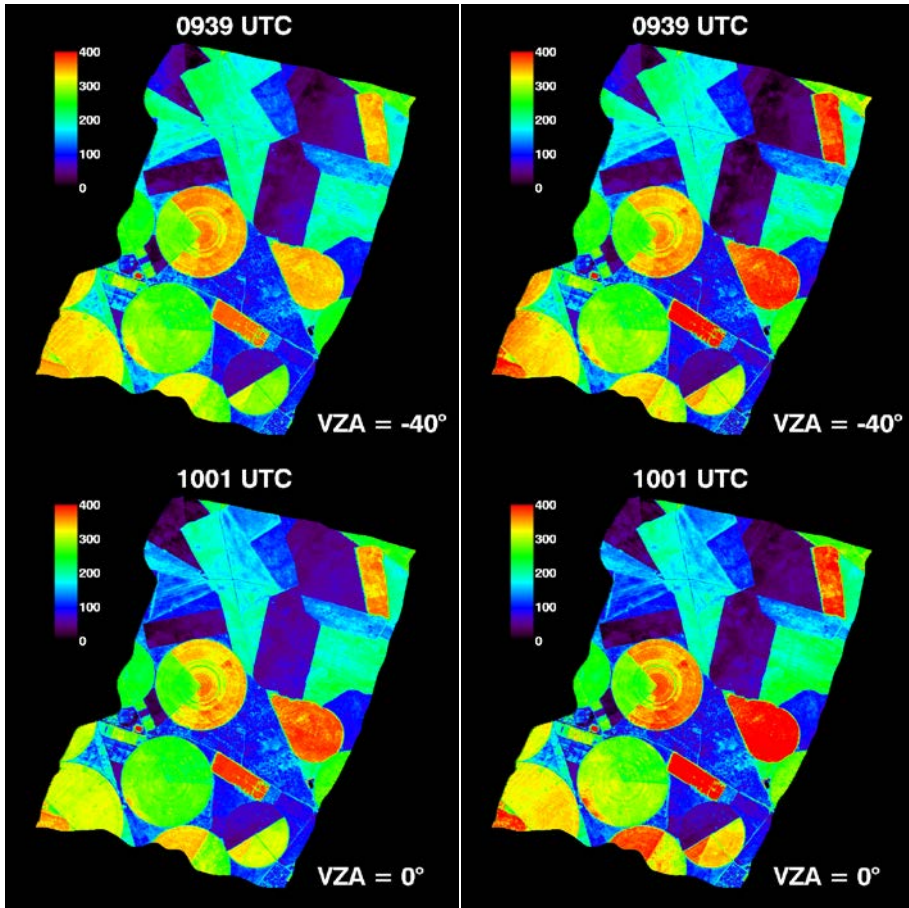


Figure 5.8. LE (W/m^2) from α_{REF} (left) and from α_{BRDF} (right) at near to nadir VZA and VZA = -40°

Finally, Figure 5.9 shows daily ET images. α_{REF} leads to ET underestimation in case of vegetated areas and overestimation in barren areas when compared to α_{BRDF} at 9:39 while presents similar values at 10:01 (near to nadir image). Comparing 9:39 to 10:01 image we obtain stable

CHAPTER 5

Application: Albedo accuracy impact on evapotranspiration precision

values when using α_{BRDF} while α_{REF} shows higher values and more similar to α_{BRDF} at 10:01.

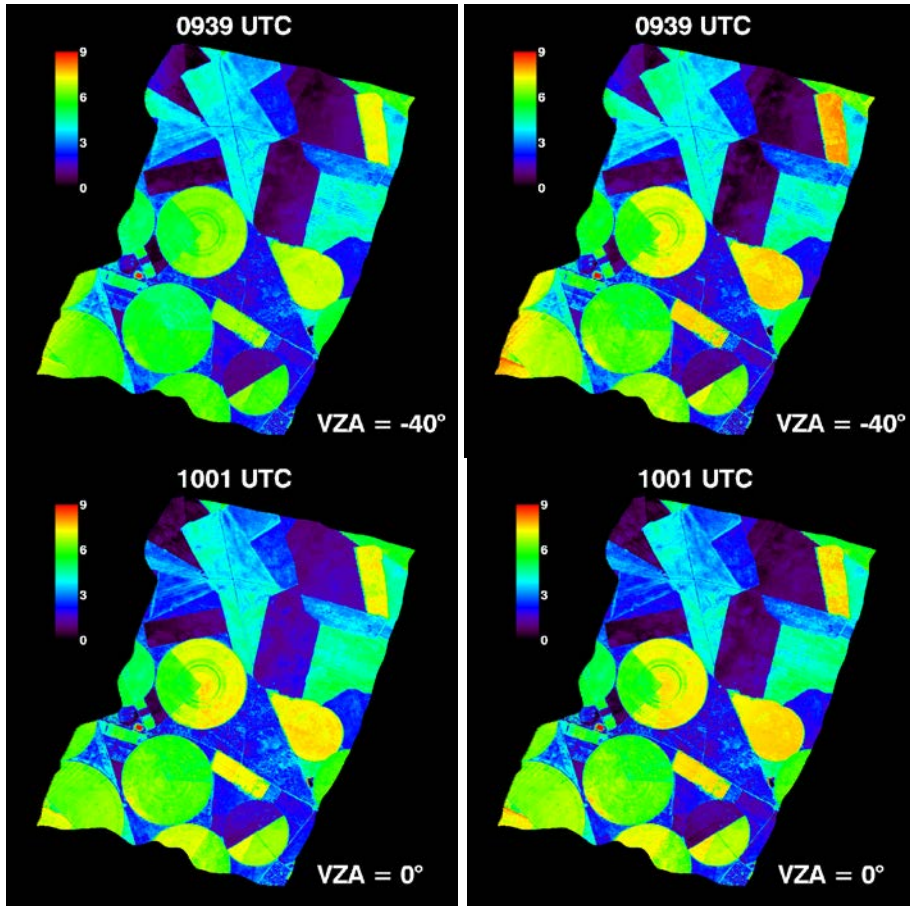


Figure 5.9. Daily ET (mm) images from α_{REF} (left) and α_{BRDF} (right) at Nadir (VZA=0°) and VZA = -40°.

These results show that remotely sensed data acquired with VZA higher than 35°-40° can lead to wrong ET values when the Lambertian assumption is considered to derive the surface albedo.

Tables 5.6, 5.7 and 5.8 summarize the statistical results for H, LE and daily ET estimation for all available acquisitions.

Table 5.6. Statistics of H for each AHS image following VZA and overpass time.

UTC hour	VZA (°)	H(α_{BRDF})	H(α_{REF})	H(α_{BRDF}) - H(α_{REF})		
		Mean (W·m ⁻²)	Mean (W·m ⁻²)	Bias (W·m ⁻²)	Stddev (W·m ⁻²)	RMSE (W·m ⁻²)
9:04	40	143	117	26	20	33
9:11	0	141	111	30	17	34
9:21	57	136	93	42	32	53
9:39	-40	150	118	31	22	38
9:46	40	127	106	21	20	29
9:54	-57	135	106	29	29	40
10:01	0	150	125	25	25	36
TOTAL				29	25	38

Table 5.7. Statistics of LE for each AHS image following VZA and overpass time.

UTC hour	VZA (°)	LE(α_{BRDF})	LE(α_{REF})	LE(α_{BRDF}) - LE(α_{REF})		
		Mean (W·m ⁻²)	Mean (W·m ⁻²)	Bias (W·m ⁻²)	Stddev (W·m ⁻²)	RMSE (W·m ⁻²)
9:04	40	199	194	5	17	17
9:11	0	201	200	2	13	13
9:21	57	206	217	-11	36	37
9:39	-40	191	191	0	15	15
9:46	40	215	204	11	23	25
9:54	-57	205	202	3	29	29
10:01	0	192	186	6	16	17
TOTAL				2	23	24

CHAPTER 5

Application: Albedo accuracy impact on evapotranspiration precision

Table 5.8. Statistics of daily ET for each AHS image following VZA and overpass time.

UTC hour	VZA (°)	ET _d (α _{BRDF})	ET _d (α _{REF})	ET _d (α _{BRDF}) - ET _d (α _{REF})		
		Mean (mm)	Mean (mm)	Bias (mm)	Stddev (mm)	RMSE (mm)
9:04	40	4.28	4.18	0.10	0.36	0.37
9:11	0	4.38	4.47	-0.09	0.25	0.27
9:21	57	4.51	5.04	-0.53	0.39	0.66
9:39	-40	3.94	3.69	0.25	0.32	0.41
9:46	40	4.68	5.03	-0.36	0.24	0.43
9:54	-57	4.47	4.46	0.01	0.23	0.23
10:01	0	3.87	3.99	-0.12	0.23	0.26
TOTAL				-0.10	0.38	0.40

Centering the attention first in H, α_{REF} underestimates this value in every flight, obtaining a general bias of 29 W·m⁻². Additionally, the mean value for each flight shows more variation than using α_{BRDF}. The highest difference between using α_{REF} instead of α_{BRDF} corresponds to 9:21 image (57° in the solar plane) which leads to an error of 53 W·m⁻². The RMSE for each image ranges between 29 to 53 W·m⁻² which imply a relative error from 23% to 39%. The total RMSE considering every image is 38 W·m⁻². This value supposes a relative error of 30%.

Secondly, LE shows lower difference between using α_{REF} or α_{BRDF} with RMSE from 13 to 37 W·m⁻² (relative errors between 6 and 18%). We obtain a total bias of 2 W·m⁻² and a RMSE of 24 W·m⁻² which implies a relative error of 12%.

Finally, no significant differences are observed in daily ET average values through the images excepting 9:21 and 9:46 flights (57° in the solar plane and 40° in the orthogonal plane respectively) where α_{REF} overestimates the average ET. The total RMSE for each image shows values ranging from 0.23 to 0.66 mm·day⁻¹ which suppose a relative error from 5% to 15%. Generally, considering every flight daily ET presents a general bias of -0.10

mm·day⁻¹ (higher ET values using α_{REF} instead of α_{BRDF}), a standard deviation of 0.38 mm·day⁻¹ and a RMSE of 0.4 mm·day⁻¹.

5.4.6. Comparison with in-situ data

In this section we evaluate airborne results by comparing them with in-situ data.

5.4.6.1. Wheat meteorological tower

Figure 5.10 presents the comparison for Rn, albedo and ground flux on the wheat field where the meteorological station was placed. We did not evaluate LET, H and EF in this pixel since the flux tower was not a Bowen station.

The surface broad-band albedo shows good results both in the solar and in the orthogonal plane with RMSE of 0.01 considering α_{BRDF} and 0.03 when using α_{REF} . The main source of error in case of α_{REF} occurs when the VZA is equal to 35° in the orthogonal plane and the backscattering direction which coincides with the hot spot effect. We do not observe significant differences between α_{REF} and α_{BRDF} regarding the other VZA.

In case of the Rn, in-situ measurements present similar magnitudes to airborne Rn when using α_{BRDF} leading to a RMSE of 12 W·m⁻². Moreover, Rn using α_{BRDF} do not present any angular dependency. In case of Rn from α_{REF} a high underestimation is observed for VZA equal to 35° in the orthogonal plane and the backscattering direction which generates the maximum bias of about 60 W·m⁻² (Rn(in situ)-Rn(α_{REF})). This must be a consequence of the albedo overestimation in this VZA due to hot spot. In case of α_{REF} the RMSE is 27 W·m⁻².

Finally, the G evaluation does not present any noticeable difference when α_{BRDF} or α_{REF} was used to compute this flux magnitude. Both G estimations present similar RMSE (around 41 and 40 W·m⁻² for α_{BRDF} and α_{REF} respectively) with a high bias (-40 and -39 W·m⁻² respectively) along the solar and orthogonal plane.

CHAPTER 5

Application: Albedo accuracy impact on evapotranspiration precision

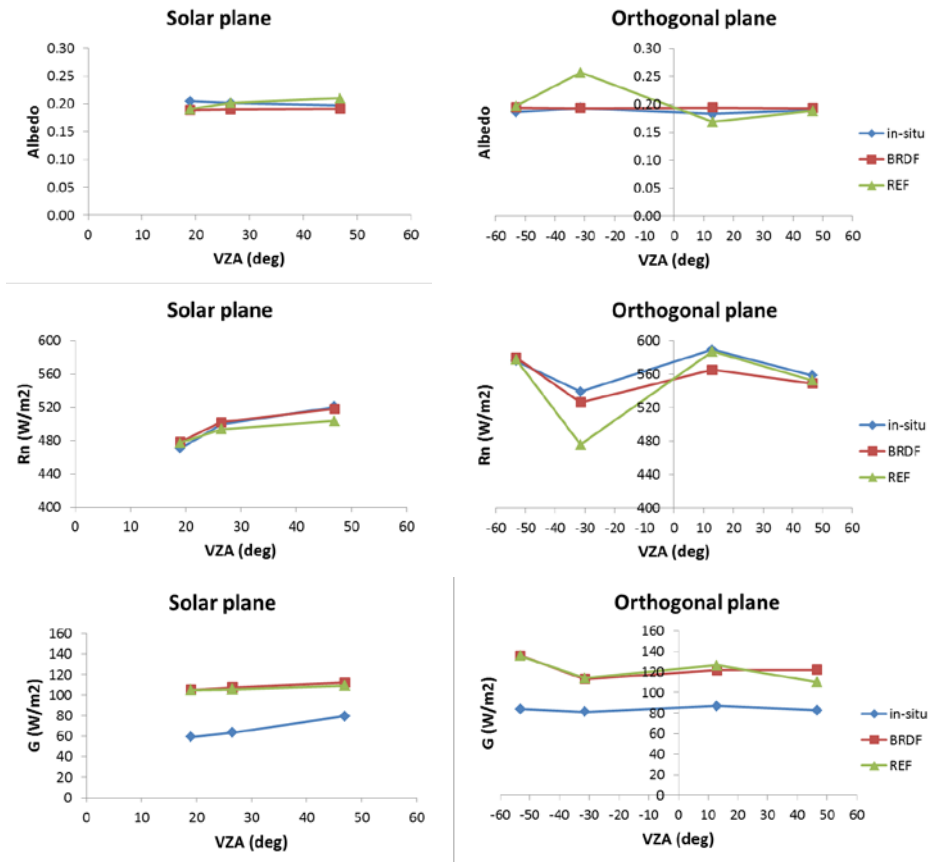


Figure 5.10. Wheat field surface broad band albedo, R_n ($W\ m^{-2}$) and G ($W\ m^{-2}$) time series comparison for each VZA differing between solar and orthogonal planes.

The airborne data overestimation may have two different error sources: the Clothier et al. (1986) algorithm and in situ measurements accuracy. First, this algorithm has been analyzed in previous works such as Payero et al. (2005) where they obtained a RMSE of $37.4\ W\cdot m^{-2}$ in a wheat field which is very similar to our results. Secondly, the instrument used to measure G was the HFP01SC heat flux plate which nominal accuracy is $\pm 3\ W\cdot m^{-2}$. However, Sauer et al. (2003) evaluated six types of commercially available heat flux plates with varying thickness, surface area, and thermal

conductivity. Their results showed that the flux plates underestimate G in the dry sand by 2.4 to 38.5%. In order to improve ground heat flux plate's measurements they need to be corrected for heat stored above the ground heat flux plates although in this study such measurements were not available.

5.4.6.1. Barley eddy covariance tower

Figure 5.11 presents the comparison for albedo and Rn on the barley field where the other meteorological station was placed.

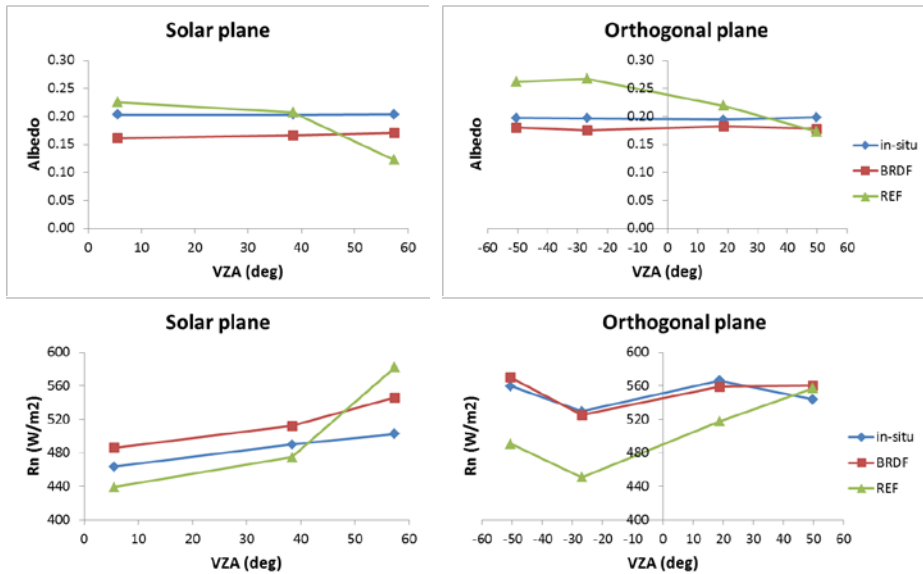


Figure 5.11. Barley field surface broad band albedo and Rn (W m⁻²) time series comparison for each VZA differing between solar and orthogonal planes.

Comparing α_{BRDF} with in situ measurements the surface broad-band albedo shows good results in the orthogonal plane while presents a constant bias of 0.04 showing airborne underestimation in the solar plane. α_{REF} shows a high angular variability both in the solar and orthogonal plane. It is highly overestimated in the backscattering direction while shows similar to in situ

CHAPTER 5

Application: Albedo accuracy impact on evapotranspiration precision

measurements in the forward scattering direction and VZA lower than 40° in the solar plane. The total RMSE is 0.03 considering α_{BRDF} and 0.05 when using α_{REF} .

In case of the Rn, in-situ measurements present similar magnitudes to airborne Rn when using α_{BRDF} in the orthogonal plane while airborne measurements overestimate around 20 W·m⁻² the Rn in the solar plane. In case of Rn from α_{REF} an angular variability is observed leading to a high underestimation in the orthogonal plane. In case of the solar plane Rn is underestimated for VZA lower than 40° while it is overestimated in case of 50° VZA. The total RMSE is 24 W·m⁻² for α_{BRDF} and 58 W·m⁻² for α_{REF} .

Rn and albedo can be directly compared, while for turbulent fluxes comparison (LE and H) footprint theory should be considered. In fact, the footprint of a turbulent flux measurement defines the source areas of the measured vertical fluxes which can be estimated with different footprint models (Schmid, 1994; Kljun et al., 2002; Hsieh et al., 2000). In this study a two-dimensional footprint model is used (Detto et al., 2006) based on the original one-dimensional model of Hsieh et al., 2000.

It is defined as:

$$f(x, y, z_m) = \frac{1}{k^2 x^2 \sqrt{2\pi} \sigma_y} D z_u^P |L|^{1-P} e^{\left(\frac{-D z_u^P |L|^{1-P}}{k^2 x}\right)} e^{-0.5 \left(\frac{y}{\sigma_y}\right)^2} \quad (5.12)$$

where L is the Obukhov length, D and P are similarity constants for unstable, neutral and stable atmospheric conditions, x is the footprint in the upwind direction, k is von Karman's constant, σ_y is the standard deviation of the cross wind direction and z_u is a length scale expressed as

$$z_u = z_m \left(\ln \left(\frac{z_m}{z_0} \right) - 1 + \frac{z_0}{z_m} \right) \quad (5.13)$$

Therefore, H and LE (\overline{F}) maps from S-SEBI model are integrated as a weighted sum over the station source area in order to be comparable to ground data.

$$\overline{F} = \frac{\sum_{i=1}^n f(x_i, y_i, z_m) F(x_i, y_i)}{\sum_{i=1}^n f(x_i, y_i, z_m)} \quad (5.14)$$

where i is the position of a pixel in an image.

Regarding turbulent fluxes comparison, Figure 5.12 shows H, LE and daily ET comparison to in situ data.

H computed both using α_{REF} and α_{BRDF} are clearly underestimated respect to ground data in the solar plane and 20° in the orthogonal plane. Backward scattering and 50° in the orthogonal plane images lead to good results when using α_{BRDF} . Nevertheless, ground data should be considered with caution as can be noticed in the sudden increase of H of almost $100 \text{ W}\cdot\text{m}^{-2}$ at 10:01 (in Figure 5.12 it corresponds to 20° image). Finally, taking into account all acquisition, H presents a RMSE of $88.7 \text{ W}\cdot\text{m}^{-2}$ when using α_{REF} and $79.6 \text{ W}\cdot\text{m}^{-2}$ when considering α_{BRDF} .

For LE, both estimations from AHS images are in good agreement with in-situ measurements with RMSE of 40 for α_{REF} and $49.1 \text{ W}\cdot\text{m}^{-2}$ for α_{BRDF} . LE in the solar plane for VZA lower than 40° is clearly overestimated, which can be probably related to turbulence representation in S-SEBI model.

We could not achieve the daily ET evaluation with in situ measurements since the flux tower failed during the first hours of the day.

CHAPTER 5

Application: Albedo accuracy impact on evapotranspiration precision

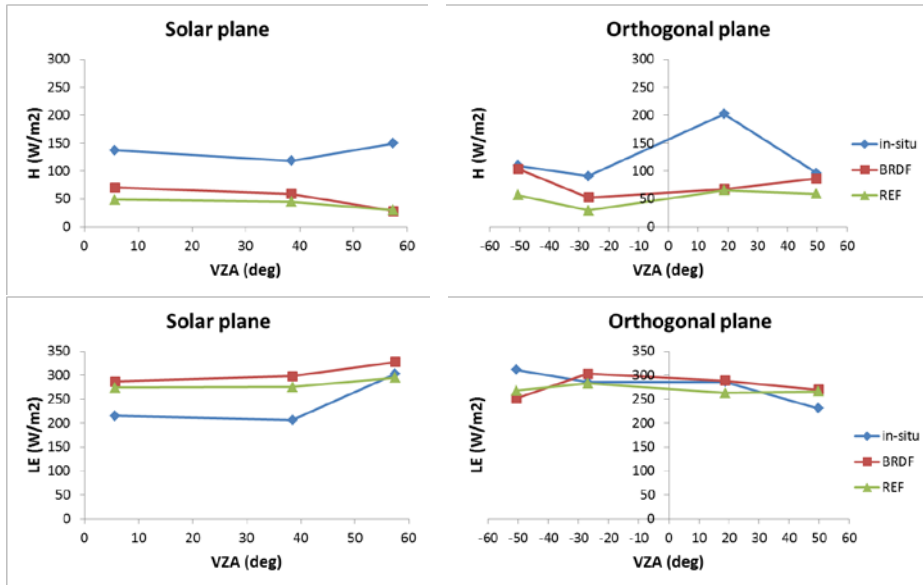


Figure 5.12. Barley field H (W m^{-2}) and LE (W m^{-2}) time series comparison for each VZA differing between solar and orthogonal planes.

This study shows that using the surface reflectance weighted average instead of the albedo from the BRDF integration may lead to errors in the R_n and daily ET estimation mainly for VZA higher than 35° and along the hot spot region. Therefore, for future ET studies we suggest the appropriate use of the RTLSR-HS modeled albedo.

CHAPTER 6

APPLICATION: ALBEDO EVOLUTION AND IMPACT ON LAND SURFACE TEMPERATURE

In this chapter we study the albedo evolution over a Europe and northern Africa scene from 2002 to 2011 taking advantage of the MODIS CMG albedo images processed and analyzed in Chapter 4. As we explained exhaustively in the introduction of this thesis, land cover change, represented by the albedo variation, may impact the local, regional or even the global climate depending on where the perturbation occurs (Jackson et al., 2008). Therefore, we centered the attention in those pixels where higher variations of surface albedo were detected looking into the cause of the

CHAPTER 6

Application: Albedo evolution and impact on land surface temperature

albedo change. Additionally, we processed the simultaneous land surface temperature (LST) and air temperature in order to analyze the impact of albedo change on the temperature.

6.1. METHODS

In Chapter 4.3 we worked with white sky albedo. We concluded that the best method compared to the MCD43 product was the 5parameter Rsqr. Therefore, in this chapter we work with the data derived from the proposed method. However, in this study we will analyze the bluesky albedo which was estimated following Eq. 1.35. In order to derive the fraction of diffuse skylight we took advantage of MODIS CMG aerosol optical thickness (AOT) data. Then we built a small look up table from 6S simulations.

LST was estimated using the Split Window method (Sobrino et al., 2003).

$$LST = T_{31} + a_1 + a_2(T_{31} - T_{32}) + a_3(T_{31} - T_{32})^2 + (a_4 + a_5W)(1 - \varepsilon) + (a_6 + a_7W)\Delta\varepsilon \quad (6.1)$$

where T_{31} and T_{32} are brightness temperature for MODIS bands 31 and 32 respectively, ε and $\Delta\varepsilon$ are respectively the average emissivity and the spectral emissivity difference for these bands, W is the total amount of water vapor obtained from the information of CMG data, and $a_1 = 1.02$, $a_2 = 1.79$, $a_3 = 1.20$, $a_4 = 34.83$, $a_5 = -0.68$, $a_6 = -73.27$ and $a_7 = -5.19$, obtained from MODTRAN simulations (additional information about these parameters can be found in Sobrino et al., 2003).

Emissivities were estimated from Fraction Vegetation Cover (FVC) and MODIS band 1 information, following the methodology presented by Sobrino et al. (2003). These emissivities correspond to MODIS thermal bands 31 and 32, and were estimated differently depending on the NDVI value of a given pixel.

Emissivities were expressed as average emissivity ϵ (for bands 31 and 32) and spectral difference of emissivities $\Delta\epsilon$ (Table 6.1).

Table 6.1. Estimation of surface emissivity.

	ϵ	$\Delta\epsilon$
<i>Vegetation: NDVI > 0.5</i>	0.99	0
<i>Mixed: 0.2 ≤ NDVI ≤ 0.5</i>	$0.971 + 0.018 FVC$	$0.006 (1 - FVC)$
<i>Bare soil: NDVI < 0.2</i>	$0.9832 - 0.058 \rho_1$	$0.0018 - 0.060 \rho_1$

FVC was estimated from NDVI parameter following Gutman and Ignatov (1998) for day-time acquisitions as a normalization of NDVI between standard bare soil and dense vegetation values. In the case of MODIS, these values are respectively 0.15 and 0.90 (Camacho et al., 2006). Therefore,

$$FVC = \frac{NDVI - 0.15}{0.90 - 0.15} \tag{6.2}$$

The air temperature was extracted from MODIS CMG Collection 6 data. It corresponds to the air temperature at 2m height.

6.2. RESULTS

Focusing first on the albedo variation, Figure 6.1 shows the slope value of the albedo evolution from 2002 to 2011 for each pixel through the Europe and Northern Africa scene. It was divided by the mean over the years considered and multiplied by 100 in order to obtain percentage values. Although the albedo evolution cannot be represented by a linear fitting, the slope just shows its positive or negative tendency.

CHAPTER 6

Application: Albedo evolution and impact on land surface temperature

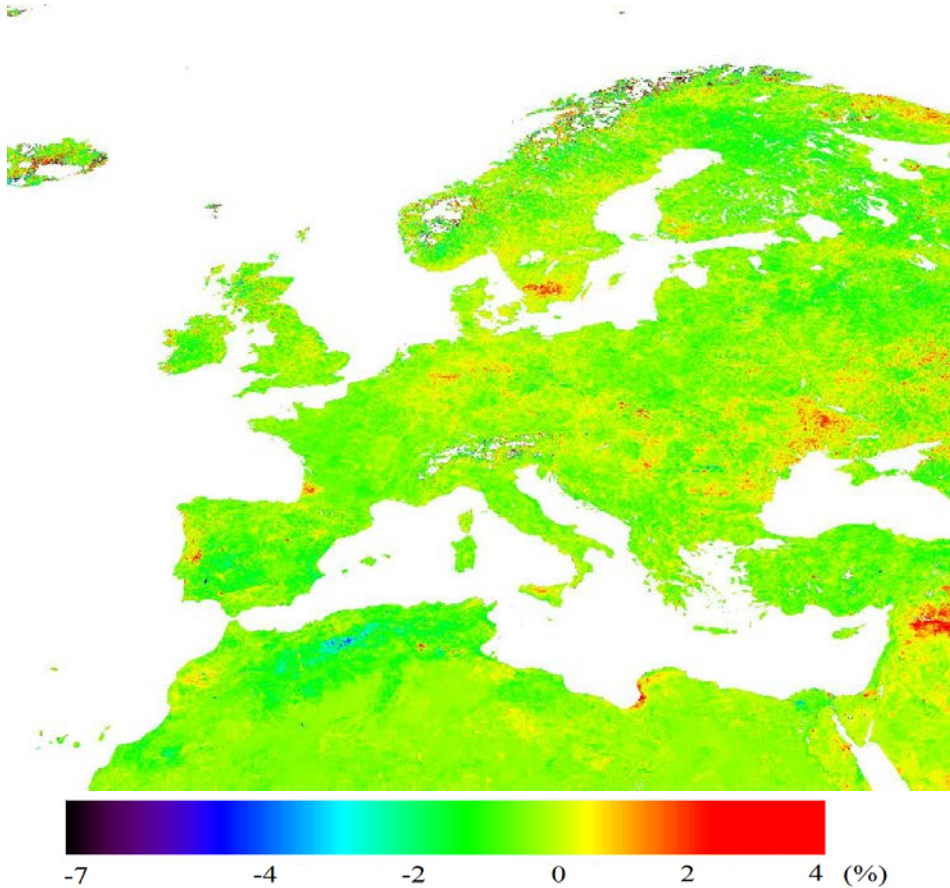


Figure 6.1. Slope in percentage of the albedo evolution from 2002 to 2011 over Europe and Northern Africa.

This image displays positive slopes in the center of Portugal, some localized areas of Spain, Bordeaux area, south of Sweden, east of Germany, south of Ukraine and Syria. On the contrary, negative slopes are obtained in the south east of Portugal and north of Algeria. Next, we focus on some of these cases to investigate how and why the albedo changed and its impact on the LST and air temperatures. We divide the study into four categories of hazards responsible of the albedo increase: forest fires, wind storms, floods

and droughts. Finally, we also analyzed areas where the albedo decreased during the period considered.

6.2.1. Forest fires

First of all, Figure 6.2 shows the albedo, LST and air temperature from those pixels where the albedo change was caused by a forest fire. We just represented the most important forest fires which implied the highest burnt areas.

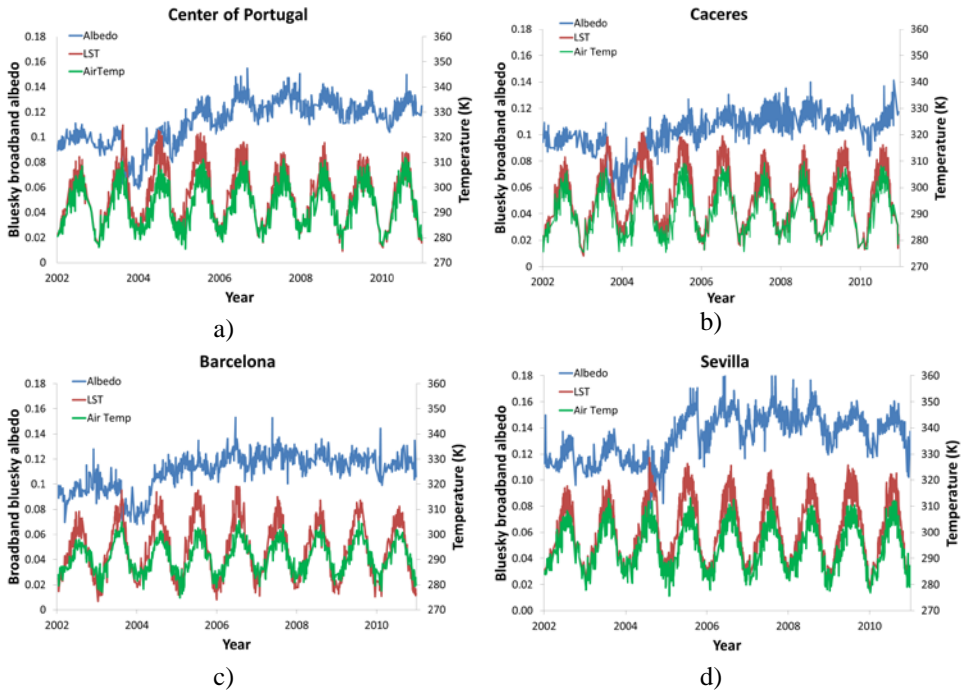


Figure 6.2. Albedo, LST and air temperature evolution in areas where forest fires caused a change in albedo.

CHAPTER 6

Application: Albedo evolution and impact on land surface temperature

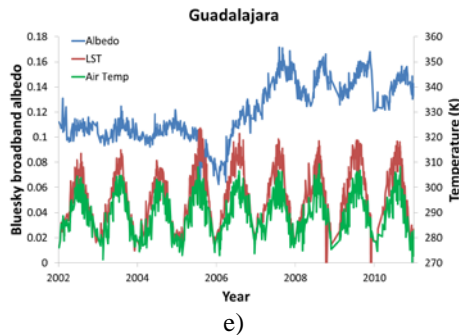


Figure 6.2. Albedo, LST and air temperature evolution in areas where forest fires caused a change in albedo (continued).

During summer of 2003 there was a severe heat wave that hit Western Europe. This caused forest fires in the north and center of Portugal (39.90°N, 8.00°W, Figure 6.2a) with 450,000 ha of total burnt area (Trigo et al., 2006), in Caceres (40.40°N, 6.35°W, Figure 6.2b) with a total of 9,000 ha of forest burnt area and in Barcelona (41.75°N, 2.00°E, Figure 6.2c) with 4,600 ha of total burnt area among others (Spanish Ministry of Environment). In August of 2004 there was a forest fire between Huelva and Sevilla (37.65°N, 6.45°W, Figure 6.2d) that burnt a total of 35,000ha. Finally, in July of 2005 a forest fire in Guadalajara (41.00°N, 2.25°W Figure 6.2e) burnt 13,000 ha. In every case we observe the same behavior of the albedo which decreases suddenly after the forest fire (the surface gets dark) and then increases to higher values than before the fire representing barren areas values. The albedo average before and after the fire changes from 0.10 to 0.14 in Portugal, from 0.10 to 0.12 in Caceres and Barcelona, from 0.12 to 0.16 in Sevilla and from 0.11 to 0.16 in Guadalajara. Regarding the temperatures, after the fire the difference between LST and air temperature is higher than before as it is expected due to the increase of the albedo. Additionally, the LST presents higher maxima after the fire.

Figure 6.3 shows the evolution of the amplitude, defined as the difference between summer LST maxima and winter LST minima in these pixels.

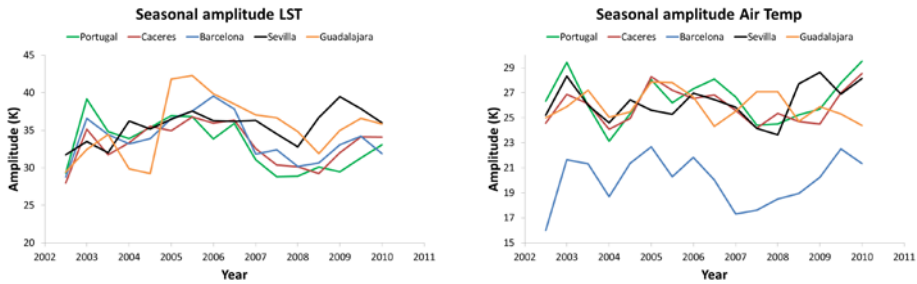


Figure 6.3. Seasonal amplitude of the LST and the air temperature.

We notice changes in the LST seasonal amplitude caused by the fire events in Portugal, Caceres and Barcelona where the LST amplitude increases in 2003 from 30 K to an average of around 35 K until 2007. After that the amplitude decreases to similar values to the ones observed before the fire. Sevilla pixel presents similar behavior, increasing the LST amplitude from 33 K before 2004 to around 36 K until 2007. However, in this case the amplitude shows a maximum value in 2009 that cannot be associated to the fire event in 2004. Finally, Guadalajara shows the highest influence to the fire event increasing its average LST amplitude from an average of 32 K before 2005 to 40 K after 2005. Nevertheless, the LST amplitude decreases slowly through the years reaching from 2008 slightly higher but similar values to the ones before the fire. Regarding the air temperature amplitude, Barcelona shows the lowest amplitudes since it is located by the sea which moderates its temperatures. Additionally it is the only pixel which air temperature seasonal amplitude presents an increase from 17 K before 2003 to an average of 21 K until 2007. However the amplitude increases from 2007 to 2009 reaching similar values to the ones after the fire event. We observe a generalized decrease of the amplitude in 2004 caused by slightly higher temperatures during the winter of 2003-2004. The other pixels do not present any influence on the air temperature amplitude.

Next we fitted the LST and air temperature evolution through the years linearly in order to see if they presented any increasing or decreasing tendency. This provides a tendency of the average temperatures during the

CHAPTER 6

Application: Albedo evolution and impact on land surface temperature

period considered. Table 6.2 shows the slopes in percentage analogously to the albedo analysis in Figure 6.1.

Table 6.2. Slope in percentage of the LST and air temperature evolution from 2002 to 2011 in burnt areas pixels.

	Slope LST (%)	Slope Air Temp (%)
Center of Portugal	-0.46	2.00
Caceres	0.72	1.73
Barcelona	0.13	1.39
Sevilla	1.72	0.59
Guadalajara	2.60	0.81

Sevilla and Guadalajara show positive and the highest slopes of LST with values around 2% while present the lowest slopes of air temperature. On the contrary, Portugal, Caceres and Barcelona pixels air temperature slopes are the highest and around 2% (although Barcelona slope was lower) and show low slope values for the LST. The highest values of the LST slope for Sevilla and Guadalajara pixels coincide with the places with highest albedo change after the fire event (as commented in Figure 6.2. Besides, the highest slopes of air temperatures in Portugal can be attributed to the highest extension burnt though we did not find any physical explanation to Caceres and Barcelona cases from the information available. It might be caused by other factors such as the evapotranspiration change of each place.

From this analysis we conclude that forest fires which take place in southern latitudes influence the LST by increasing the seasonal extreme temperatures. This effect lasts three to four years while the albedo reestablishment takes longer. We also have noted that higher changes in albedo imply higher changes in LST. We do not notice significant changes of the air temperature extreme seasonal values.

6.2.2. Wind storms

Figure 6.4 shows the particular case of the Bordeaux area and south of Sweden forest.

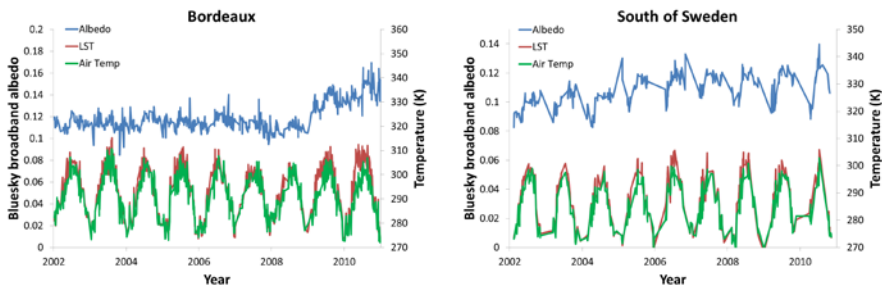


Figure 6.4. Albedo, LST and air temperature evolution in Bordeaux and south of Sweden.

The albedo variation of the Bordeaux area (located in a pine forest in Les Landes region) was associated to the winter storm Klaus (an extratropical cyclone) that damaged approximately 300,000 ha of forest in January of 2009. On 8th January 2005, the Gudrun storm caused the largest amount of reported storm damage ever in Sweden. A total of 270,000 ha of forest were demolished in the south of Sweden (Bengtsson & Nilsoon, 2007). In Bordeaux pixel (44.25°N, 0.60°W), the plot shows an increase of the albedo from 0.12 to 0.14. LST and air temperature present similar values before the storm although after 2009 they show different values mainly during the summer. On the contrary, the Sweden pixel (57.10°N, 13.05°E) does not show a significant albedo change mainly due to the high noise and few available data. This is a result of not taking into account snow pixels and additionally the difficulty of having clear pixels (with no clouds) in northern latitudes. In fact, a sudden increase of albedo is observed at the beginning of 2005 that lead to a sudden decrease followed by a slight positive tendency from then on. The low albedo change from an average of 0.10 before the storm to an average of 0.12 after the storm do not cause strong changes in the temperatures although a slight increase of the minimum temperatures during winter and a slight increase in the maximum temperatures during summer can be guessed after 2005.

Regarding the influence of the albedo change in the temperatures, Figure 6.4 plots show lack of temperature data during the winter (mainly in Sweden) which can lead to an overestimation of minimum temperatures. Therefore, in this case we cannot estimate the seasonal amplitude of the

CHAPTER 6

Application: Albedo evolution and impact on land surface temperature

temperatures. Figure 6.5 displays the LST and air temperature yearly average of these pixels.

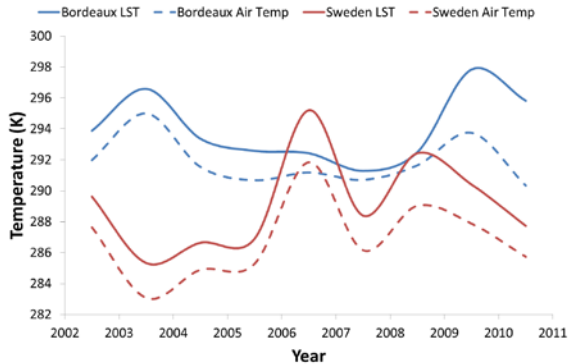


Figure 6.5. Yearly average of LST and air temperature in Bordeaux and Sweden pixels.

In case of Bordeaux an increase of 6K is detected on the LST yearly average in 2009 which could be consequence of the wind storm during January of 2009. However this area also presents a peak of LST in 2003 which can be attributed to the heat wave that hit Wester Europe during the summer of this year. The air temperature shows a slight increase in 2009 of 2 K. With reference to Sweden, a high increase of both LST and air temperature is detected in 2006 of 7K in both cases. However, the wind storm occurred in January of 2005 hence, we do not detect any temperature variation as consequence of the albedo increase.

6.2.3. Floods and land slides

Figure 6.6 shows the albedo, LST and air temperature evolution in a pixel in the west of Germany and south of Poland.

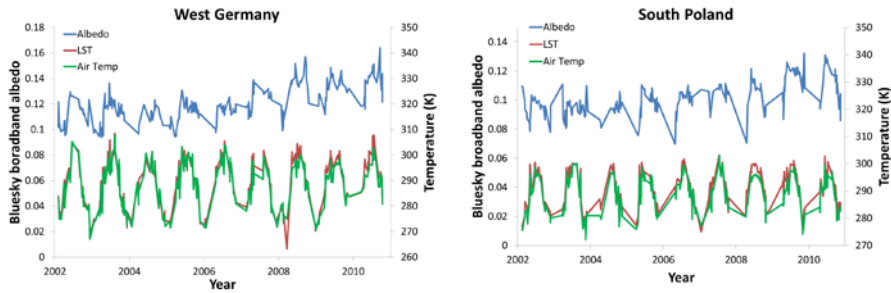


Figure 6.6. Albedo, LST and air temperature evolution in the west of Germany and south of Poland.

At first sight we notice higher dispersion of the albedo data in both sites compared to previous plots. This is consequence of the lack of data during winter since they are covered by snow and therefore masked out of the image. Starting with the west of Germany pixel (51.35°N , 7.75°E), it is located in a forest area nearby Dortmund city in Westphalia region where a heavy precipitation event occurred on 26th July of 2008 that led to floods. Looking to the plot, a slight increase of albedo can be observed from 2008. Regarding the temperatures variation, we notice differences between LST and air temperatures after 2008 which denote a change in the surface. In case of the south of Poland pixel (49.65°N , 19.05°E), we detect an increase of albedo tendency through the Beskydy Mountains from 2007. Plot 6.6 shows winter lack of data followed by some sudden decreases of the albedo in spring of 2005, 2006 and 2008. Therefore, these decreases of albedo can be associated to snowmelt floods which are causing landslides and erosion through the Beskydy Mountains (Pánek et al., 2011). This hazard increases slightly the albedo after 2007. In this case we also observe a difference between LST and air temperature after 2007.

Figure 6.7 displays LST and air temperature yearly average for both sites.

CHAPTER 6

Application: Albedo evolution and impact on land surface temperature

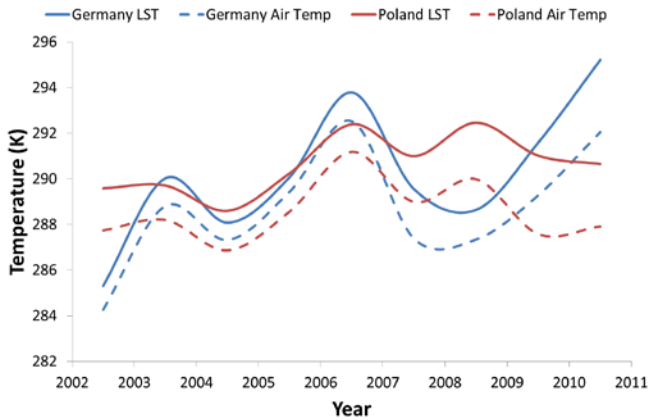


Figure 6.7. Yearly average of LST and air temperature in west of Germany and south of Poland pixels.

Germany pixel shows a peak of both LST and air temperature yearly averages in 2006. On the contrary, the year when the flood event occurred (2008), shows a decrease of both LST and air temperature. Since then, LST and air temperature increase during 2009 and 2010, reaching maximum values. Regarding Poland pixel, LST presents two similar peaks in 2006 and in 2008 but we do not appreciate any significant change in temperature after 2007. Therefore, no tendency can be guessed consequence of the slightly albedo increase in both sites.

6.2.4. Droughts

Figure 6.8 shows the albedo, LST and air temperature evolution in a pixel in Syria (35.90°N, 38.85°E) along the Euphrates valley. The plot shows an increase of the surface albedo from 2007 from an average of 0.25 to an average of 0.33. In fact, the albedo evolution before 2007 corresponds to a typical agricultural area with seasonal albedo variations. However since 2007 we observe more stability in albedo. This behavior can be consequence of a severe drought in 2007 and 2008 that affected 1.3 million people and diminished the nation's wheat yields.

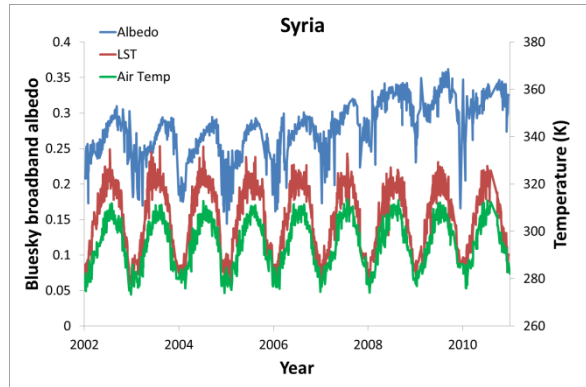


Figure 6.8. Albedo, LST and air temperature evolution in Syria pixel.

Regarding the temperatures, both LST and air temperature show similar values through the time series studied. However, in order to dig into this parameters' variability, Figure 6.9 shows the seasonal amplitude and the yearly average of LST and air temperature in this pixel. The seasonal amplitude do not show any pattern that differed 2007 or 2008 from other years. However, the yearly average of LST shows a minimum value in 2007 although the difference with the previous year is only 2 K. Considering this area's extreme temperatures this decrease on the average temperatures cannot be considered as consequence of the albedo increase.

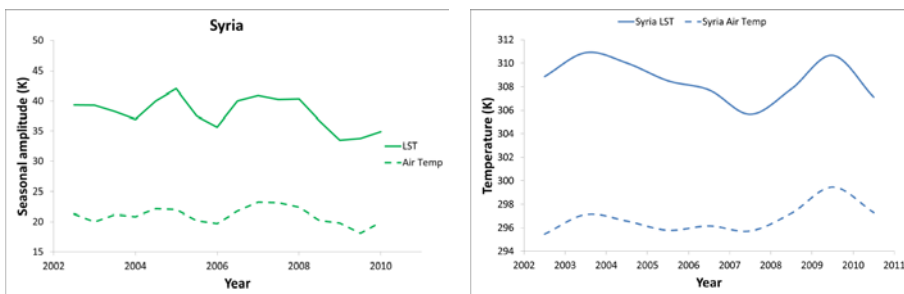


Figure 6.9. Seasonal amplitude (left) and yearly average (right) of LST and air temperature in Syria pixel.

CHAPTER 6

Application: Albedo evolution and impact on land surface temperature

6.2.5. Decrease of albedo

Figure 6.1 showed important decrease in albedo in a region located in the south east of Portugal and a region in the north of Algeria. Figure 6.10 shows the temporal evolution of the albedo, LST and air temperature of these regions.

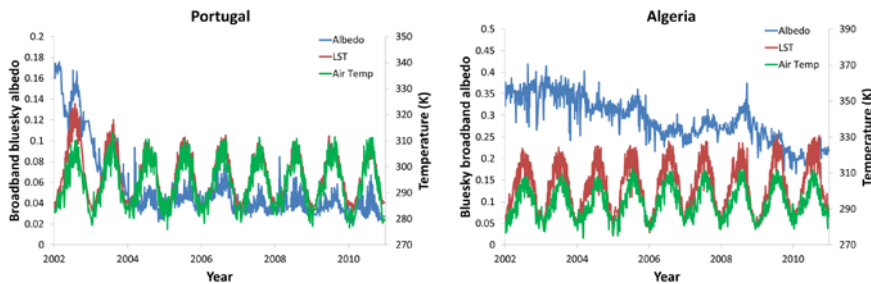


Figure 6.10. Albedo, LST and air temperature evolution in Portugal and Algeria pixels.

In case of Portugal pixel (38.3°N, 7.45°W) the plot shows a sudden decrease of albedo in 2003. This is associated to the Alqueva dam, which was inaugurated in 2002. This dam is located on the Guadiana River in the Alentejo region of Portugal. The reservoir is the largest in Portugal and Western Europe taking up a surface area of 250 km². Regarding the temperature, LST shows a decrease in its maximum value after 2002. Additionally, LST presents equivalent values to the air temperature after 2003.

In case of Algeria (34.6°N, 1.60°E), the area analyzed is located in the southern region between the Tell Atlas and Saharan Atlas. It consists of a high plateau (~1000 m in elevation) with level terrain where water collects during the wet season, forming large shallow salt lakes (and as they dry, salt flats). Therefore, depending of the year precipitations the area can be covered by water or salt. That may be the reason of the albedo variation. We do not appreciate significant changes in temperature as a result of the albedo decrease.

Briefly, in this study we observed albedo change impact on LST in case of fire events and wind storms located in the Southern Europe increasing in the first case extreme temperatures and yearly average temperatures in the second case. Wind storms and floods placed along central and northern Europe did not imply any alteration neither on LST nor on air temperature, although the magnitude of these events did not change significantly the albedo. We did not detect any impact more arid areas such as Syria despite the albedo strong increase. In every case, air temperature showed higher differences with LST values after the albedo changes. However, air temperatures did not present any significant variation.

CHAPTER 6

Application: Albedo evolution and impact on land surface temperature

CONCLUSIONS

In this work we developed three different studies looking for an improvement in the surface albedo estimation.

First of all, we studied the influence of including the BRDF coupling in the atmospheric correction. Several conclusions could be obtained from this study. First, the effect of surface anisotropy is stronger in the green band (with errors from 3 to 12%) than the red band (with errors from 2 to 8%) and smaller in the near infrared band (with errors from 0.7 to 5.0%). However, these errors barely influence the NDVI estimation, obtaining relative RMS around 1%. Second, the difference between ρ_2 and ρ_3 , that is, considering the first iteration ($BRDF_1$) or the second iteration ($BRDF_2$), is around 1-2% in the red band, 1-3% in the green band and almost insignificant (around

CONCLUSIONS

0.2%) in the near infrared. Third, high amounts of aerosols lead to higher influence of the BRDF surface effects. Fourth, we noticed higher errors in the forward scattering direction than in the backward scattering. Fifth, the bias analysis showed that surface reflectance is overestimated in the forward scattering and is underestimated in the backward scattering when assuming a Lambertian surface.

Regarding the albedo estimation, we obtained errors from 1.5 to 5.0% both in the red and green bands and from 0.7 to 3.0% in the near infrared. In the case of the broad band white sky albedo, we obtained RMS errors around 1% which agrees with previous works. Additionally, the small negative bias values (from $-4 \cdot 10^{-4}$ to $-10 \cdot 10^{-4}$), indicate that the Lambertian assumption only generates a slight overestimation of the albedo.

To sum up, the assumption of Lambertian surface can be used satisfactorily in the derivation of surface reflectance and surface albedo. In fact, the obtained RMS of 1% in case of the surface albedo estimation meets the accuracy requirement of 5% suggested by the Global Climate Observing System (GCOS, 2006). However, it should be used carefully for high aerosol amounts since this can result in a significant error in the surface reflectance estimation.

Besides, we evaluated the MODIS BRDF/albedo product over an agricultural heterogeneous area in the framework of the EODIX campaign. In this way we applied two BRDF models to AHS airborne data, the RTLSR and the RTLSR-HS to obtain the surface albedo. The results show, a good agreement between the RTLSR model (MODIS BRDF/albedo product algorithm) and the RTLSR-HS model when compared to in situ data with a RMSE of 0.018 in both cases. However we observed a slight underestimation (more significant in the corn field by the RTLSR model and in the barley field by both models) which has been already reported in previous works such as Roesch et al. (2004) or Liu et al. (2009). In fact, we observed that the corn field (which during June was in its growing phase) and the wheat field (which was entering its senescent phase) showed a better agreement with in situ data than the barley field (which was already

CONCLUSIONS

senescent). These facts agree with Jin et al. (2003) who observed good results during the growing season and underestimation during other periods.

Regarding the comparison between airborne and satellite data, the aggregation of AHS pixels led to a RMSE of 0.04 for both models. This error is not only a consequence of the aggregation technique, but is also due to the methodology applied to estimate the BRDF. We must take into account that MODIS BRDF/albedo algorithm considers that the surface does not change during 16 days which is a coarse approach when working with agricultural sites entering their senescence period. However, the AHS data correspond to a single day composition. Additionally, we must emphasize the difficulty of comparing satellite to airborne or in situ data during this study because of the area heterogeneity. Nevertheless, since airborne images presented a good agreement with in situ data, the RMSE of 0.04 proves that MODIS BRDF/albedo product meets the required accuracy of 0.02-0.05 in the surface albedo estimation. Additionally, considering a homogeneous pixel (barley field), we found a good agreement between the satellite estimation (0.210 ± 0.003) and the in situ albedo measurement (0.204 ± 0.003).

This study shows that both the RTLSR and the RTLSR-HS models provide equivalent results. The greatest difference between both models is evidenced in the hot spot region where we did not dispose of in situ measurements. Therefore, both models can be used in future works indistinctly in the albedo estimation but considering RTLSR-HS should improve slightly its precision and correct the hot spot effect.

Finally, we compared the MCD43 MODIS product with different BRDF inversion methods through the white sky albedo analysis. Moreover, we presented and studied three methods that strengthen the VJB method and improve its time processing.

The results show that both the VJB and the proposed methods present good agreement with the MCD43 MODIS product, obtaining errors lower than 0.02 for most cases. The main discrepancies with the MODIS product were detected along mountainous areas in the winter season. As commented

CONCLUSIONS

in Chapter 4 the reason must be due to the lack of data which may lead to insufficient angular sampling. Therefore, in these cases the difficulty of obtaining the BRDF leads to higher errors regardless of the method considered. In case of the MODIS product, these situations are solved using a backup algorithm which constrains the BRDF shape from prior information but adjusts it to match the observations made (Strahler et al, 1999). In case of the VJB method and the proposed methods, they are based on V and R dependency on the NDVI over a year. The VJB particularly divides the NDVI into five classes with equal population. Considering the lack of data during the winter in these pixels, they must be less represented by the V and R fitting. The proposed methods consider all the data through a year to invert the BRDF, which gives less weight to less frequent data. However, when comparing the methods proposed to the VJB we obtained similar values although the VJB provided higher errors in mountainous areas while the proposed methods led to higher errors in the east of Spain, Italy, Germany and south of Sweden. Overall, considering every pixel and all the data the VJB method RMSE was 5.0%, while it was 6.1%, 5.1% and 5.3% for the 4parameter, 5parameter Rsqr and 5parameter Vsqr methods respectively. Consequently, the VJB and the 5parameter Rsqr methods provide the lowest error. The results, therefore, lead to the same conclusion as Breon & Vermote (2011) (although they analyzed the normalized reflectance) that the VJB method (as well as the three methods proposed) provides equivalent albedo results to the MDC43 MODIS product with the advantage of daily versus a 16-day temporal resolution.

Regarding the methods proposed we also obtain equivalent results to the VJB method with the advantage of being more robust algorithms that avoid the NDVI classification into five different classes and that speeds up the time processing. Among the three methods, including a fifth parameter (5parameter Rsqr and 5parameter Vsqr versus 4parameter) supposes an additional parameter in the system equation which slightly slows down the time processing. However, it improves 4parameter results from 6.1% to 5.1% when using 5parameter Rsqr, showing higher differences mainly in mountainous areas, along arid areas in the north of Africa, along Germany and Poland and north-east of Europe. Finally, we propose the 5parameter Rsqr method as an alternative to the VJB method since it provides the best

results mainly in mountainous regions during the winter season, while reducing significantly the processing time needed for the retrieval of BRDF parameters.

We also present two different applications based on the previous conclusions.

We first analyzed the error committed by many evapotranspiration studies that assume the surface as Lambertian and estimate the albedo from a surface reflectance weighted average (α_{REF}). We used different angular airborne images retrieved during the EODIX field campaign in order to derive the surface broadband albedo from the BRDF integration (α_{BRDF}) and compare the results with α_{REF} . The study showed α_{BRDF} stability through every image while α_{REF} presented high variation depending on the VZA. The highest difference was observed in the backward scattering direction along the hot spot region obtaining a RMSE of 0.11 through the AHS image which implied a relative error of 65%.

We also studied the influence of the albedo error on fluxes estimation such as the Rn, G, LE, H and daily ET. The Rn presented relative errors from 6 to 17%, obtaining the maximum error in the images that included the hot spot effect. We did not observe significant changes in case of G and EF. However, H, LE and daily ET showed relative errors ranging between 23-39%, 6-18% and 5-15% respectively. However, contrary to albedo and Rn where the highest error was obtained for the hot spot image, in case of H, LE and daily ET the highest error corresponded to the image with highest VZA in the solar plane.

We evaluated the results with in situ data. α_{BRDF} showed good agreement with RMSE of 0.01 and 0.03 for the wheat and barley field respectively. However, α_{REF} presented higher variability and a general overestimation in some VZA with RMSE of 0.03 and 0.05. We also obtained better results for the Rn using α_{BRDF} with RMSE of 12 and 24 $\text{W}\cdot\text{m}^{-2}$ than using α_{REF} with RMSE of 27 and 58 $\text{W}\cdot\text{m}^{-2}$ in the wheat and barley fields respectively. Both albedo and Rn showed a clear overestimation and underestimation respectively in the hot spot area when

CONCLUSIONS

using α_{REF} . G was only evaluated in the wheat field obtaining a clear airborne overestimation both using α_{REF} and α_{BRDF} leading to a RMSE of 40 and 41 $\text{W}\cdot\text{m}^{-2}$ respectively. As commented in Chapter 5 the difference was not just attributed to G algorithm but also to the ground heat flux plate inaccuracy commented in previous works (e.g., Halliwell and Rouse, 1987; Sauer et al., 2003). For LE both estimations from AHS images were in good agreement with in-situ measurements showing better results using α_{REF} with RMSE of 40 $\text{W}\cdot\text{m}^{-2}$ while in case of α_{BRDF} it reached 49.1 $\text{W}\cdot\text{m}^{-2}$. However, H presented a clear underestimation from airborne data leading to a RMSE of 88.7 $\text{W}\cdot\text{m}^{-2}$ when using α_{REF} and 79.6 $\text{W}\cdot\text{m}^{-2}$ when considering α_{BRDF} although these results should be considered with caution due to the noise detected in the H ground measurements.

It is important to note that the hot spot effect (which was the main source of error in case of the albedo and Rn estimation) was removed from α_{BRDF} images since we used the RTLSR-HS model. On the contrary, the RTLSR model, which is used in the MODIS algorithm, does not take into account this effect. Therefore, α_{BRDF} derived using this model would be affected by the hot spot effect and could lead to similar errors to α_{REF} .

As a conclusion, considering the Lambertian assumption to estimate surface albedo may lead to high errors in some fluxes estimations mainly for VZA higher than 35° and along the hot spot region. Therefore, for future ET studies we suggest the appropriate use of the RTLSR-HS modeled albedo.

Then, we also studied the albedo temporal evolution from 2002 to 2011 through a Europe and northern Africa scene using MODIS CMG data. We localized the pixels which suffered the highest albedo changes during this period. We divided the study into four categories of hazards responsible of the albedo increase: forest fires, wind storms, floods and droughts.

Forest fires, located in the Iberian Peninsula, led to albedo increases from 0.02 to 0.05 depending on the location. After most of these events we detected an increase of the seasonal extreme LST proportional to the albedo increase. The results also showed that this effect lasts three to four years

CONCLUSIONS

after the fire event while the albedo reestablishment takes longer. We did not notice significant changes in the air temperature extreme temperatures.

During the studied period two wind storms hit Europe damaging large forest areas in the Bordeaux region of Les Landes and the south of Sweden which increased the albedo by 0.02 in both cases. We observed an increase of the yearly average LST of 6K and of 2K in case of the air temperature in Les Landes during the year of the wind storm. South of Sweden did not show any influence of the temperatures corresponding to the albedo increase.

Floods caused a slight increase of 0.01 of albedo in the west of Germany and south of Poland which did not led to any significant change in temperatures.

Finally, a severe drought in the Euphrates valley in Syria damaged agricultural areas increasing the albedo by an average of 0.08. However, despite this strong increase we did not observe any influence on the temperatures.

This study showed that natural hazards that origin surface albedo alteration may impact LST depending on the location of the event (showing more impact on temperature Southern Europe sites) the magnitude of the hazard and the regional climate.

CONCLUSIONS

APENDIX

RELATED PUBLICATIONS

This section presents the articles published and to be published within the year 2013 in relation with this PhD dissertation. These articles are the following:

B. Franch, E.F. Vermote, J.A. Sobrino and E. Fédèle, E. (2013). Analysis of directional effects on atmospheric correction. *Remote Sensing of Environment*, 128, 276-288

J.A. Sobrino, B. Franch, R. Oltra-Carrió, E.F. Vermote and E. Fédèle (Accepted). Evaluation of the MODIS albedo product over a heterogeneous agricultural area. *International Journal of Remote Sensing*.

APPENDIX

Related Publications

J.A. Sobrino and B. Franch (2011). Estimación de la reflectividad superficial mediante datos del sensor aéreo AHS y comparación con el producto MODIS en la campaña CEFLES2. *Revista Española de Teledetección*, volumen 35, 72-79.

B. Franch, E.F. Vermote, J.A. Sobrino and Y. Julien (sent). Retrieval of surface albedo on a daily basis: Application to MODIS data. *Remote Sensing of Environment*.

C. Mattar, B. Franch, J.A. Sobrino, J.C. Jimenez-Muñoz, C. Corbari, L. Olivera, D. Skokovic, G. Sòria, R. Oltra-Carrió, Y. Julien and M. Mancini (sent). Directional Effects on daily Evapotranspiration Estimations. *Agriculture and forest meteorology*.

B. Franch and J.A. Sobrino (sent). Evolución del albedo en Europa e influencia en la temperatura. *Revista Española de Teledetección*.

REFERENCES

- Allen, R., Tasumi, M., and Trezza, R. 2007. Satellite-based energy balance for mapping evapotranspiration with internalized calibration METRIC – Model. *Journal of Irrigation and Drainage Engineering*, 133(4), 380-394.
- Bacour, C., and Bréon, F.-M. (2005). Variability of biome reflectance directional signatures as seen by POLDER. *Remote Sensing of Environment*, 98, 80-95
- Bala, G., Caldeira, K., Wickett, M., Phillips, T. J., Lobell, D. B., Delire, C., and Mirin, A. (2007). Combined climate and carbon-cycle effects of large-scale deforestation. *Proceedings of the National Academy of Sciences*, 104, 6550-6555

REFERENCES

- Barnsley, M.J., Allison, D., and Lewis, P. (1997). On the information content of multiple view angle (MVA) images. *International Journal of Remote Sensing*, 18, 1937-1960
- Bastiaanssen W. G. M., M. Menenti, R. A. Feddes and A. A. Holtslag, 1998. A remote sensing surface energy balance algorithm for land (SEBAL). 1. Formulation. *J. Hydrol.* 212-213, 198-212
- Bastiaanssen, W. G. M., Molden, D. J., and Makin, I. W. (2000). Remote sensing for irrigated agriculture: Examples from research of possible applications. *Agric. Water Manage.*, 46(2), 137–155.
- Bengtsson A. and Nilsson, C. (2007). Extreme value modelling of storm damage in Swedish forests. *Nat. Hazards Earth Syst. Sci.*, 7, 515–521.
- Betts, R.A. (2000). Offset of the potential carbon sink from boreal forestation by decreases in surface albedo. *Nature*, 408, 187-190
- Berk, A., Bernstein, L. S., Anderson, G. P., Acharya, P. K., Robertson, D. C., Chetwynd, J. H. and Adler-Golden, S. M., 1998: MODTRAN cloud and multiple scattering upgrades with application to AVIRIS. *Remote Sensing of Environment* 65, 367-375
- Bicheron, P., and Leroy, M. (1999). A Method of Biophysical Parameter Retrieval at Global Scale by Inversion of a Vegetation Reflectance Model. *Remote Sensing of Environment*, 67, 251-266
- Bonan, G.B. (2008). Forests and Climate Change: Forcings, Feedbacks, and the Climate Benefits of Forests. *Science*, 320, 1444-1449
- Bounoua, L., DeFries, R., Collatz, G. J., Sellers, P., and Khan, H. (2002). Effects of Land Cover Conversion on Surface Climate. *Climatic Change*, 52, 29-64
- Breon, F.-M., and Vermote, E.F. (2012). Correction of MODIS surface reflectance time series for BRDF effects. *Remote Sensing of Environment*, 125, 1-9

REFERENCES

- Breon, F.M., Maignan, F., Leroy, M., and Grant, I. (2002). Analysis of hot spot directional signatures measured from space. *Journal of Geophysical Research-Atmospheres*, 107
- Cabot, F., and Dedieu, G. (1997). Surface albedo from space: Coupling bidirectional models and remotely sensed measurements. *Journal of Geophysical Research-Atmospheres*, 102, 19645-19663
- Camacho-de Coca, F., Jiménez-Muñoz, J.C., Martínez, B., Bicheron, P., Lacaze, R. y Leroy, M. (2006). Prototyping of fCover product over Africa based on existing CYCLOPES and JRC products for VGT4Africa. *Proceedings of the 2nd RAQRS symposium*, pp. 724-727
- Cescatti, A., Marcolla, B., Santhana Vannan, S.K., Pan, J.Y., Roman, M.O., Yang, X., Ciais, P., Cook, R.B., Law, B.E., Matteucci, G., Migliavacca, M., Moors, E., Richardson, A.D., Seufert, G.n. and Schaaf, C.B. (2012). Intercomparison of MODIS albedo retrievals and in situ measurements across the global FLUXNET network. *Remote Sensing of Environment*, 121, 323-334
- Cess, R.D. (1978). Biosphere-Albedo Feedback and Climate Modeling. *Journal of the Atmospheric Sciences*, 35, 1765-1768
- Clothier, B.E., K.L. Clawson, P.J. Pinter Jr., M.S. Moran, R.J. Reginato and R.D. Jackson. 1986. Estimation of soil heat flux from net radiation and soil heat flux. *Rem. Sens. Environ.* 37:3 19-329
- Coddington, O., Schmidt, K. Sebastian, Pilewskie, Peter, Gore, Warren J., Bergstrom, Robert W., Román, Miguel, Redemann, Jens, Russell, Philip B., Liu, Jicheng, and Schaaf, Crystal C. (2008). Aircraft measurements of spectral surface albedo and its consistency with ground-based and space-borne observations. *J. Geophys. Res.*, 113, D17209
- Corbari, C., Ravazzani, G., Mancini, M., 2011. A distributed thermodynamic model for energy and mass balance computation: FEST-EWB, *Hydrol. Process.* 25, 1443–1452.

REFERENCES

- Corbari C., Masseroni D., Mancini M., 2012. Effetto delle correzioni dei dati misurati da stazioni eddy covariance sulla stima dei flussi evapotraspirativi, *Italian Journal of Agrometeorology*, 1, 35-51
- Courault, D., Seguin, B., Olioso, A., 2005. Review on estimation of evapotranspiration from remote sensing data: From empirical to numerical modeling approaches. *Irrig. Drain. Syst.*, 19(3-4): 223-249.
- Cowan, I.R., and Farquhar, G. D. (1977). Stomatal function in relation to leaf metabolism and environment. *Symp Soc Exp Biol*, 31, 471-505
- Cunnington, W.M., and Rowntree, P. R. (1986). Simulations of the Saharan atmosphere – Dependence on moisture and albedo. *Quarterly Journal of the Royal Meteorological Society*, 112, 971-999
- Charlson, R.J., Valero, Francisco P. J., and Seinfeld, John H. (2005). In Search of Balance. *Science*, 308, 806-807
- Charney, J. (1975). Dynamics of deserts and drought in the Sahel. *The Physical Basis of Climate and Climate Modelling*. GARP Publications Series No. 16. World Meteorological Organization: Geneva, Switzerland, 171-175
- Charney, J., Quirk, William J., Chow, Shu-hsien, and Kornfield, Jack (1977). A Comparative Study of the Effects of Albedo Change on Drought in Semi-Arid Regions. *Journal of the Atmospheric Sciences*, 34, 1366-1385
- Chervin, R.M. (1979). Response on the NCAR general circulation model to changed land surface albedo. . Report of the JOC study Conf. on Climate Models, 1, 563-581
- DeFries, R.S., Bounoua, L., and Collatz, G. J. (2002). Human modification of the landscape and surface climate in the next fifty years. *Global change biology.*, 8, 438-458
- Detto, M., Montaldo, N., Alberston, J., Mancini, M., & Katul, G. 2006. Soil moisture and vegetation controls on evapotranspiration in a eterogeneous Mediteranean ecosystem on Sardinia, Italy. *Water Resour. Res.*, 42, 1-16.

REFERENCES

- Diffenbaugh, N.S., and Sloan, L.C. (2002). Global climate sensitivity to land surface change: The Mid Holocene revisited. *Geophys. Res. Lett.*, 29, 1476
- Diner, D.J., Beckert, J. C., Reilly, T. H., Bruegge, C. J., Conel, J. E., Kahn, R. A., Martonchik, J. V., Ackerman, T. P., Davies, R., Gerstl, S. A. W., Gordon, H. R., Muller, J. P., Myneni, R. B., Sellers, P. J., Pinty, B., and Verstraete, M. M. (1998). Multi-angle Imaging SpectroRadiometer (MISR) instrument description and experiment overview. *Geoscience and Remote Sensing, IEEE Transactions on*, 36, 1072-1087
- Dirmeyer, P.A., and Shukla, J. (1996). The effect on regional and global climate of expansion of the world's deserts. *Quarterly Journal of the Royal Meteorological Society*, 122, 451-482
- Feddema, J.J., Oleson, Keith W., Bonan, Gordon B., Mearns, Linda O., Buja, Lawrence E., Meehl, Gerald A., and Washington, Warren M. (2005). The Importance of Land-Cover Change in Simulating Future Climates. *Science*, 310, 1674-1678
- Field, C.B., Lobell, David B., Peters, Halton A., and Chiariello, Nona R. (2007). Feedbacks of Terrestrial Ecosystems to Climate Change. *Annual Review of Environment and Resources*, 32, 1-29
- Franch, B., Vermote, E. F., Sobrino, J. A. and Fédèle, E. (2013). Analysis of directional effects on atmospheric correction. *Remote Sensing of Environment*, 128, 276-288
- French, A., Jacob, F., Anderson, M., Kustas, W., Timmermans, W., Gieske, A., et al. 2005. Surface energy fluxes with the Advanced Spaceborne Thermal Emission and Reflection radiometer (ASTER) at the Iowa 2002 SMACEX site (USA). *Remote Sensing of Environment*, 99(1–2), 55-65
- Galleguillos, M., F. Jacob, L. Prévot, A. French, and Lagacherie, P. 2011. Comparison of two temperature differencing methods to estimate daily evapotranspiration over a Mediterranean vineyard watershed from ASTER data. *Remote Sensing of Environment*, 115, 1326–1340

REFERENCES

- Gao, F., Schaaf, C. B., Strahler, A. H., and Lucht, W. (2001). Using a multikernel least-variance approach to retrieve and evaluate albedo from limited bidirectional measurements. *Remote Sensing of Environment*, 76, 57-66
- Gillespie, A. R., Matsunaga, T., Rokugawa, S. & Hook, S. J. 1998. Temperature and emissivity separation from Advanced Spaceborne Thermal Emission and Reflection Radiometer (ASTER) images. *IEEE Transactions on Geoscience and Remote Sensing*, 36, 1113-1125
- Gutman, G. G. (1991). Vegetation indices from AVHRR data: an update and future prospects. *Remote Sensing of Environment*, 35, 121 – 136.
- Gutman, G., & Ignatov, A. (1998). The derivation of the green vegetation fraction from NOAA/AVHRR data for use in numerical weather prediction models, *International Journal of Remote Sensing*, 19(8), 1533-1543
- Halliwell, D. H. and Rouse, W.R. (1987). Soil heat flux in permafrost: Characteristics and accuracy of measurement. *J. Climatol.*, 7: 571–584.
- Hsieh, C., Katul, G. & Chi, T. 2000. An approximate analytical model for footprint estimation of scalar fluxes in thermally stratified atmospheric flows. *Ad. Water Resour.* 23, 765-772.
- Hu, B.X., Lucht, W., and Strahler, A. H. (1999). The interrelationship of atmospheric correction of reflectances and surface BRDF retrieval: A sensitivity study. *Ieee Transactions on Geoscience and Remote Sensing*, 37, 724-738
- Huete, A., Justice, C., and van Leeuwen, W. (1999). MODIS Vegetation Index, Algorithm Theoretical Basis Document (ATDB) Version 3. University of Arizona (online at: http://modis.gsfc.nasa.gov/data/atbd/atbd_mod13.pdf)
- Hyman, A.H., and Barnsley, M. J. (1997). On the potential for land cover mapping from multiple-view-angle (MVA) remotely-sensed images. *International Journal of Remote Sensing*, 18, 2471-2475

REFERENCES

- Jackson, R., B., James T. Randerson, Josep G. Canadell, Ray G. Anderson, Roni Avissar, Dennis D. Baldocchi, Gordon B. Bonan, Ken Caldeira, Noah S. Diffenbaugh, Christopher B. Field, Bruce A. Hungate, Esteban G. Jobbágy, Lara M. Kueppers, Marcelo D. Noesetto, and Diane E. Pataki (2008). Protecting climate with forests. *Environmental Research Letters*, 3, 044006
- Jackson, R.B., Jobbágy, Esteban G., Avissar, Roni, Roy, Somnath Baidya, Barrett, Damian J., Cook, Charles W., Farley, Kathleen A., le Maitre, David C., McCarl, Bruce A., and Murray, Brian C. (2005). Trading Water for Carbon with Biological Carbon Sequestration. *Science*, 310, 1944-1947
- J. C. Jiménez-Muñoz and J. A. Sobrino (2006). Error sources on the land surface temperature retrieval from thermal infrared single channel remote sensing data. *International Journal of Remote Sensing*, Vol. 27, Nos. 5-6, pp. 999-1014.
- Jin, Y.F., Schaaf, C.B., Gao, F., Li, X.W., Strahler, A.H., Lucht, W. and Liang, S.L. (2003). Consistency of MODIS surface bidirectional reflectance distribution function and albedo retrievals: 1. Algorithm performance. *Journal of Geophysical Research-Atmospheres*, 108
- Juang, J.-Y., Katul, G., Siqueira, M., Stoy, P. and Novick, K. (2007). Separating the effects of albedo from eco-physiological changes on surface temperature along a successional chronosequence in the southeastern United States. *Geophys. Res. Lett.*, 34, L21408
- Jung, M., Reichstein, M., Ciais, P., Seneviratne, S.I., Sheffield, J., Goulden, M.L., Bonan, G., Cescatti, A., Chen, J., de Jeu, R., Dolman, A. J., Eugster, W., Gerten, D., Gianelle, D., Gobron, N., Heinke, J., Kimball, J., Law, B.E., Montagnani, L., Mu, Q., Mueller, B., Oleson, K., Papale, D., Richardson, A.D., Rouspard, O., Running, S., Tomelleri, E., Viovy, N., Weber, U., Williams, C., Wood, E., Zaehle, S., Zhang, K., 2010, Recent decline in the global land evapotranspiration trend due to limited moisture supply, *Nature* 467, 951-954

REFERENCES

- Justice, C.O., Vermote, E., Townshend, J. R. G., Defries, R., Roy, D. P., Hall, D. K., Salomonson, V. V., Privette, J. L., Riggs, G., Strahler, A., Lucht, W., Myneni, R. B., Knyazikhin, Y., Running, S. W., Nemani, R. R., Wan, Z. M., Huete, A. R., van Leeuwen, W., Wolfe, R. E., Giglio, L., Muller, J. P., Lewis, P., and Barnsley, M. J. (1998). The Moderate Resolution Imaging Spectroradiometer (MODIS): Land remote sensing for global change research. *Ieee Transactions on Geoscience and Remote Sensing*, 36, 1228-1249
- Kaufman, Y.J., Tanré, D., Remer, L.A., Vermote, E., Chu, A., and Holben, B. N., 1997. Operational remote sensing of tropospheric aerosol over land from EOS Moderate Resolution Imaging Spectroradiometer. *J. Geophys. Res.*, 102, 17 051–17 067.
- Kistler, R., Collins, W., Saha, S., White, G., Woollen, J., Kalnay, E., et al. (2001). The NCEPNCAR 50-year reanalysis: Monthly means CD-ROM and documentation. *Bulletin of the American Meteorological Society*, 82, 247–267.
- Kljun, N., Calanca, P., Rotach, M. & Schmid, H. 2004. A simple parameterization flux footprint predictions. *Bound.-Lay. Meteorol.* 112, 503-523.
- Knorr, W., Schnitzler, K. G., and Govaerts, Y. (2001). The role of bright desert regions in shaping North African climate. *Geophysical Research Letters*, 28, 3489-3492
- Knyazikhin, Y., Martonchik, J. V., Diner, D. J., Myneni, R. B., Verstraete, M., Pinty, B., and Gobron, N. (1998). Estimation of vegetation canopy leaf area index and fraction of absorbed photosynthetically active radiation from atmosphere-corrected MISR data. *J. Geophys. Res.*, 103, 32239-32256
- Koster, R. D. et al. Regions of strong coupling between soil moisture and precipitation. *Science* 305, 1138–1140 (2004)
- Kriebel, K.T. (1978). Measured spectral bidirectional reflectance properties of vegetated surfaces. *Applied Optics*, 17, 253-259

REFERENCES

- Lee, T.Y., and Kaufman, Y. J. (1986). Non-Lambertian Effects on Remote-Sensing of Surface Reflectance and Vegetation Index. *Ieee Transactions on Geoscience and Remote Sensing*, 24, 699-708
- Leroy, M., and Roujean, J. L. (1994). Sun and view angle corrections on reflectances derived from NOAA AVHRR DATA. *Ieee Transactions on Geoscience and Remote Sensing*, 32, 684-697
- Leroy, M., Deuze, J. L., Breon, F. M., Hautecoeur, O., Herman, M., Buriez, J. C., Tanre, D., Bouffies, S., Chazette, P., and Roujean, J. L. (1997). Retrieval of atmospheric properties and surface bidirectional reflectances over land from POLDER/ADEOS. *Journal of Geophysical Research-Atmospheres*, 102, 17023-17037
- Levy, R. C., L. A. Remer, D. Tanre, Y. J. Kaufman, C. Ichoku, B. N. Holben, J. M. Livingston, P. B. Russell, and H. Maring, 2003. Evaluation of the MODIS retrievals of dust aerosol over the ocean during PRIDE. *J. Geophys. Res.*, 108, 8594, doi:10.1029/2002JD002460.
- Lewis, P., and Barnsley, M.J. (1994). Influence of the sky radiance distribution on various formulations of the earth surface albedo. *Proc. Conf. Phys. Meas. Sign. Remote Sens.*, Vol. d'Isere. France, 707-715
- Li, X.W., and Strahler, A. H. (1986). Geometric-Optical Bidirectional Reflectance Modeling of a Conifer Forest Canopy. *Ieee Transactions on Geoscience and Remote Sensing*, 24, 906-919
- Li, X.W., and Strahler, A. H. (1992). Geometric-optical bidirectional reflectance modeling of the discrete crown vegetation canopy – Effect of crown shape and mutual shadowing. *Ieee Transactions on Geoscience and Remote Sensing*, 30, 276-292
- Liang, S.L. (2000). Narrowband to broadband conversions of land surface albedo I Algorithms. *Remote Sensing of Environment*, 76, 213-238
- Liang, S., Fang, H., Chen, M., Shuey, C.J., Walthall, C., Daughtry, C., Morisette, J., Schaaf, C. and Strahler, A. (2002). Validating MODIS

REFERENCES

- land surface reflectance and albedo products: methods and preliminary results. *Remote Sensing of Environment*, 83, 149-162
- Liu, H., Peters, G. & Foken, T. 2001. New equations for sonic temperature variance and buoyancy heat flux with an omnidirectional sonic anemometer. *Bound.-Lay. Meteorol.* 100, 459-468.
- Liu, J.C., Schaaf, C., Strahler, A., Jiao, Z.T., Shuai, Y.M., Zhang, Q.L., Roman, M., Augustine, J.A. and Dutton, E.G. (2009). Validation of Moderate Resolution Imaging Spectroradiometer (MODIS) albedo retrieval algorithm: Dependence of albedo on solar zenith angle. *Journal of Geophysical Research-Atmospheres*, 114
- Lucht, W. (1998). Expected retrieval accuracies of bidirectional reflectance and albedo from EOS-MODIS and MISR angular sampling. *Journal of Geophysical Research-Atmospheres*, 103, 8763-8778
- Lucht, W., Hyman, A. H., Strahler, A. H., Barnsley, M. J., Hobson, P., and Muller, J. P. (2000). A comparison of satellite-derived spectral albedos to ground-based broadband albedo measurements modeled to satellite spatial scale for a semidesert landscape. *Remote Sensing of Environment*, 74, 85-98
- Lyapustin, A.I. (1999). Atmospheric and geometrical effects on land surface albedo. *J. Geophys. Res.*, 104, 4127-4143
- Lyapustin, A.I., Yujie, W., Martonchik, J., Privette, J.L., Holben, B., Slutsker, I., Sinyuk, A., and Smirnov, A. (2006). Local analysis of MISR surface BRF and albedo over GSFC and mongu AERONET sites. *IEEE T. Geoscience and Remote Sensing*, 1707-1718
- Maignan, F., Breon, F. M., and Lacaze, R. (2004). Bidirectional reflectance of Earth targets: Evaluation of analytical models using a large set of spaceborne measurements with emphasis on the Hot Spot. *Remote Sensing of Environment*, 90, 210-220
- Massman, W. & Lee, X. 2002. Eddy covariance flux corrections and uncertainties in long-term studies of carbon and energy exchanges. *Agr. For. Meteorol.* 113, 121-144.

REFERENCES

- McCabe, M. F., and Wood, E. F. 2006. Scale influences on the remote estimation of evapotranspiration using multiple satellite sensors. *Remote Sensing of Environment*, 105, 271-285.
- Menenti, M., and Choudhury, B. 1993. Parameterization of land surface evaporation by means of location dependent potential evaporation and surface temperature range. *Proceedings of IAHS conference on Land Surface Processes*. IAHS Publ., 212, 561-568
- Mintz, Y. (1984). The sensitivity of numerically simulated climates to land-surface conditions. *The Global Climate*, Houghton J (ed.). Cambridge University Press: Cambridge, 79-105
- Moreno, J., Calera, A., Caselles, V., Cisneros, J.M., Martínez-Lozano, J.A., Meliá, J., Montero, F., and Sobrino, J.A., (2001). The measurement programme at Barrax, in DAISEX Final Results Workshop, NASA Spec. Publ., SP-499, pp. 43– 51
- Morisette, J.T., Privette, J.L. and Justice, C.O. (2002). A framework for the validation of MODIS Land products, *Remote sensing of environment*, 83, 77-96.
- Nicodemus, F.E., Richmond, J.C., Hsia, J.J., Ginsberg, I.W. and Limperis, T., 1977, Geometrical considerations and nomenclature for reflectance. Tech. rep., National Bureau of Standards, US Department of Commerce, Washington, DC, USA.
- Nilson, T., and Kuusk, A. (1989). A reflectance model for the homogeneous plant canopy and its inversion. *Remote Sensing of Environment*, 27, 157-167
- Oki, T. & Kanae, S. Global hydrological cycles and world water resources. *Science* 313, 1068–1072 (2006)
- Oleson, K., Bonan, G., Levis, S., and Vertenstein, M. (2004). Effects of land use change on North American climate: Impact of surface datasets and model biogeophysics. *Climate Dynamics*, 23
- Otterman, J. (1977). Anthropogenic impact on the albedo of the earth. *Climatic Change*, 1, 137-155

REFERENCES

- Pánek, T., Silhán, K., TáBořík, P., Hradecký, J., Smolková, V., Lenart, J., Brázdil, R., Kašičková, L. and Pazdur, A. (2011). catastrophic slope failure and its origins: case study of May 2010 Girová mountain long-runout rock slide (Czech Republic). *Geomorphology*, 130, 352–364.
- Payero, J.O., Neale, C.M.U. and Wright, J.L. (2005). Estimating soil heat flux for alfalfa and clipped tall fescue grass. *American Society of Agricultural Engineers*, Vol. 21(3): 401–409.
- Pielke, R.A., Marland, Gregg, Betts, Richard A., Chase, Thomas N., Eastman, Joseph L., Niles, John O., Niyogi, Dev dutta S., and Running, Steven W. (2002). The influence of land-use change and landscape dynamics on the climate system: relevance to climate-change policy beyond the radiative effect of greenhouse gases. *Philosophical Transactions of the Royal Society of London. Series A: Mathematical, Physical and Engineering Sciences*, 360, 1705-1719
- Pinty, B., and Verstraete, M. 1992. On the design and validation of surface bidirectional reflectance and albedo model. *Remote Sensing of Environment*, 41, 155–167.
- Pitman, A.J. (2003). The evolution of, and revolution in, land surface schemes designed for climate models. *International Journal of Climatology*, 23, 479-510
- Roerink, G. J., B. Su, and M. Menenti. 2000. S-SEBI: A simple remote sensing algorithm to estimate the surface energy balance. *Physics and Chemistry of the Earth, Part B* 25(2), 147-157
- Roesch, A., Schaaf, C. and Gao, F. (2004). Use of Moderate-Resolution Imaging Spectroradiometer bidirectional reflectance distribution function products to enhance simulated surface albedos. *Journal of Geophysical Research-Atmospheres*, 109
- Roujean, J.L., Leroy, M. and Deschamps, P. Y. (1992). A Bidirectional Reflectance Model of the Earths Surface for the Correction of Remote-Sensing Data. *Journal of Geophysical Research-Atmospheres*, 97, 20455-20468

REFERENCES

- Sauer, T. J., Meeka, D. W., Ochsnerb, T. E., Harrisc, A. R., and Horton, R. (2003). Errors in Heat Flux Measurement by Flux Plates of Contrasting Design and Thermal Conductivity. Vol. 2 no. 4 p. 580-588.
- Schaeffer, M., Eickhout, B., Hoogwijk, M., Strengers, B., van Vuuren, D., Leemans, R., and Opsteegh, T. (2006). CO₂ and albedo climate impacts of extratropical carbon and biomass plantations. *Global Biogeochem. Cycles*, 20, GB2020
- Schaepman-Strub, G., Schaepman, M. E., Painter, T. H., Dangel, S. and Martonchik, J. V. (2006). Reflectance quantities in optical remote sensing-definitions and case studies. *Remote Sensing of Environment*, 103, 27-42
- Schmid, H. 1994. Source areas for scalars and scalar fluxes. *Bound.-Lay. Meteorol.* 67, 293-318.
- Seemann, S. W., Borbas, E. E., Li, J., Menzel, W. P., & Gumley, L. E. (2006). MODIS atmospheric profile retrieval algorithm theoretical basis document. Version 6, October 25.
- Seguin, B. and B. Itier (1983): Using midday surface temperature to estimate daily evaporation from satellite thermal IR data. *International Journal of Remote Sensing* 4(2): 371-383
- Seneviratne, S. I., Lüthi, D., Litschi, M. & Schär, C. Land-atmosphere coupling and climate change in Europe. *Nature* 443, 205-209 (2006)
- Slater, P. N. (1980), *Remote Sensing Optics and Optical Systems*, Addison-Wesley Publishing Company.
- Sobrinho, J.A. and Cuenca, J. (1999) Angular variation of emissivity for some natural surfaces from experimental measurements. *Applied Optics*, 38 (1999), pp. 3931-3936
- Sobrinho J A, El-Kharraz J and Li Z (2003). Surface temperature and water vapour retrieval from MODIS data; *Int. J. Remote Sens.* 24(24) 5161-5182

REFERENCES

- Sobrino, J.A., Jiménez-Muñoz, J. C., Zarco-Tejada, P. J., Sepulcre-Cantó, G. and de Miguel, E. 2006. Land surface temperature derived from airborne hyperspectral scanner thermal infrared data. *Remote Sensing of Environment*, 102, 99-115
- Sobrino, J., Gomez, M., Jimenez-Munoz, J., and Olioso, A. 2007a. Application of a simple algorithm to estimate daily evapotranspiration from NOAA-AVHRR images for the Iberian Peninsula. *Remote Sensing of Environment*, 110(2), 139–148.
- Sobrino, J. A., Jimenez-Munoz, J. C., Balick, L., Gillespie, A. R., Sabol, D. E., and Gustafson, W. T. 2007b. Accuracy of ASTER level-2 thermal-infrared standard products of an agricultural area in Spain. *Remote Sensing of Environment*, 106, 146–153
- Sobrino, J.A., Jimenez-Munoz, J. C., Zarco-Tejada, P. J., Sepulcre-Canto, G., de Miguel, E., Soria, G., Romaguera, M., Julien, Y., Cuenca, J., Hidalgo, V., Franch, B., Mattar, C., Morales, L., Gillespie, A., Sabol, D., Balick, L., Su, Z., Jia, L., Gieske, A., Timmermans, W., Olioso, A., Nerry, F., Guanter, L., Moreno, J., Shen, Q. (2009). Thermal remote sensing from Airborne Hyperspectral Scanner data in the framework of the SPARC and SEN2FLEX projects: an overview. *Hydrology and Earth System Sciences*, 13, 2031-2037
- Sobrino, J. A., C. Mattar, J. P. Gastellu-Etchegorry, J. C. Jiménez-Muñoz and E. Grau (2011). Evaluation of the DART 3D model in the thermal domain using satellite/airborne imagery and ground-based measurements. *International Journal of Remote Sensing*, Vol. 32, No. 22, pp. 7453-7477.
- Strahler, A.H., Wanner, W., Schaaf, C., Li, X., Muller, J.P., Lewis, P., and Barnsley, M.J. (1999). MODIS BRDF/albedo product: ATBD, Version 5.0
- Su, Z. and Menenti, M. (Eds.), 1999. Mesoscale climate hydrology: the contribution of the new observing systems. Report USP-2, 99-05, Publications of the National Remote Sensing Board (BCRS). 141pp.

REFERENCES

- Su, Z., Pelgrum, H. and Menenti, M., 1999. Aggregation effects of surface heterogeneity in land surface processes. *Hydrol. Earth Sys. Sci.*, 3, 549–563.
- Su, Z. 2002. The Surface Energy Balance System (SEBS) for estimation of turbulent heat fluxes. *Hydrological and Earth System Sciences*, 6(1), 85-100.
- Sud, Y.C., and Fennessy, M. (1982). A study of the influence of surface albedo on July circulation in semi-arid regions using the GLAS GCM. *Journal of Climatology*, 2, 105-125
- Sud, Y.C., and Molod, A. (1988). A GCM simulation study of the influence of Saharan evapotranspiration and surface albedo anomalies on July circulation and rainfall. *Monthly Weather Review*, 116, 2388-2400
- Tanner, C. & Thurtell, G. 1969. Anemoclinometer measurements of Reynolds stress and heat transport in the atmospheric surface layer. ECOM 66-G22-F, ECOM, United States Army Electronics Command, Research and Development .
- Tanré, D., Kaufman, Y. J., Herman, M. and Mattoo, S., 1997: Remote sensing of aerosol properties over oceans using the MODIS/EOS spectral radiances. *J. Geophys. Res.*, 102, 16 971–16 988
- Timmermans, W., W. Kustas, M. Anderson, and A. French. 2007. An intercomparison of the Surface Energy Balance Algorithm for Land (SEBAL) and the Two-Source Energy Balance (TSEB) modeling schemes. *Remote Sensing of Environment*, 108(4), 369–384.
- Tittebrand, A. and Berger, F. 2008. Spatial heterogeneity of satellite derived land surface parameters and energy flux densities for LITFASS-area. *Atmospheric Chemistry and Physics Discussion*, 8(4), 16219–16254.
- Trigo, R.M., J.M.C. Pereira, M.G. Pereira, B. Mota, T.J. Calado, C.C. Dacamara and F.E. Santo, 2006: Atmospheric conditions associated with the exceptional fire season of 2003 in Portugal. *Int. J. Climatol.*, 26, 1741-1757.
- Tucker, C. J., 1979: Red and photographic infrared linear combinations for monitoring vegetation. *Remote Sens. Environ.*, 8, 127–150.

REFERENCES

- Vautard, R. et al. Summertime European heat and drought waves induced by wintertime Mediterranean rainfall deficit. *Geophys. Res. Lett.* L07711 (2007)
- Verhoef, W., and Bach, H. (2003). Simulation of hyperspectral and directional radiance images using coupled biophysical and atmospheric radiative transfer models. *Remote Sensing of Environment*, 87, 23-41
- Vermote, E.F., ElSaleous, N., Justice, C. O., Kaufman, Y. J., Privette, J. L., Remer, L., Roger, J. C., and Tanre, D. (1997). Atmospheric correction of visible to middle-infrared EOS-MODIS data over land surfaces: Background, operational algorithm and validation. *Journal of Geophysical Research-Atmospheres*, 102, 17131-17141
- Vermote, E.F., and Vermeulen, A (1999). Atmospheric correction algorithm: spectral reflectances (MOD09). Algorithm Theoretical Background Document available on line at http://modarch.gsfc.nasa.gov/MODIS/ATBD/atbd_mod08.pdf.
- Vermote, E.F., Tanre, D., Deuze, J. L., Herman, M., Morcrette, J. J., Kotchenova, S. Y., and Miura, T. (2006). Second Simulation of the Satellite Signal in the Solar Spectrum (6S). 6S User Guide Version 3 (November, 2006), <http://www.6s.ltdri.org>
- Vermote, E.F., and Kotchenova, S. (2008). Atmospheric correction for the monitoring of land surfaces. *Journal of Geophysical Research-Atmospheres*, 113
- Vermote, E., Justice, C. O., and Breon, F. M. (2009). Towards a Generalized Approach for Correction of the BRDF Effect in MODIS Directional Reflectances. *Ieee Transactions on Geoscience and Remote Sensing*, 47, 898-908
- Verstraeten, W. W., B. Muys, J. Feyen, F. Veroustraete, M. Minnaert, L. Meiresonne, and A. D. Schrijver (2005), Comparative analysis of the actual evapotranspiration of Flemish forest and cropland, using the soil water balance model WAVE, *Hydrol. Earth Syst. Sci.*, 9, 225 – 2241.

REFERENCES

- Vinukollu, R., E. Wood, C. Ferguson, and Fisher, J. 2011. Global estimates of evapotranspiration for climate studies using multi-sensor remote sensing data: Evaluation of three process-based approaches. *Remote Sensing of Environment*, 115(3), 801–823
- Walthall, C.L., Norman, J. M., Welles, J. M., Campbell, G., and Blad, B. L. (1985). Simple equation to approximate the bidirectional reflectance from vegetative canopies and bare soil surfaces. *Applied Optics*, 24, 383-387
- Wang, S.S., and Davidson, A. (2007). Impact of climate variations on surface albedo of a temperate grassland. *Agricultural and Forest Meteorology*, 142, 133-142
- Wang, Y., Lyapustin, A. I., Privette, J. L., Morisette, J. T., and Holben, B. (2009). Atmospheric correction at AERONET locations: a new science and validation dataset. *Ieee Transactions on Geoscience and Remote Sensing*, 47(8), 2450-2466
- Wang, Y.J., Lyapustin, A. I., Privette, J. L., Cook, R. B., SanthanaVannan, S. K., Vermote, E. F., and Schaaf, C. L. (2010). Assessment of biases in MODIS surface reflectance due to Lambertian approximation. *Remote Sensing of Environment*, 114, 2791-2801
- Wanner, W., Li, X., and Strahler, A. H. (1995). On the Derivation of Kernels for Kernel-Driven Models of Bidirectional Reflectance. *Journal of Geophysical Research-Atmospheres*, 100, 21077-21089
- Wanner, W., Strahler, A. H., Hu, B., Lewis, P., Muller, J. P., Li, X., Schaaf, C. L. B., and Barnsley, M. J. (1997). Global retrieval of bidirectional reflectance and albedo over land from EOS MODIS and MISR data: Theory and algorithm. *Journal of Geophysical Research-Atmospheres*, 102, 17143-17161
- Webb, E., Pearman, G. & Leuning, R. 1980. Correction of the flux measurements for density effects due to heat and water vapour transfer. *Bound.-Lay. Meteorol.* 23, 251-254.
- Wu, A.H., Li, Z. Q., and Cihlar, J. (1995). Effects of land-cover type and greens on advanced very high-resolution radiometer bidirectional

REFERENCES

- reflectances – Analysis and removal. *Journal of Geophysical Research-Atmospheres*, 100, 9179-9192
- Xue, Y.K., and Shukla, J. (1993). The influence of land-surface properties on Sahel climate. 1. Desertification. *Journal of Climate*, 6, 2232-2245
- Zhang, H., Henderson-Sellers, A., and McGuffie, K. (2001). The compounding effects of tropical deforestation and greenhouse warming on climate. *Climatic Change*, 49, 309-338
- Zhang, Y., Tian, Y., Myneni, R. B., Knyazikhin, Y., and Woodcock, C. E. (2002). Assessing the information content of multiangle satellite data for mapping biomes I. Statistical analysis. *Remote Sensing of Environment*, 80, 418-43